ISSN 1580-2949
UDK 669+666+678+53 MTAEC9, 44(3)103–161(2010)

MATER. TEHNOL.	LETNIK VOLUME 44	ŠTEV. NO. 3	STR. P. 103–161	LJUBLJANA SLOVENIJA	MAY–JUN. 2010

VSEBINA – CONTENTS

UDK 669.14.018.298:621.791:621.785
Pregledni članek/Review article

ISSN 1580-2949
MTAEC9, 44(3)105(2010)

PHYSICAL SIMULATION OF METALLURGICAL PROCESSES

FIZIKALNA SIMULACIJA METALURŠKIH PROCESOV

Stan T. Mandziej

Advanced Materials Analysis, P. O. Box 3751, NL–7500DT Enschede, Nederland
stanamanl@cs.com

Prejem rokopisa – received: 2009-11-16; sprejem za objavo – accepted for publication: 2009-12-08

Worldwide demand of better and more efficient metallurgical processes, leading to low costs of their products, stimulates intensive research to reach these goals. In this respect, any full-scale industrial experiments appear non-acceptable. Cutting off the R&D costs and fast introducing of new technologies is possible when physical and numerical simulations are used. The computer simulation can be only correct when exact data of materials behaviour at processing conditions are known. To obtain the data, physical simulation is needed and it must be executed on multi-purpose thermal-mechanical testing devices accurately reproducing the real industrial processing conditions. For continuous casting or metal forming, individual phases of processes or multi-step operations must be followed, characterized by their time, temperature, and by applied forces, strains and strain rates. Actually the physical simulation, as compared with full-scale industrial testing, allows in a fraction of time for a fraction of cost an improvement of existing technology or development of a new one for modern materials and products. It can be used for solving production problems due to solidification phenomena or deformability limits, which result in hot cracking and rejection of the product. In this paper several examples of physically simulated procedures are given and their physical background discussed.

Key words: physical simulation, Gleeble thermal simulator, deformation, hot cracking, welding, casting

Rast zahtev po boljših in bolj učinkovitih metalurških procesih stimulira po vsem svetu intenzivne raziskave, kako doseči te cilje, ker so za tak namen nesprejemljivi realni industrijski poizkusi. Zmanjšanje RR-stroškov in hitro uvedbo novih tehnologij dosežemo, če uporabimo fizikalno in numerično simulacijo procesov. Računalniška simulacija je natančna, če uporablja prave podatke o vedenju materiala v procesnih razmerah. Da bi te podatke pridobili, je potrebna fizikalna simulacija, ki se izvrši na večnamenski termomehanični preizkusni napravi, ki natančno reproducira pogoje realnega industrijskega procesiranja. Za neprekinjeno litje in oblikovanje kovin je treba upoštevati različne faze procesov, ki se odvijajo v več stopnjah, ki jih karakterizirajo čas, temperatura in uporabljene sile, deformacije in hitrosti deformacije. Fizikalna simulacija, če jo primerjamo z industrijskim preizkusom v polnem obsegu, omogoči, da se v delcu časa za del stroškov doseže izboljšanje sedanje tehnologije ali razvoj nove za moderne materiale in proizvode. Uporabljamo jo lahko za rešitev proizvodnih problemov povezanih s strjevalnimi pojavi ali z mejnimi deformacijami, ki povzročijo vročo pokljivost in izmeček proizvodov. V tem članku predstavljamo primere fizikalno simuliranih procedur in razpravljamo o njihovem fizikalnem ozadju.

Ključne besede: fizikalna simulacija, Gleeblejev termični simulator, deformacija, vroča pokljivost, varjenje, litje

1 INTRODUCTION – PHYSICAL SIMULATION OF WELDING

Historically, welding was the first metallurgical process successfully studied by the simulation technique, in particular the use of simulated thermal cycles to reproduce the situation occurring in parent plate material affected by heat generated during welding. Further development of this technique led to the introduction of several testing procedures aiming to exactly replicate various situations in the weld metal or between the welded joint and adjacent material, in particular these occurring due to the stress relaxation and plastic accommodation processes during multiple heat cycling characteristic of multi-pass welds. The necessity to apply physical simulation for studying ductility and fracture behaviour of heat-affected zones of welds, occurred just after WW-II and was associated with low ductility of the weld heat-affected zone in high-strength steels introduced to shipbuilding [1]. In 1949 the first weld thermal-cycle simulator was built and utilized to generate uniform heat-affected zone microstructures through the CVN-sample for impact testing [2]. At that time, using the simulation, the results of impact strength appeared to be often better than on real welds. This discrepancy initiated more detailed studies on physical phenomena standing behind the toughness of weldments, which studies revealed the role of thermal gradients in affecting phase transformations and generating crystallographic lattice defects to plastically accommodate various micro-strains. Accordingly, the weld thermal-cycle simulator was equipped with a mechanical system capable to deform specimens with adequate speed at exact temperatures. When this was done, the Gleeble thermal-mechanical simulator was born [3]. Since 1957, when the first commercial Gleeble was produced for the purpose of weldability studies, it underwent several metamorphoses and the recent dynamic thermal-mechanical simulators allow the use of physical simulation techniques not only for welding but also for other industrial application processes, such as high strain rate multi-step hot forming with all kinds of thermal-mechanical processes, melting and controlled solidification for the purpose of conventional and continuous casting as well as semi-solid processing, checking for susceptibility

to hot cracking and embrittling, studying sintering, stress relaxation, accelerated creep, thermal-mechanical fatigue, and others.

The main concept of the thermal-mechanical simulator, however, has not been changed much since the beginning, and the actual Gleeble system [4] comprises: an AC electric resistance heating system as it was originally, a mechanical deformation system which earlier was pneumatic and now is servo-hydraulic, a vacuum and/or controlled atmosphere working chamber, and like in all the most recent testing equipments the computer control plus data acquisition and processing. For specific applications it may comprise various working units and attachments. And like at the beginning, the main aim of the physical simulation is to exactly reproduce the thermal and mechanical situation of the workpiece material as it appears in real processing, and to obtain identical microstructures as well as mechanical properties of the physically simulated materials.

1.1 Weld heat-affected zone

In the historical case of welding and its vulnerable to embrittlement and cracking heat-affected zone (HAZ), during the electric arc action a short thermal cycle appeared comprising a rapid heating, followed after reaching peak temperature by a cooling due to heat flow from the hot zone of the weld towards the cooler bulk of the material. The heating and cooling rates result from the balance between the energy input and the heat flow, and are controlled by thermal gradients between the hot zone of the weld and the parent plate. During the thermal cycle the electric current flows through the HAZ and the heat flows from the fusion surface between the weld and the plate to form isothermal planes perpendicular to this main direction of the heat flow, as schematically presented in **Figure 1**. This situation has to be reproduced on a bar-like sample in which a narrow uniformly heated zone is formed in the middle due to the thermal balance between the electric heating and the heat flow towards cold copper jaws, producing real temperature gradients, **Figure 2**. During the weld thermal cycle, a part of the HAZ material at first expands on heating and during this is compressed being restrained crosswise by the cold portions of the parent material, while in the second portion of this cycle the faster cooling down portions of thermal gradient zones once again compress it. In this second part of the thermal cycle also tensile strains appear, in particular in the main direction of the

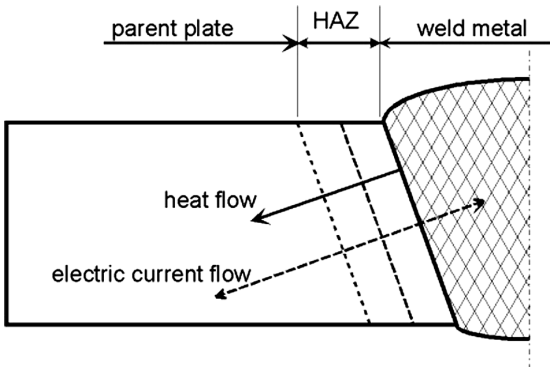

Figure 1: Schematic situation of the heat-affected zone in an arc weld with electric current flow and heat flow.

Slika 1: Shema položaja zone toplotnega vpliva pri elektrobločnem varjenju s smerjo toka toplote

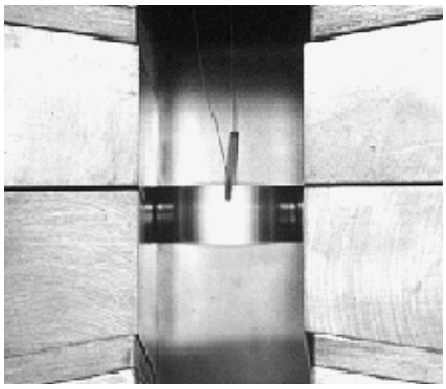

Figure 2: Weld HAZ simulation in Gleeble on 10mm diameter round-bar sample mounted in "cold" copper jaws.

Slika 2: Simulacija v Gleeblejevi napravi za toplotno zono zvara 10 mm na okrogli palici, pritrjeni v hladnih bakrenih čeljustih

a)

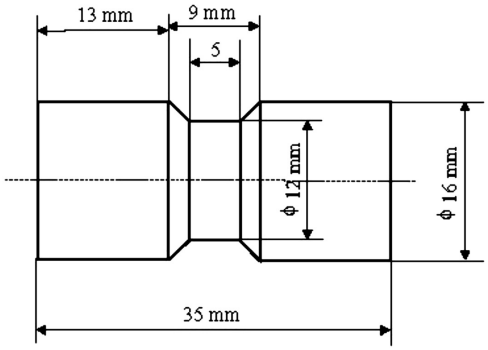

b)

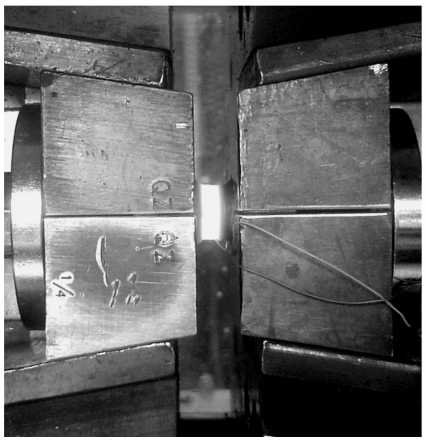

Figure 3: Schematic drawing of Gleeble sample for laser dilatometer studies of phase transformations in steels with cooling rates up to 200 °C/s (a) and this sample mounted in Gleeble's "cold" Cu jaws (b)

Slika 3: Shematična oblika Gleeblejevega preizkušanca za laserki dilatometrski študij faznih transformacij v jeklu s hitrostjo do 200 °C/s (a) in preizkušanec pritrjen v Gleeblejevih hladnih bakrenih čeljustih (b)

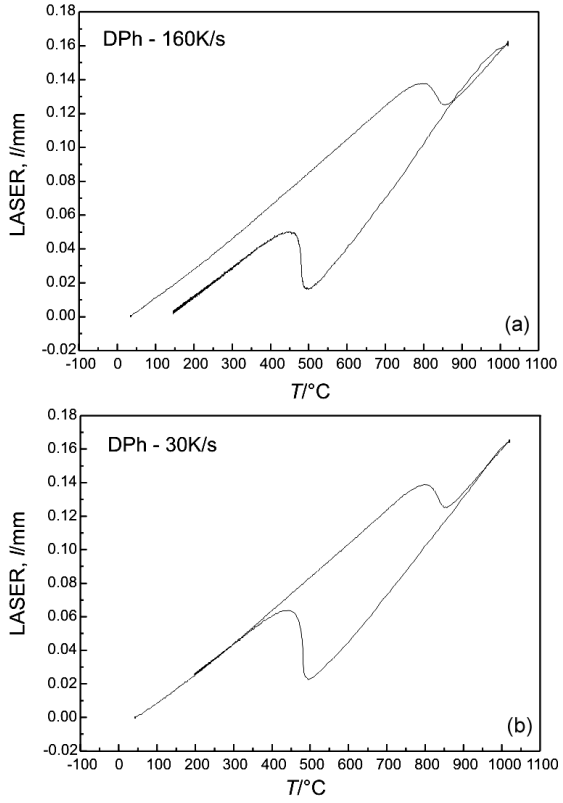

Figure 4: Laser dilatometer curves of HSLA steel heated up in Gleeble to 1020 °C and cooled by heat flow to Cu jaws with rate of 160 °C/s (a) and with rate of 30 °C/s (b).

Slika 4: Laserke dilatometrske krivulje jekla HSLA, ki je bilo v Gleeblejevi napravi segreto na 1020 °C in ohlajeno s pretokom toplote v čeljusti s hitrostjo 160 °C/s (a) in s 30 °C/s (b)

heat flow, and these may assist embrittlement due to generation of dislocations and interaction of these with interstitials [4], or even initiate intergranular cracking.

The magnitude of crosswise deformation due to thermal gradient, which in the case of a stiff real component may result in substantial residual stresses, can be illustrated in the following test. On the sample like in **Figure 3**, tested for phase transformations by contactless laser dilatometer, at the cooling rate of 160 °C/s obtained in the hot gauge zone by heat transfer to cooler mounting portions of the sample fixed in cold copper jaws of the Gleeble, a permanent shrinkage of diameter occurs after the thermal cycle, **Figure 3**. At lower cooling rates of 30 °C/s and less, which produce weaker temperature gradients, such permanent change of sample's diameter may be negligible, **Figure 4**.

1.2 Stress-relief embrittlement

An important demand for the successful physical simulation is its practical accuracy. Certain physical phenomena cannot be detected or studied on samples of wrong size or improper geometry, and then the sensitivity of the testing system must be adequate. Moreover, the physical background of the studied phenomenon must be well known, to properly design the experiment.

Here an example is given from a study on stress-relief embrittlement, occurring in some micro-alloyed HSLA steels and weld metals after post-weld heat-treatment. The stress relieving PWHT carried out at 600 °C converts prior fully acicular ferrite microstructure of the HSLA weld to partly recrystallised one, **Figure 5**, which is brittle and fractures in an intercrystalline mode along columnar crystals of the weld metal, **Figure 6**. This stress-relief embrittlement was associated with initial configuration of crisscrossing $a/2<111>$ screw dislocations, **Figure 7**, dominating in ferrite grains along the boundaries of prior columnar grains, and interaction of these dislocations with interstitials to form meta-stable $a<001>$ edge dislocations [5]. The saturated by interstitials $a<001>$ edge dislocations are mobile and able to enter the columnar grain boundaries to deposit there the interstitials, thus sensitizing these boundaries. An example of such boundary is given in **Figure 8**. Non-embrittling HSLA weld metals of very similar chemical compositions had another initial dislocation substructure and during the stress-relief annealing mainly generated large amount of tangled $a/2<111>$ edge type accommodation dislocations.

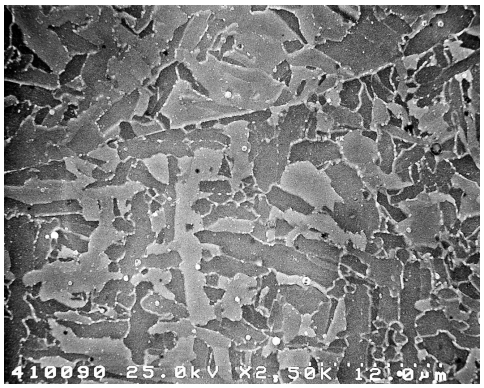

Figure 5: Microstructure of transformed acicular ferrite of HSLA weld metal, showing grain boundary of prior columnar crystals

Slika 5: Mikrostruktura iz transformiranega acikularnega ferita v zvaru jekla HSLA, ki prikazuje meje primarnih stebrastih kristalnih zrn

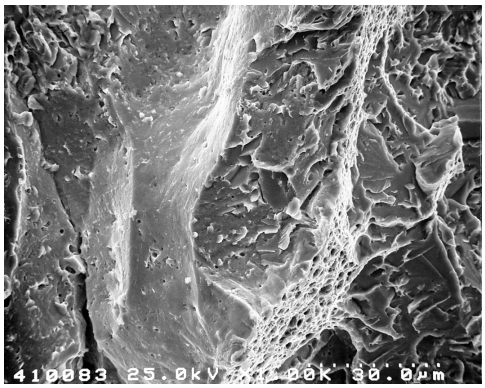

Figure 6: Brittle intergranular and transgranular fracture surface of the stress-relief annealed HSLA weld metal

Slika 6: Krhka intergranularna in transgranularna prelomna površina v napetostno žarjenem zvaru HSLA-jekla

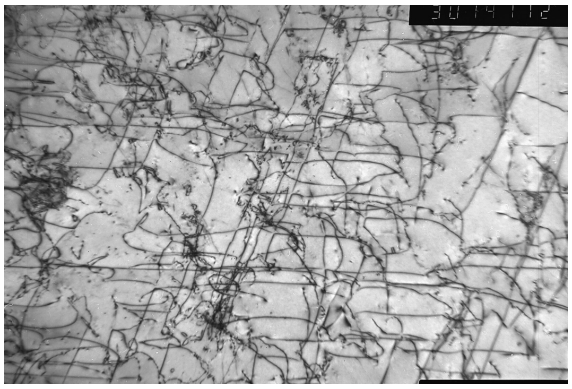

Figure 7: Configuration of criss-crossing screw dislocations dominating in ferrite of the stress-relief embrittling weld metal
Slika 7: Konfiguracija križajočih se vijačnih dislokacij, ki prevladujejo v feritu v zvaru, občutljivem za popustno krhkost

Testing on Gleeble for susceptibility to stress-relief embrittlement comprises 3-step thermal cycling applied on bulk samples of 10 mm to 12 mm diameter, while recording diameter by crosswise contactless laser dilatometer; the setup of this test is schematically shown in **Figure 9**. The laser dilatometer readouts from austenitic stainless steel sample show no changes of its dimensions during such thermal cycling, **Figure 10**.

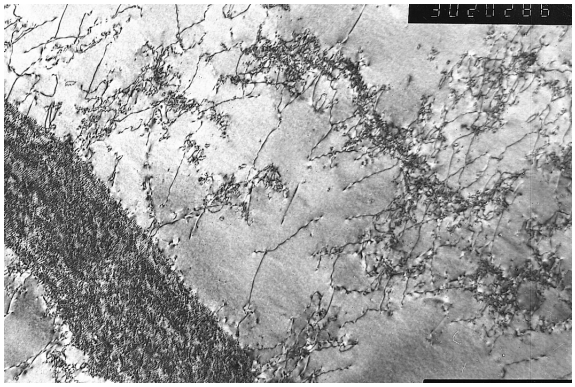

Figure 8: Sensitized grain boundary containing high density of dislocations and fine precipitates in embrittled HSLA weld metal
Slika 8: Sensitivirana krstalna meja z veliko gostoto dislokacij in majhnih izločkov v krhkem zvaru HSLA-jekla

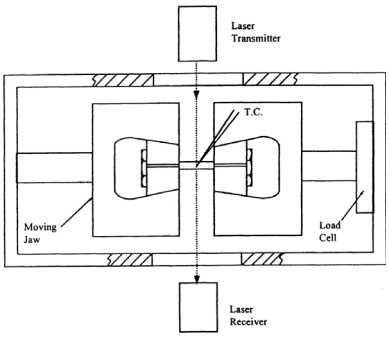

Figure 9: Schematic of laser dilatometer measurement on sample mounted in Gleeble
Slika 9: Shema meritve z laserskim dilatometrom za vzorec v Gleeblejevi napravi

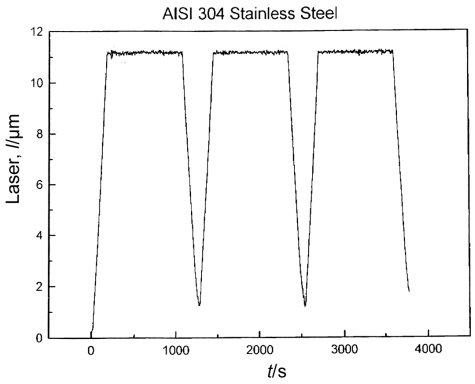

Figure 10: Result of laser measurement during 3-step thermal cycling of austenitic stainless steel
Slika 10: Rezultati meritev z laserskim dilatometrom pri termičnem cikliranju avstenitnega nerjavnega jekla v treh korakih

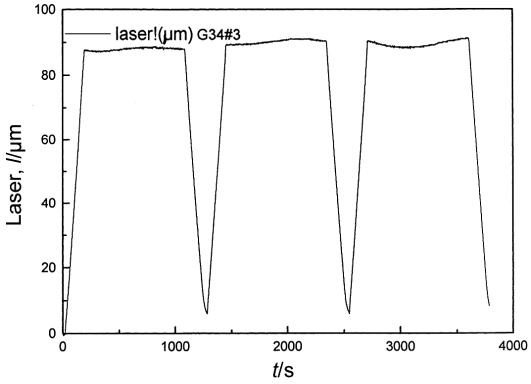

Figure 11: Laser measurement during thermal cycling of non-embrittling HSLA weld metal
Slika 11: Laserske meritve med termičnim cikliranjem zvara HSLA-jekla brez pojava krhkosti

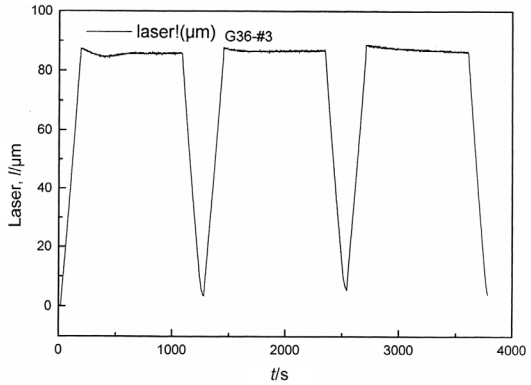

Figure 12: Laser measurement during thermal cycling of embrittling HSLA weld metal
Slika 12: Laserske meritve med termičnim cikliranjem zvara HSLA-jekla z pojavom krhkosti

Samples of a non-embrittling HSLA weld metals during the hold periods of thermal cycles show increase of diameter, **Figure 11**, due to mainly generation of accommodation dislocations, while the embrittling HSLA weld metals in the first cycle show tempering of acicular ferrite (bainite) and in further cycles a steady

decrease of diameter, **Figure12**, associated with reaction of *a*/2<111> screw dislocations into the meta-stable *a*<001> edge dislocations (decrease of density by the factor of ≈2.4) followed by annihilation of the last, mostly within the grain boundaries.

1.3 Hot ductility and hot cracking

One of the main problems of weldability is the susceptibility of some welds to hot cracking, as welding is the technology of joining materials by bringing them locally to the molten state and then solidifying this region. At high temperatures just below solidus most of metal alloys suffer loss of strength and ductility. This occurs on heating due to liquation before reaching the fully molten state and then on cooling from the melt it persists within certain range of temperatures after solidification, called brittle temperature range – BTR. As the solidified alloy becomes stiff while not yet ductile, hot cracks may form on cooling, when tensile strains caused by shrinkage and assisted by restraint cannot be compensated by ductility of this alloy. Accordingly, the method of studying susceptibility of an alloy to hot cracking involves tensile testing at the conditions simulating these of the real welding (or casting) process. The use of thermal-mechanical simulator like Gleeble, able to reproduce on a specimen the welding thermal cycle and impose a strain in a controlled manner, allows achieving this goal.

Hot tensile test

Testing on Gleeble for susceptibility to weld liquation cracking / HAZ hot cracking, is the hot tensile testing of a number of specimens on-heating and then on-cooling, and determining their hot ductility measured as a reduction in area at the specimen's neck portion after the test. This procedure is schematically presented in **Figure 13** [6].

The hot ductility of a welded alloy increases gradually with increase of testing temperature from ambient towards melting point, however, before reaching this point it drops abruptly from certain maximum to nil. Just above this nil ductility temperature (NDT) is the nil strength temperature (NST) at which the alloy looses its strength due to liquation i.e. formation of weak or liquid phases along grain boundaries. The real physically measurable melting temperature of such alloy – TL, is higher than NST. On-cooling from the melt or from the NST, the ductility does not recover exactly at NDT only below it at so-called ductility recovery temperature – DRT. The temperature span from NST to DRT is considered to be the brittle temperature range – BTR, the extent of which can be used as a rough criterion of the susceptibility to hot cracking.

More exact criterion of this susceptibility is the measure how fast does the ductility recover on-cooling as compared with its decrease on-heating. As reference point for this measurement the maximum of ductility from the on-heating ductility curve is taken and the representative areas below the on-heating and on-cooling curves are compared, **Figure 14** [7]. Arbitrarily considering 5 % of reduction-in-area on-cooling as the ductility recovery point and comparing the hot ductility curves on-heating and on-cooling, the nil ductility range (NDR), ductility recovery rate (DRR) and ratio of ductility recovery (RDR) can be determined to exactly characterize the susceptibility of an alloy to hot cracking.

The reference point for the hot ductility measurements determining the susceptibility to liquation cracking is the nil strength temperature. This temperature has to be used as a peak of the welding thermal cycle, on-cooling after which the hot tensile tests should be run. To measure the NST on Gleeble an attachment is used, schematically presented in **Figure 15**. This NST attachment keeps the specimen under a constant tensile load of about 50 N while allowing its heating-up with an initial heating rate the same as of the welding thermal cycle to be simulated up to a temperature 50 °C below the solidus temperature of the material, then change to a heating rate of 2–5 °C/s until the NST is reached, as shown in **Figure 16**.

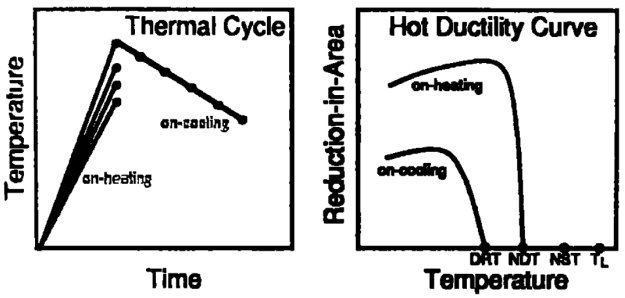

Figure13: Schematic of Gleeble's procedure for hot cracking, including hot tensile testing on-heating up to NST and then on-cooling after weld thermal cycle with NST as the peak temperature [6]

Slika 13: Shema Gleeblejeve procedure za vročo pokljivost, ki obsega vroč raztržni preizkus s segrevanjem do NST in ohlajanje po termičnem ciklu varjenja z NST kot najvišjo temperaturo [6]

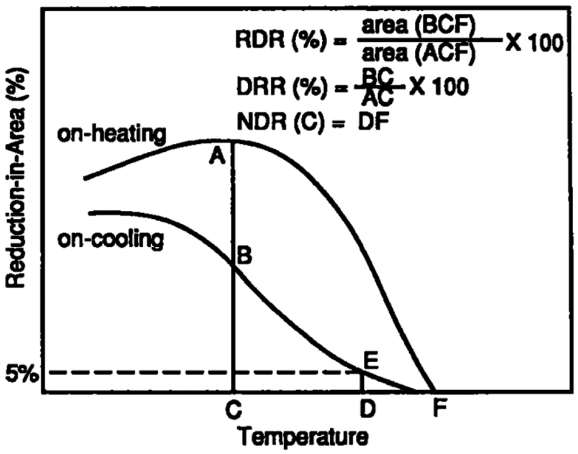

Figure 14: Evaluation of hot ductility curves for the hot cracking susceptibility [7]

Slika 14: Ocena krivulj vroče duktilnosti za občutljivost za vročo pokljivost [7]

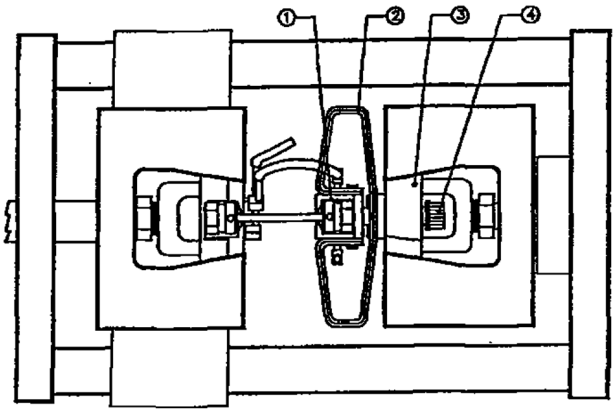

Figure 15: Nil strength attachment of Gleeble using trapezoidal spring grip maintaining constant small tensile load on specimen during heating

Slika 15: Shema montaže brez sile v Gleeblejevo napravo s prijemom z uporabo trapezoidalne vzmeti, ki ohranja konstantno majhno natezno napetost med ogrevanjem preizkušanca

To avoid mixing-up of phenomena related to liquation cracking with these of solidification cracking, in order to measure only the hot ductility region responsible for the liquation cracking, the NST must not be exceeded in the simulated weld thermal cycles.

To test for the susceptibility to solidification cracking, controlled melting and solidification of a rod-like specimen can be carried out on Gleeble, and after the solidification the hot ductility is determined in the manner like described above. Here the ability of Gleeble to melt electrically conductive specimens is used. In this test the central portion of the specimen protected by a crucible / quartz sleeve is brought to a temperature above solidus and then this crucible contains the molten / semi-liquid metal, as shown in **Figure 17**. Thermal gradients between the molten portion and mounting jaws prevent the metal from flowing out of the crucible while controlled thermal cycle allows conducting the solidification in a manner similar to that of

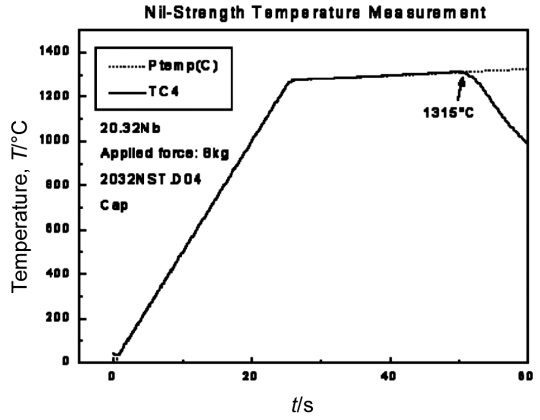

Figure 16: Time – temperature graph of Gleeble test for nil strength temperature

Slika 16: Graf čas – temperatura Gleeblejevega preizkusa za temperaturo ničelne trdnosti

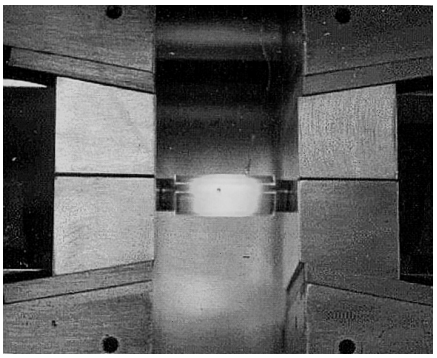

Figure 17: Gleeble's setup for controlled melting and solidification study

Slika 17: Gleeble postavitev za raziskave kontroliranega taljenja in strjevanja

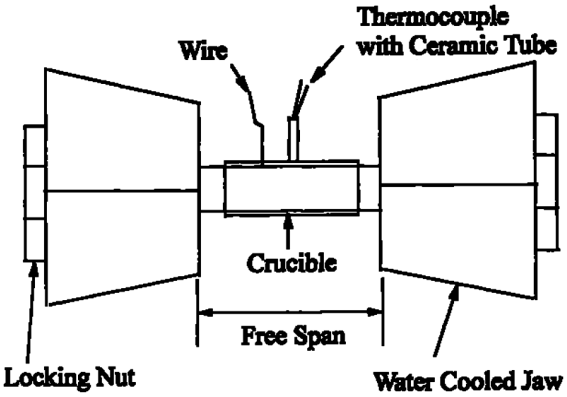

Figure 18: Schematic of **Figure 17**, with end nuts for hot tensile testing

Slika 18: Shema **slike 17** s končnimi vijaki za vroč natezni preizkus

real casting or welding. Schematic of the assembly used for this purpose in Gleeble is given in **Figure 18**.

More details of the Gleeble testing for liquation and solidification cracking can be found in IIW document No. II-C-042A/95 [8]. The Gleeble testing procedures are also mentioned in the technical report CEN ISO/TR 17641-3:2003, under the chapter "Hot Tensile Test" [9].

The SICO test

An alternative procedure to study susceptibility to solidification cracking on Gleeble is the strain-induced crack opening test – SICO, developed at Dynamic Systems Inc., in USA, for studying hot deformability of alloys. In this test the central hot portion of the Gleeble specimen is compressed to form a bulge, **Figure 19**, on outer perimeter of which cracks appear at the critical secondary tensile strain, **Figure 20**. The critical strain to fracture in SICO test is defined as the hoop strain at onset of cracking in the bulge zone:

$$\varepsilon_c = \ln (D_f/D_o)$$

where D_o is the initial diameter of the specimen, while D_f is the final maximum diameter in the bulge zone.

As during the controlled melting and solidification in Gleeble the dendritic crystals mostly grow from the direction of the main heat flow i.e. in the axial direction,

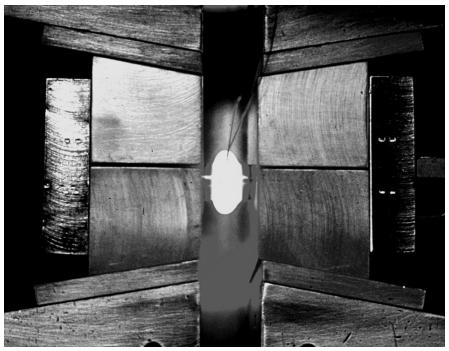

Figure 19: SICO sample tested in Gleeble
Slika 19: SICO-preizkušanec med preizkusom na Gleeblejevi napravi

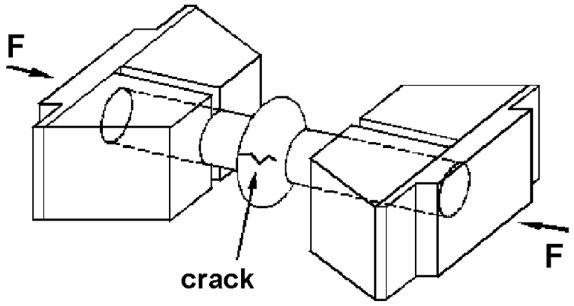

Figure 20: Schematic of SICO test showing crack formed on bulge portion of sample
Slika 20: Shema SICO preizkusa z napako na izbočenem delu preizkušanca

the mid-span segregation may occur in the specimen causing deep and partly hidden cracking of the SICO specimen along the central plane perpendicular to the compression axis, **Figure 21**. In such situation it is advised to check for the true critical diameter on the cross-section of SICO sample, like it is shown in **Figure 22**.

As the hot tensile testing on Gleeble gives the adequate characteristics of an alloy regarding its hot cracking susceptibility, the SICO test appears to be more accurate for measuring of critical strains to fracture and related critical strain rates.

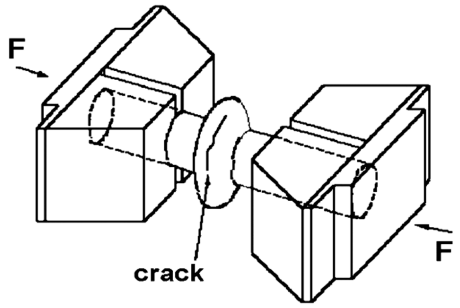

Figure 21: Central plane crack in SICO often appearing after melting and solidification
Slika 21: Razpoka v centralni ravnini na SICO-preizkušancu, ki pogosto nastane po taljenju in strjevanju

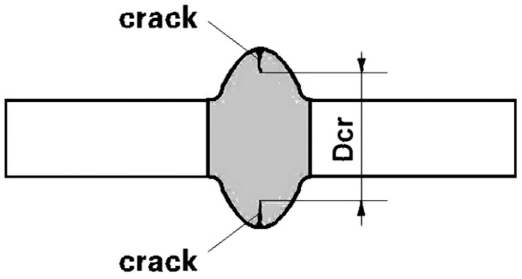

Figure 22: Method of measuring critical diameter *D*cr when central plane crack appears
Slika 22: Metoda za merjenje kritičnega premera *D*cr v primeru razpoke v centralni ravnini

2 SIMULATION OF CASTING

The physical simulation actually plays an important role in the design and application of the most efficient industrial manufacturing process, which is the continuous casting and the hot rolling following it. As shown in **Figure 23**, in different stages of process may occur flaws such as shrinkage cavity, centre-line porosity, facial and corner cracks [10]. Physical simulation can be used to determine flawless processing parameters, without interrupting of production.

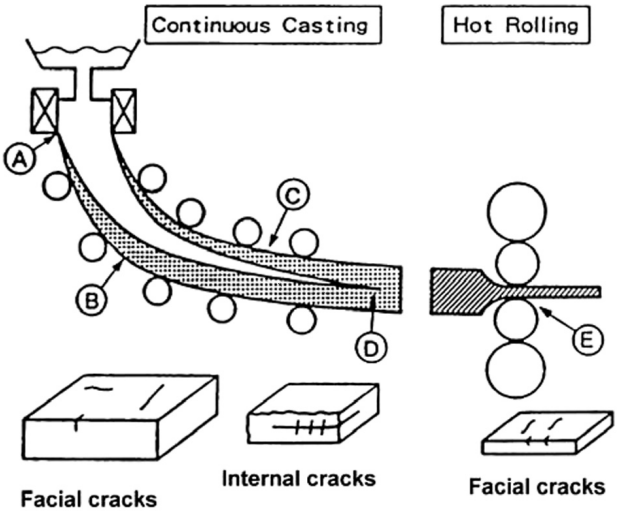

Figure 23: Schematic of continuous casting and hot rolling processes [10]
Slika 23: Shema neprekinjenega litja in vročega valjanja [10]

2.1 Controlled solidification and semi-solid processing

In the first phase of process like schematically shown above, the liquid metal is poured into a crystallizer chamber in which its outer shell has to solidify to the extent securing the liquid core inside. When a vertically cast slab or billet has to be bent into horizontal position, the ductility of outer shell must allow this. Gaining physical data for such operation includes melting and solidifying of numerous samples in the manner like presented in **Figures 17 & 18**, and hot tensile testing

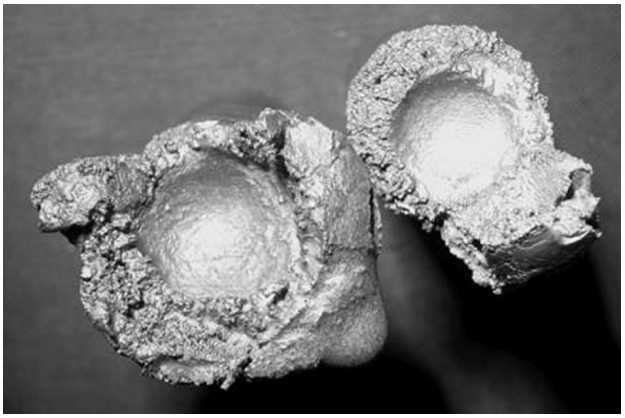

Figure 24: Sizes of solidified outer shell and molten pool in 25 mm SICO bar melted at 1465 °C and then compressed at 1420 °C surface temperature, while the middle temperature being of ≈1450 °C
Slika 24: Velikosti strjene zunanje lupine in talilne kopeli v 25 mm SICO-palici, ki je bila staljena pri 1465 °C in krčena pri temperaturi površine 1420 °C, ko je bila temperatura v sredini ≈1450 °C

them at various temperatures after solidification, to create hot ductility maps [10].

An alternative test comprises melting of a 25 mm diameter bar and deforming it by compression after a partial solidification. The heating-cooling balance of Gleeble causes in the sample thermal gradient to occur keeping molten core inside when outer shell solidifies. The test called 25 mm SICO gives critical strain to fracture, strain rate and temperature, and in the case of incomplete solidification reveals thickness of outer shell on crashed sample, **Figure 24**.

Distribution of strains in the SICO sample can be determined by numerical simulation [11]. Having known the strain distribution and temperature gradient as well, valuable information can be gained from cross section of the sample like given in **Figure 25**: cracks at maximum perimeter occurred at temp of 1385 °C and 0.35 strain with 0.5/s strain rate, then no-crack zone at ≈0.5 of radius appeared representative to temperature ≈1400 °C and strain of 0.2, and once again cracks in the middle of the sample were formed representative to strain ≈0.05 at temperature of ≈1425 °C, the last is the nil ductility temperature of the tested steel.

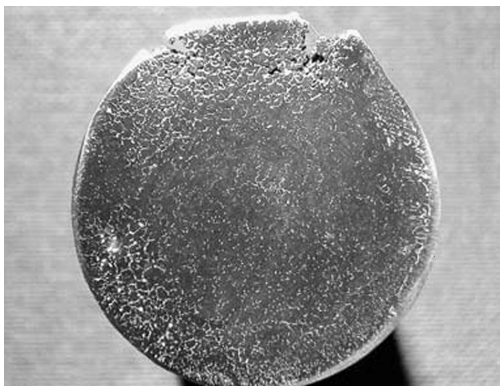

Figure 25: Cross-section of SICO sample showing deep cracks along perimeter and cracks in the middle, with flawless zone in between
Slika 25: Prečni prerez SICO-preizkušanca z globokimi razpokami vzdolž oboda in razpokami v sredini z področjem brez napak med obema

2.2 Direct casting and rolling

The recent development in continuous casting consists of thin strip casting followed directly by hot rolling while retaining the heat of the melt. For simulation of such process the dedicated HDS-V40 physical simulator has been built [4,12], allowing on one specimen after melting and solidification with controlled dendrite size and growth direction to perform multi-step high rate deformations representative to multi-stand rolling. The process comprises resistance heating of a bulk 10 mm thick, 50 mm wide and 165 mm long specimen in a specifically designed crucible, to melt the central portion of this specimen and then to solidify it in a controlled manner, and then to deform its central portion by heated plane strain anvils perpendicularly to the lengthwise axis. Upon melting and subsequent cooling a thin shell forms around the molten material and as soon as it appears the melting crucible is pulled away from the specimen to allow for deformation. Schematic of this process is given in **Figure 26**. Multiple hit deformations by plane strain compression, **Figure 27**, can then be performed on the material while it is in the solid or semi-solid state. Resulting from the simulation is the flat bar, **Figure 28**, with central deformed zone (5), transient zone (4) and side zones of reheated in solid state coarse-grained material (1), mushy zone (2) and fully melted (3) material; in this picture marked by hatching are sections used in subsequent metallographic examination.

The reliability of the melting and solidification procedure can be discussed in terms of non-metallic inclusions before and after the experiment. The specimen made of 0.2 % C plain carbon steel, had in the initial

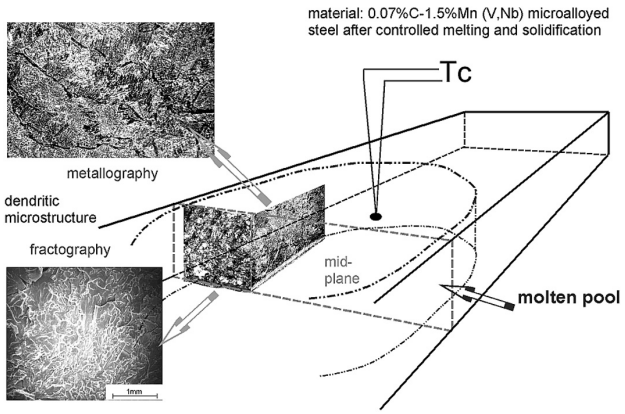

Figure 26: Schematic of the melting and solidification test in HDS-V40 simulator, showing the site and shape of the molten pool and then formed columnar crystals as visible on longitudinal section and on fracture in the mid-plane
Slika 26: Shema talilnega in strjevalnega preizkusa v HDS-V40 simulatorju, ki kaže mesto in obliko staljene kopeli in nato nastalih stebrastih zrn, kot se vidijo na vzdolžnem prerezu in na prelomu v srednji ravnini

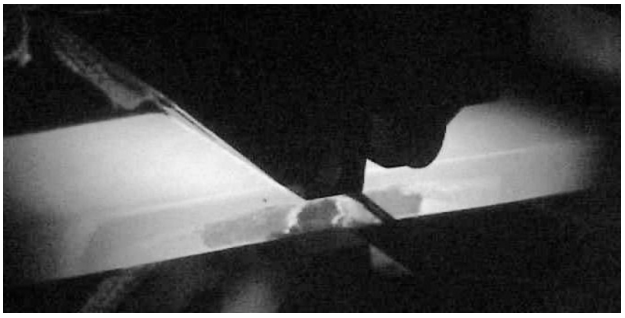

Figure 27: Hot central zone of specimen and plane strain anvils in the working chamber
Slika 27: Vroča centralna zona preizkušanca in čeljusti za napenjanje v delovni komori

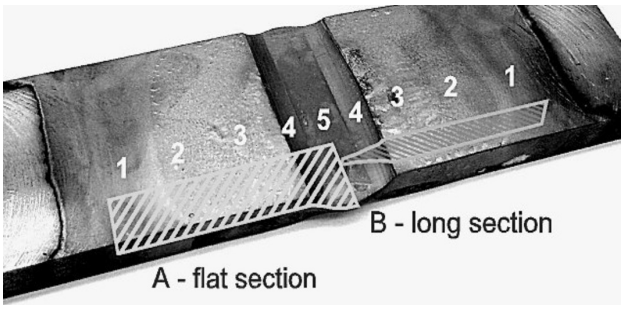

Figure 28: Specimen after simulation of melting and direct hot rolling
Slika 28: Preizkušanec po simulaciji taljenja in direktnega vročega valjanja

state a ferritic-pearlitic microstructure with bands elongated in rolling direction and so extended non-metallic inclusions. After the test, in the entirely melted and solidified "as-cast" zone-3, chains of spheroidal inclusions dominated along boundaries of dendrites, **Figure 29**. On fracture through mid-plane of the as-solidified specimen, which coincides with the mid-plane of the former molten pool, individual dendritic crystals are seen, **Figure 30**, with their lengths of up to 2.0 mm. This size of dendrites

Figure 30: Cleavage fracture along mid-plane of specimen, showing sizes of dendritic crystals
Slika 30: Cepilni prelom vzdolž centralne ravnine preizkušanca, na katerem vidimo velikost dendritnih zrn

Figure 29: Fine spheroidal inclusions in grain boundary ferrite of dendritic crystals
Slika 29: Fini sferični vključki v feritu po kristalnih mejah dendritnih zrn

well coincides with the length and width of dendritic crystals appearing in the thin continuously cast slabs manufactured in the industrial processes [13].

3 SIMULATION OF HOT DEFORMATION

Two major hot deformation procedures: forging and rolling, have to be physically simulated in a different manner, due to differences in main force direction, main strain direction and heat flow, as schematically given in **Figure 31**. Thus to simulate forging an axial compression / flow stress test is used, while for simulation of rolling the plane strain compression has to be applied.

3.1 Multi-step deformation

An exact simulation of multi-step hot rolling by plane strain compression test requires constant strain rates to be maintained in each step with an instantaneous stop at

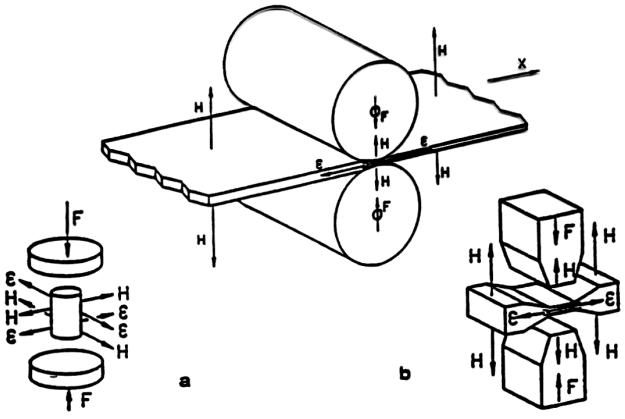

Figure 31: Schematic presentation of a roll stand and simulation of deformation by: (a) flow stress test, and (b) plane strain test. The letters denote: F – compression force; H – heat flow direction; ε – strain direction: X – rolling direction [14]
Slika 31: Shema valjalniškega ogrodja in simulacija s: (a) preizkusom meje tečenja in (b) z ravninskim deformacijskim preizkusom. Črke pomenijo: F – tlačna sila, H – smer toka toplote, ε- smer deformacije, X – smer valjanja [14]

the end of deformation. To achieve such performance of the Gleeble's servo-hydraulic system, a dedicated deformation-assisting device called Hydrawedge was designed and implemented [14]. The Hydrawedge, synchronized with the main / primary deforming system, is acting as a flexible mechanical stop that allows the primary hydraulic ram to be stopped by running into an immovable object. In order to perform exact multiple compressions sequentially, for which the specimen must be moved since the main hydraulic ram will stop at the same point in space each time, the Hydrawedge is used to program the displacements. This allows to exactly control the amount of strain, while simultaneously and separately controlling the strain rate at which the sample is being deformed. Without such device, all fast servo-hydraulic machines or give substantial over-travel or must slow down before stopping at the right sample's height. In the first instance other than programmed strains are generated while in the last case final microstructures are generated characteristic of slower than programmed strain rates.

In **Figure 32** the schematic of Hydrawedge is given and in **Figure 33** its operation explained. In the system consisting of main power piston (M), punch with stop (P), yoke (Y), sample (S) and Hydrawedge piston (H), before deformation the system is in position like drawn in **Figure33**(a). Preparation to deformation includes pulling off the main piston (M) to form a gap "g" between it and punch (P). Simultaneously the Hydrawedge piston (H) pushes the sample (S) and punch (P) to set-up the amount of required deformation between the punch's stop ring and the yoke (Y), **Figure 33**(b). Finally in the deformation step, **Figure 33**(c), the main piston accelerates through the gap "g" reaching the required top speed, then during the deformation decelerates in a programmed manner to maintain constant strain rate, and when the stop of the punch (P) hits the yoke (Y), the deformation is finished with high accuracy. Such steps can be then repeated several times.

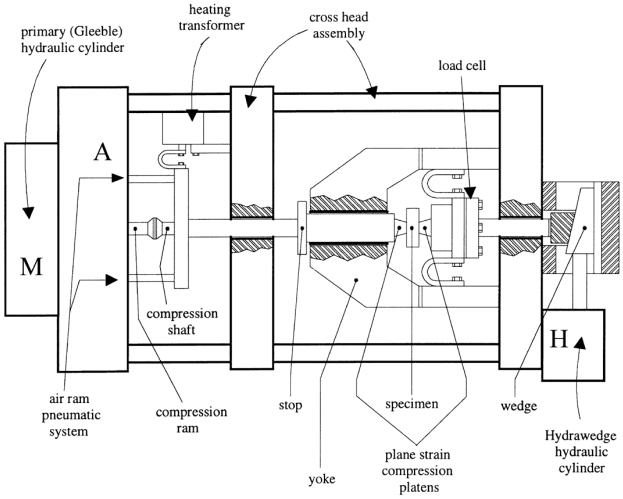

Figure 32: Schematic drawing of the Hydrawedge device [14]
Slika 32: Shema vlečenja na napravi Hydrawedge [14]

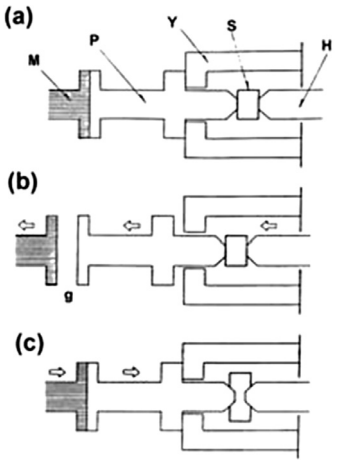

Figure 33: Hydrawedge operation
Slika 33: Preizkus Hydrawedege

Maintaining constant strain rates and instantaneous termination of each deformation step with an aid of Hydrawedge reveals true behaviour of the material under processing. Theoretical deformation behaviour assumes continuous strain hardening and increase of flow stress with decrease of deformation temperature, **Figure 34**. In reality, due to microstructure transformation processes like dynamic and static recrystallisations and precipitations overlapping with these, the true multi-step flow stresses are often much different, **Figure 35**.

An example, which follows, shows how the physical simulation can be used to generate various as-hot-rolled microstructures. A HSLA steel, used for manufacturing of hot rolled plates in a 7-step rolling process, as in **Figure 36**, with continuous drop of temperature, had an acicular ferrite / upper bainite microstructure with very uniform grain size across the plate thickness, given in **Figure 37**. On this steel an attempt was made by physical simulation on Gleeble, to refine grains, separate the phases, achieve a dual-phase microstructure, as well as to reduce amount of deformation steps in the rolling mill.

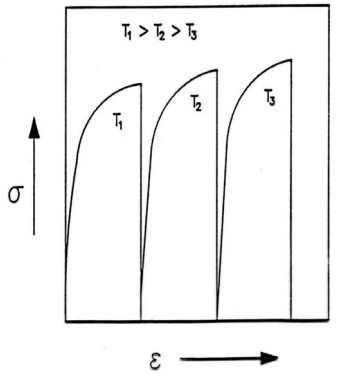

Figure 34: Theoretical flow stress curves of multi-step hot deformation
Slika 34: Teoretične krivulje tečenja pri vroči deformaciji v več stopnjah

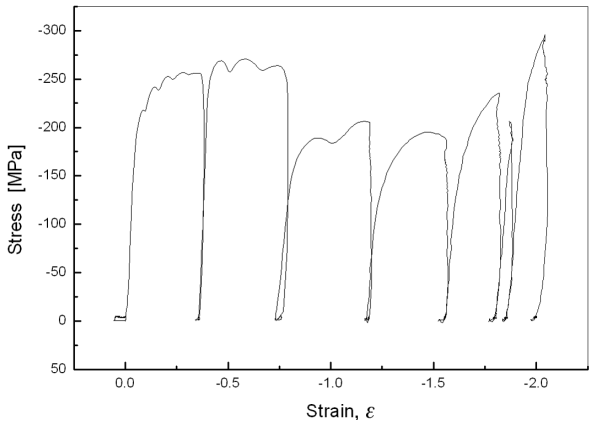

Figure 35: True stress-strain graph of the 7-step hot rolling simulated in Gleeble

Slika 35: Pravi graf napetost – deformacija simulacije valjanja v 7 vtikih v Gleeblejevi napravi

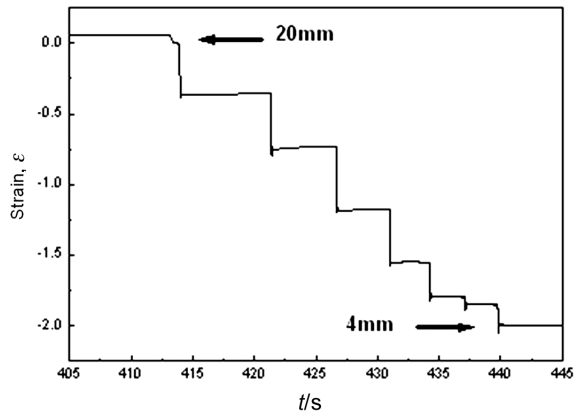

Figure 36: Strain vs. time of the 7-step rolling schedule simulated in Gleeble

Slika 36: Odvisnost deformacije od časa pri simulaciji valjanja v 7 vtikih v Gleeblejevi napravi

One of the methods to obtain the dual-phase microstructure is an intercritical annealing followed by accelerated cooling. An alternative is to stimulate by deformation the phase separation in the two-phase intercritical

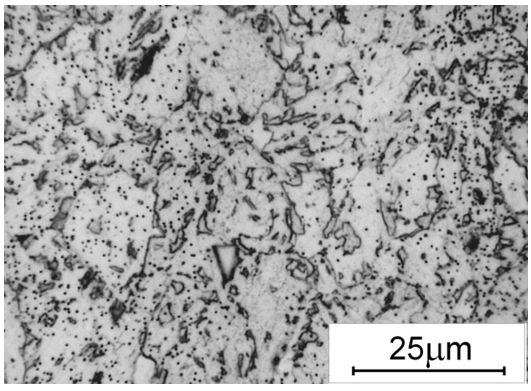

Figure 37: Microstructure of acicular ferrite / bainite with uniform distribution of carbides

Slika 37: Mikrostruktura iz acikularnega ferita/bainita z enakomerno porazdelitvijo karbidov

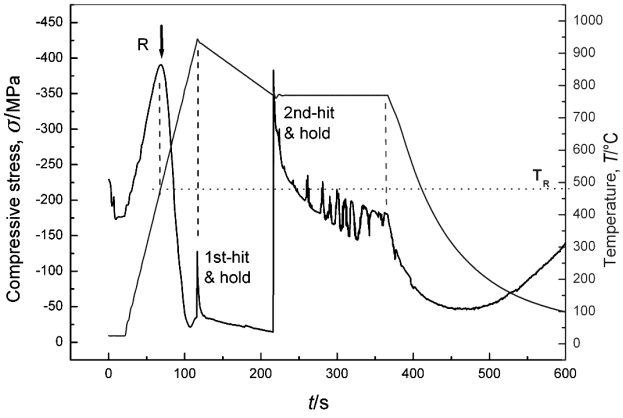

Figure 38: The 2-step deformation and relaxation test in the intercritical range followed by cooling, as simulated in Gleeble

Slika 38: Simulacija v napravi Gleeble za deformacijo v dveh korakih; preizkus relaksacije v interkritičnem področju ter hlajenje

austenite-ferrite range. The new requested continuous 5-step rolling procedure needed a proof that for the selected steel this would be achieved. The appropriate test on Gleeble comprised applying small strains after which the relaxation of sample was monitored. Two- and three-hit experiments were carried out with different time intervals after the hits. An example of a 2-hit experiment is displayed in **Figure 38**. A sample pre-loaded to 175 MPa compression stress at room temperature was heated with constant rate of 10 °C/s to above A_3 temperature in fixed Gleeble jaws, showing relaxation temperature of about 480 °C. After reaching 920 °C it was deformed by the first hit and then held to relax for 100 s while the temperature was constantly dropping. The second hit was executed at 770 °C and during the hold for 150 s after it the austenite-to-ferrite isothermal transformation effects were observed.

Further a free cooling was applied, during which at first the effects were observed of austenite-to-martensite transformation and then "stiffening" of the ferritic-martensitic microstructure.

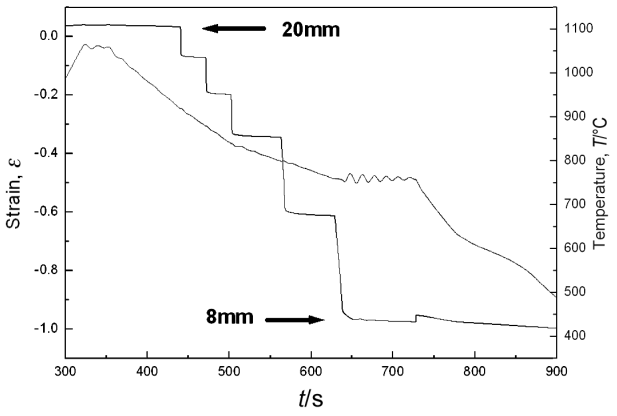

Figure 39: Strain vs. time and temperature profile of 5-step simulation to achieve fine-grained microstructure

Slika 39: Odvisnost napetosti od časa in temperaturni profil pri simulaciji v 5 korakih za dosego finozrnate mikrostrukture

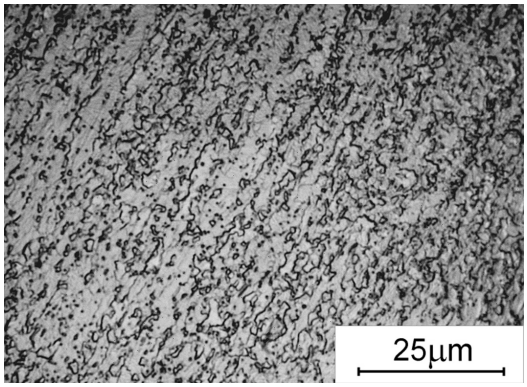

Figure 40: Fine-grained microstructure if the deformation bands after the 5-step rolling simulation in Gleeble

Slika 40: Finozrnata mikrostruktura v deformiranem pasu po simulaciji valjanja v 5 vtikih v Gleeblejevi napravi

The final 5-step rolling procedure, **Figure 39**, comprised three initial steps in austenite phase, maintaining strains, strain rates, as well as interpass times and temperatures adequate to preserve and/or to additionally stimulate precipitation of fine carbides. The last two steps were executed in the austenite-ferrite two-phase region according to the results from tests like this presented in **Figure 38**. The resulting fine-grained microstructure, which on plane strain samples reduced to only ≈1.0 total strain formed mainly in shear-bands, is shown in **Figure 40**. By an increase of strains in all five steps of this new rolling procedure the uniform fine-grained microstructure was obtained across the whole thickness of the plate.

3.2 Solving problems in hot rolling

Flawless rolling process requires that characteristic of the material strains to fracture got never exceeded. In hot deformation tests steeper temperature gradients cause apparent strengthening of the material and decrease of its ductility. In industrial manufacturing this phenomenon is often responsible for appearance of corner cracking of hot rolled billets. The lower temperatures of the corner region always appear, **Figure 41a**, and corner or near-corner cracks may occur when the flow of material to the corner of billet is hampered by the thermal gradients. This situation, schematically given in **Figure 41b**, shows how normal force and friction forces exerted by rolls cause the material flow in the rolling direction as well as towards the corners, while the plasticity of the material along the cooler corners may be limited. Solving of this problem requires hot strength and ductility data that might be provided by numerous hot tensile tests [14].

As an alternative to physically reproduce this situation, a two-step SICO test may be used (**Figure 42**). After forming a bulge in the first compression deformation, an air (or inert gas) blow is locally applied to produce the measured by two thermocouples *T*c1 & *T*c2 thermal gradient like in the real situation, and when this gradient is achieved the second compression is applied, with adequate second strain and proper strain rate, till the

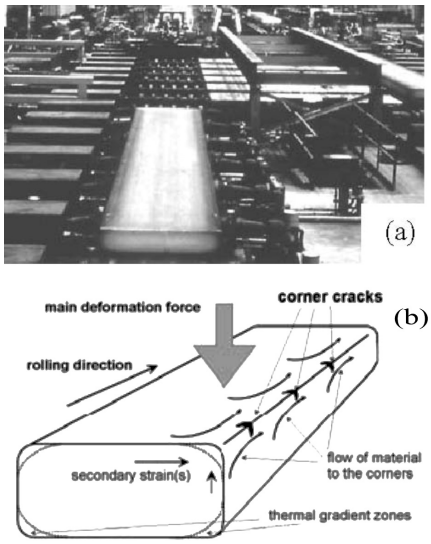

Figure 41: The real situation of hot rolled steel slab (a) with cooler corner portions, and its schematic explanation indicating the directions of main metal flow

Slika 41: Pravo stanje vroče valjanega slaba s (a) hladnejšimi vogali in shematsko označbo smeri glavnega toka metala

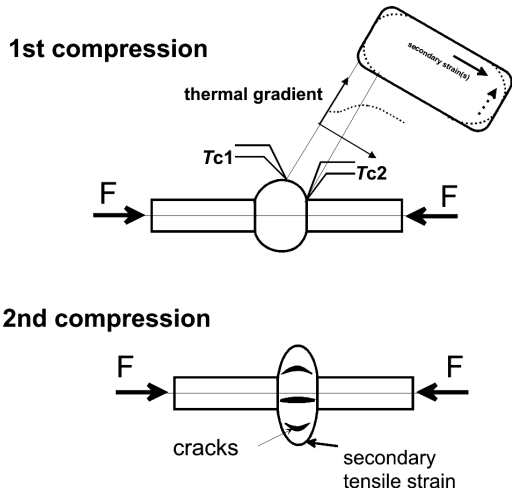

Figure 42: A two-step SICO test for susceptibility of hot rolled billets to corner cracking, including: the first compression to form a bulge, holding till the gradient appears and the final second compression

Slika 42: Dostopenjski SICO- preizkus občutljivosti vroče valjanih slabov za vogalne razpoke, ki obsega: najprej krčenje za nastanek izbokline, zadržanje do nastanka gradienta in nato drugo, končno krčenje

cracks appear. This procedure gives the amount of strain to fracture at the real strain rate, at controlled temperature and at real temperature gradient – it is not easy to gain all these data simultaneously in any other simple and continuous test.

4 THERMAL-MECHANICAL FATIGUE

The thermal-mechanical fatigue is a complex process often responsible for premature failure of components in power generation and chemical processing. In recent four decades microstructural features were identified,

which in novel creep resisting martensitic / ferritic steels accelerate precipitation of carbides and speed-up recovery and recrystallisation of matrix. Based on these evidences a low-cycle thermal-mechanical fatigue procedure called accelerated creep test (ACT) was developed on Gleeble. The ACT speeds-up microstructural changes by elasto-plastic tensile and compressive strains applied on the sample during thermal cycling in the temperatures characteristic of creep. It also uses the advantages of direct electric resistance heating, which is the heating mode implemented on Gleeble and also complies with the recent knowledge on development of dislocation substructures and their effect on precipitation processes in ferritic and multi-phase steels [15].

4.1 The accelerated creep test – ACT

The up to date ACT procedure complies with the following principles:

- The basic temperature and applied strains prevent odd transformations like e.g. secondary dissolution of carbides or intensive formation of non-equilibrium phases.
- The final deformation at fracture is like at real creep – just a few pct in total.
- The depletion of weld metal or steel matrix in alloying elements is achieved similar to that of crept steels and the carbide phases at onset of cracks are not different.

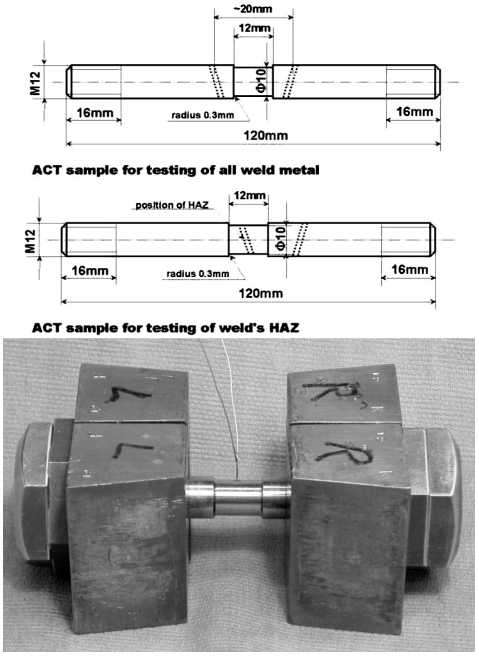

Figure 43: Schematic drawing of cross-weld samples used for ACT on all-weld-metal and on weld's HAZ, and mounting of the sample in Gleeble's jaws set

Slika 43: Shema križnih varilnih preizkušancev za ACT na metalu zvara in coni toplotnega vpliva zvara ter pritrditev preizkušanca v čeljusti Gleeblejeve naprave

Size and mounting of specimens in Gleeble allows a uniformly heated zone formed in the middle-span of the sample and the portion of material in this zone undergoes transformation. To better define this zone, gauge portion of a reduced diameter is made on the sample, **Figure43**.

The ACT was primarily invented for welded joints, in particular for repair welding. Its first larger application appeared in the 5thFP EU R&D project "SmartWeld" (2001–2004) and more recently in COST-536 and COST-538 EU actions.

The ACT samples mounted in the Gleeble's "pocket jaws" assembly, like in **Figure 44**, were subjected to programmed cycles of the low-cycle thermal-mechanical fatigue, run till failure or till pre-determined stress or strain. In homogeneous materials, often before the crack appearance on the surface, internal cracks were formed extending perpendicularly to the sample's axis. In microstructurally inhomogeneous samples the cracks usually followed the "weakest links" like the HAZs of the welds.

4.2 Results of the ACT

In the implemented low-cycle thermal-mechanical fatigue procedure on Gleeble data of stress, strain, strain rate and temperature as well as dilatometric information are recorded, out of which strain-time and stress-time graphs can be produced like these given below in **Figure 45**. Usually the tests are run till failure of specimen, however the test can be interrupted anytime and specimens for e.g. fine fractographic and microanalytical investigations taken before fracturing. As the tests for different materials are run at different temperatures and the response of material gives various stress equivalent to the YS at elevated temperature of the test, to compare the ACT results the duration of the test and its temperature can be included in the following parameter:

$$P_{\mathrm{ACT}} = (7 + \log t) \cdot T/100$$

where: t/ks = time of test, and T/K = temperature.

Then, the creep strength factor in ACT can be calculated as:

$$F_{\mathrm{ACT}} = P_{\mathrm{ACT}} \cdot R_{\mathrm{S}}/100$$

where R_S is the average stress of all ACT cycles measured during relaxation on tension.

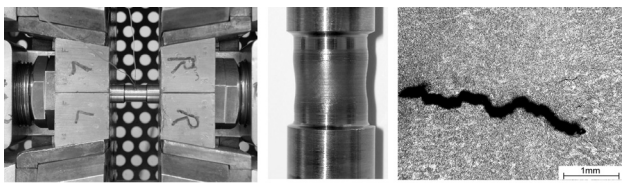

Figure 44: ACT sample located in the Gleeble "pocket jaw" assembly, then shape of the sample after the test and the internal crack formed during the test in the neck portion of this sample

Slika 44: ACT-preizkušanec v žepnih čeljustih Gleeblejeve naprave; oblika preizkušanca po preizkusu in notranja razpoka, nastala v vratu preizkušanca

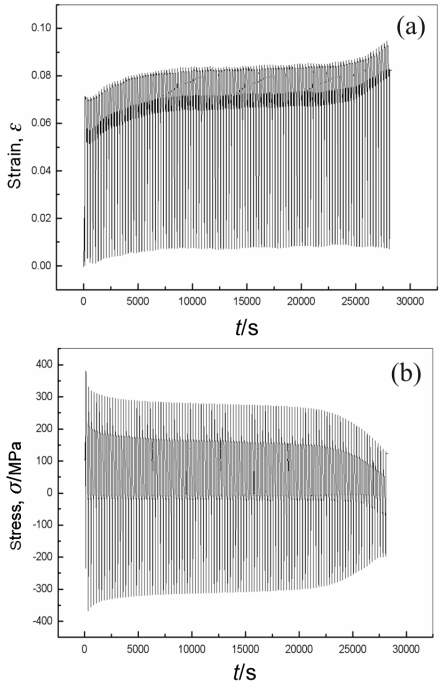

Figure 45: Strain-time (a) and stress-time (b) graphs, from ACT at 600 °C on a post-weld heat-treated P91 weld metal

Slika 45: ACT-grafa deformacija – čas (a) in napetost – čas (b) pri 600 °C za po varjenju toplotno obdelan P 91-zvar

Table 4.1: Hardness results of P91/P92 materials after creep and after ACT

Tabela 4.1: Trdote jekel P91/P92 po preizkusu lezenja in po ACT

Material / sample / exposure	Micro-hardness HV 100G	
	initial	after exposure or testing
P91 component 1 – pipe / 3 years at 568 °C	n. a.	231
P91 component 1 – weld / 3 years at 568 °C	n. a.	258
P91 component 1 – bottle / 3 years at 568 °C	n. a.	243
P91 component 2 – antler / 9 years at 600 °C	n. a.	229
P91 component 2 – weld / 9 years at 600 °C	n. a.	208
P91 component 2 – stub / 9 years at 600 °C	n. a.	177
ACT – P91 standard weld metal with PWHT	285	223
ACT – P91 lean/soft weld metal low PWHT	298	193
ACT – P92 standard weld metal	294	240
ACT – P92 standard pipe	268	228

From the graph of **Figure 45a** for the zero-stress condition the progress of permanent extension can be read, while from graph of **Figure 45b** the decrease of tensile yield strength with progress of the creep can be observed as well as the change of elasticity modulus calculated. Micro-hardness measurements after the ACT show results comparable with these of multi-year creep exposed power generation components of the same grade material; some examples are given in **Table 4.1**.

4.3 Verification of results

The loss of steel's strength during creep is associated with transformation of its microstructure, which in the case of the Cr-Mo-V grade materials is due to precipitation of carbides and their coagulation and also to formation of intermetallic phases, so metallographic and microanalytical investigations are needed to confirm the reliability of the testing procedure.

In the case of the P91 steels and weld metals discussed here, their initial microstructures in the initial tempered state contain numerous fine and medium size carbide precipitates, relatively uniformly distributed in the ferritic matrix retaining its post-martensitic character, **Figure 46**. Such matrix, when seen in thin foil specimens in TEM, mostly consists of fine subgrains aligned in arrays of crystallographic orientations inherited from the former martensite microstructure, **Figure 47**. During exposure to creep conditions, in this initial microstructure further precipitation processes occur as well as

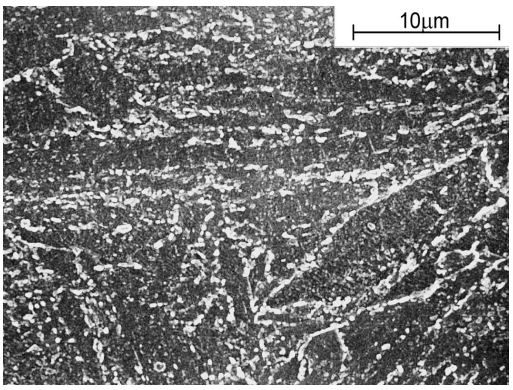

Figure 46: Tempered martensite microstructure of P91 steel; $FeCl_3$ etched, SEM image

Slika 46: Mikrostruktura iz popuščenega martenzita v jeklu P 91. Jedkano s $FeCl_3$; SEM-posnetek

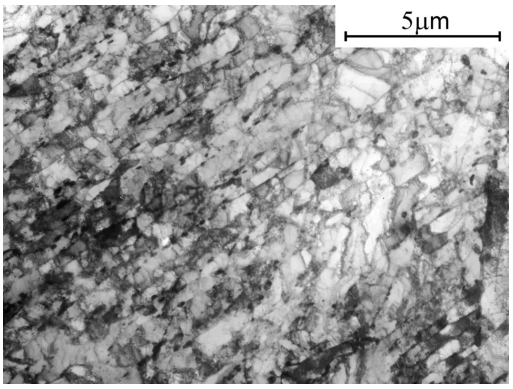

Figure 47: Arrays of subgrains with carbides in tempered martensite of P91 steel; thin foil specimen, TEM image

Slika 47: Področje podzrn s karbidi v popuščenem martenzitu v jeklu P 91, tanka folija; TEM-posnetek

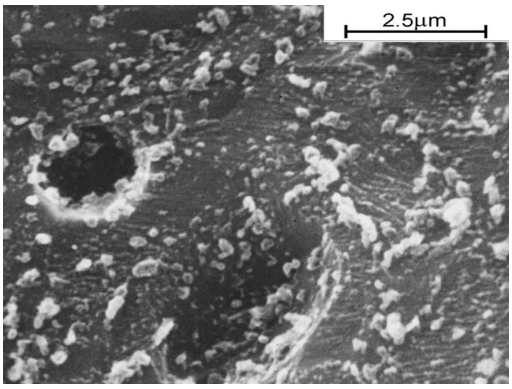

Figure 48: Fracture surface of ACT sample of P91 steel showing high density of carbides, $FeCl_3$ etched, SEM image

Slika 48: Prelomna površina ACT-preizkušanca iz jekla P 91, ki kaže veliko gostoto karbidov; jedkano s $FeCl_3$; SEM-posnetek

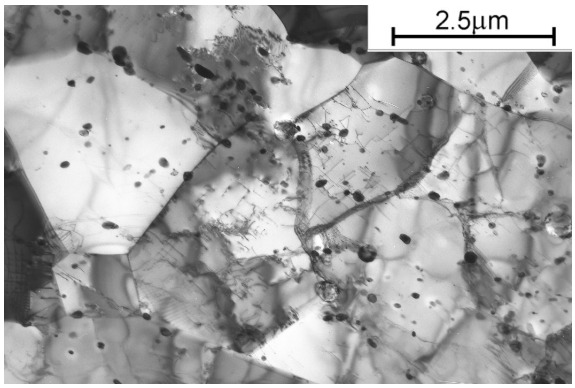

Figure 49: Recrystallised fine ferrite grains retaining oriented arrays of carbides in P91 sample after ACT at 600 °C; TEM, thin foil

Slika 49: Rekristalizirana fina feritna zrna, ki so obdržala orientirano porazdelitev karbidov v preizkušancu iz jekla P91 po ACT pri 600 °C, TEM, tanka folija

transformation of the existing carbides and their coagulation, in combination with recovery and recrystallisation of the matrix.

Accordingly, any reliable creep test should not generate microstructures much different from these taken from true services. The microstructures generated during the ACT appear to be a bit finer than after exposure to true creep while the precipitation of carbides especially at the surface of the internal crack seems to be somewhat more intensive, **Figure 48**. Nevertheless, on the fracture surfaces of the ACT samples the precipitated phases are identical with these after the long-term creep exposure and their content and chemical compositions do agree with the Thermocalc prediction of phases, which should be present at thermodynamic equilibrium [16]. On these fracture surfaces also traces of slip lines can be observed confirming that up to the onset of cracking the process is mainly controlled by dislocations glide and annihilation. Finally the microstructure after the ACT consists of well recrystallised grains with uniform distribution of spheroidal precipitates, mainly carbides, **Figure 49**.

5 CONCLUSIONS

1. Up-to-date physical simulation procedures allow studying materials behaviour at conditions very close to real industrial processing or applications.
2. The process parameters such like temperature, sense and amount of strain, strain rate as well as thermal gradients can be adequately reproduced and their values accurately recorded.
3. By means of physical simulation a large variety of microstructures and associated mechanical properties can be obtained and studied in a short time and for a tiny fraction of full-scale industrial experiments.
4. The materials behaviour data gained from physical simulation experiments can be further used in computer modeling and control of the industrial manufacturing processes.

6 REFERENCES

[1] E. F. Nippes & W. F. Savage; The Weldability of Ship Steel – A Study of the Effect of Travel Speed, Preheat Temperature and Arc Power Level on the Notch Toughness of the Weld Metal and the Heat-Affected Zone, Welding Journal 25 (**1946**), Res Suppl, p. 776s

[2] E. F. Nippes & W. F. Savage; *Tests of Specimens Simulating Weld Heat-Affected Zones*, Welding Journal 28 (**1949**), Res Suppl, p. 599s

[3] W. F. Savage et al; *An Investigation of the Hot Ductility of High Temperature Alloys*, Welding Journal 34 (**1955**), Res Suppl, p.183s

[4] Information on http://www.gleeble.com/

[5] S. T. Mandziej; *Physical Simulation of Welding*, in Proc ASM Intl Conf on Welding & Joining, Madrid, Spain, March 1997, p.253

[6] W. Lin, J. C. Lippold, W. A. Baeslack III; An Evaluation of Heat-Affected Zone Liquation Cracking Susceptibility, Part I: Development of a Method for Quantification', Welding Journal 72 (**1993**), Res Suppl, p.135

[7] C. D. Lundin et al; Hot ductility and hot cracking behavior of Modified 316 Stainless Steels designed for high temperature service, Welding Journal 72 (**1993**), Res Suppl, p.189

[8] *A Standard Procedure for Hot Cracking Test*, Dynamic Systems Inc, Poestenkill, NY, USA, 1995, IIW Doc. II-C-042A/95

[9] CEN ISO/TR 17641-3:2003, Destructive tests on welds in metallic materials – Hot cracking tests for weldments – Arc welding processes – Part 3: Externally loaded tests

[10] H. G. Suzuki, S. Nishimura, S. Yamaguchi; *Physical Simulation of the Continuous Casting of Steels*, in Proc Physical Simulation of Welding, Hot Forming and Continuous Casting, MTL 92-43(TR), CANMET, Canada, 1988, p. II-1

[11] L. Trebacz, R. Kuziak, M. Pietrzyk; *Numerical Model of the SICO Test*, Proc STEELSIM 2005, Brno CR, 2005, p.487

[12] S. T. Mandziej, J. D. Vosburgh, R. Kawalla, H.-G. Schoss; *Physical Simulation of Thin Slab Continuous Casting*, Materials Science Forum, Vols 539-547, 2007, p.4149

[13] B. Engel, M. Albedyhl, M. Brühl, Ch. Klinkenberg, H. Langner, H. Pircher, K. Wünnenberg; Stahl und Eisen 118 (**1998**) 5, 41

[14] H. S. Ferguson; *Fundamentals of Physical Simulation*, in Proc Intl Symposium on Physical Simulation, TU Delft 1992, p. 1

[15] S. T. Mandziej; *Low-Energy Dislocations and Ductility of Ferritic Steels*, in Fundamental Aspects of Dislocation Interactions, Materials Science & Engineering A, 164 (**1993**) 275

[16] S. T. Mandziej, A. Výrostková: Evolution of Cr-Mo-V weld metal microstructure during creep testing – Part 1: P91 material, Welding in the World, 52 (**2008**)1/2, 3

UDK 669.14.018.252:669.13:669.26
Original scientific article/Izvirni znanstveni članek

ISSN 1580-2949
MTAEC9, 44(3)121(2010)

THERMODYNAMIC MODELING FOR THE ALLOY DESIGN OF HIGH SPEED STEELS AND HIGH CHROMIUM CAST IRONS

TERMODINAMIČNO MODELIRANJE NAČRTOVANJA SESTAVE HITROREZNIH JEKEL IN LITINE Z VELIKO VSEBNOSTJO KROMA

Massimo Pellizzari

Department of Materials Engineering and Industrial Technologies, via Mesiano 77, 38050 Trento – Italy
Massimo.Pellizzari@ing.unitn.it

Prejem rokopisa – received: 2009-11-16; sprejem za objavo – accepted for publication: 2003-03-10

In recent years, Thermo-Calc was successfully used by the author for the development of as-cast High Speed Steels and High Chromium Irons. The correlation between solidification process and microstructure was studied in view of influence of alloying elements introduced to promote carbide precipitation. The solidification process occurs under non-equilibrium conditions, because of microsegregation phenomena connected with the solidification structure: the liquid between dendrites becomes progressively enriched in solute and its composition increasingly differs from that predicted by the equilibrium diagram. This behavior can be studied with good approximation by using the model proposed by Scheil and Gulliver. In this way it was possible to refine the phase constitution of High Speed Steels, even if kinetic-related phenomena still limit its correct prediction. Present results also show that microstructural tailoring is possible looking at the correlation existing between the fraction of liquid phase at eutectic MC carbides precipitation. The morphology of V-rich particles changes from a continuous *interdendritic* network to a *globular dissociated eutectic,* showing higher toughness. The composition of HiCrI should result as near as possible to the eutectic, to maximize eutectic carbide amount. Calculations allowed to define the parameter T_L-T_{Ei} (T_L = liquidus temperature; T_{Ei} = eutectic start temperature) as representative of the material hypoeutecticity, and, on the basis of experimental results, a value of 20 °C was safely established in the development of the new composition.

Key words: thermodynamic modelling, solidification, high chromium alloy, high speed steel, phase composition, MC carbides

Zadnja leta je avtor uspešno uporabil Thermo-Calc za razvoj hitroreznih jekel (HSS) in veliko vsebnostjo litine kroma (HiCrI). Raziskana je bila korelacija med procesom strjevanja in mikrostrukturo z vidika legirnih elementov, ki so bili dodani za povečanje precipitacije karbidov. Proces strjevanja je neravnotežen zaradi povezanosti med strjevalno strukturo in mikrosegregacijo: talina med dendriti postopno postane obogatena s topljencem, njena sestava pa se naraščajoče razlikuje od tiste, ki jo napoveduje ravnotežni diagram. Tako vedenje je mogoče raziskati z zadostnim približkom, če uporabimo model, ki sta ga predlagala Scheil in Gulliver. Tako lahko izboljšamo fazno sestavo hitroreznih jekel, čeprav kinetični pojavi omejujejo natančno napoved. Prikazani rezultati dokazujejo, da je mogoče krojiti mikrostrukture z opazovanjem korelacije med deležem taline pri precipitacijo MC-karbidov. Morfologija zrn, bogatih z V, se spremeni od povezane interdritske mreže v globularni disociirani evtektik in dobi večjo žilavost. Sestava litine z veliko vsebnostjo kroma (HiCrI) naj bo čim bližja evtektični, da se tako poveča delež evtektičnih karbidov. Z izračuni je bil določen parameter $T_L - T_{Ei}$ (T_L = likvidis temperatura; T_{Ei} = temperatura začetka evtektika), ki je merilo hipoevtektičnosti. Na podlagi eksperimtalnih rezultatov je bila opredeljena vrednost parametra 20 °C za razvoj novih sestav.

Ključne besede: termodinamično modeliranje, strjevanje, sestava faz, hitrorezno jeklo, litina z veliko vsebnostjo kroma, MC-karbidi

1 INTRODUCTION

The solidification and precipitation sequence play an important role on the microstructure and the final properties of high speed steels (HSS) and high chromium cast irons (HiCrI). The optimization of properties is related to the possibility to govern the phase precipitation, microsegreation and transformation temperature during solidification. This becomes crucial for spincast hot roll materials, that are not submitted to thermomechanical treatment after solidification. Hence, hardness, wear resistance and toughness (…) are largely dependent on the amount and type of primary and eutectic carbides, but also on the composition of the metallic matrix giving rise to secondary hardening during final treatment [1–3].

Different models have been applied to simulate the solidification behaviour of multicomponent systems like high speed steels [4–7] and cast irons [7,8] using thermodynamic methods. In general, the solidification does not follow the equilibrium and limitations regarding the diffusivity in the solid and, partially in the liquid phase, have to be taken into account [9,10]. The Scheil-Gulliver model [11,12], considering the total lack of diffusion within the solid and the complete mixing in the liquid (produced by efficient stirring and diffusion), defines the upper limit for the solute segregation in the liquid and the minimum attainable solidus temperature. In the present work Thermo-Calc [13] software was used to model the solidification process under both, thermodynamic equilibrium and under the conditions stated by the Scheil model.

2 THERMODYNAMIC MODELS AND DATABASE

The phases in the studied multicomponent systems are described by the sub-lattice model [14,15]. The molar Gibbs free energy of a phase *m* in the system can be expressed as

$$G_m = G_m^{\text{ref}} - TS_m^{\text{id}} + G_m^{\text{ex}} + G_m^{\text{mg}}$$

where G_m^{ref} is the reference free energy, $-TS_m^{\text{id}}$ is the ideal mixing entropy, G_m^{ex} is the excess energy term and G_m^{mg} is the change in energy caused by magnetic ordering. The thermodynamic data used for the calculations are contained in the TCFE2000 database. Phases considered are reported in **Table 1**.

3 ALLOY DESIGN OF HIGH CHROMIUM IRON

The nominal chemical composition of standard HiCrI is reported in **Table 2**. The base-alloy contains mainly carbon and chromium, with only minor addition of secondary hardening alloying elements (Mo, V and W).

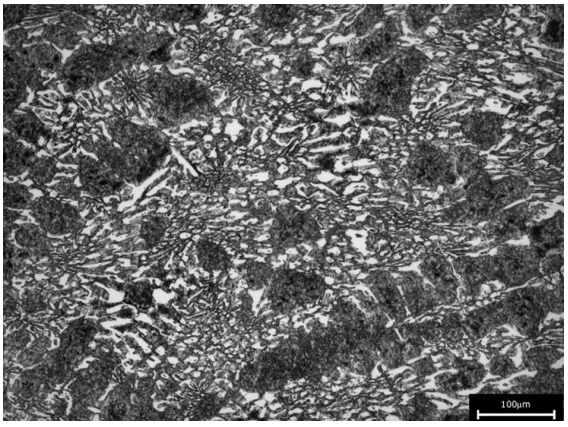

Figure 1: Microstructure of standard HiCrI
Slika 1: a) Mikrostruktura standardne HiCrI

The hypo-eutectic nature of this alloy can be observed in the microstructure in **Figure 1**, displaying the material after quenching from 950 °C and double tempering. The result is also confirmed by the calculated isopleth in

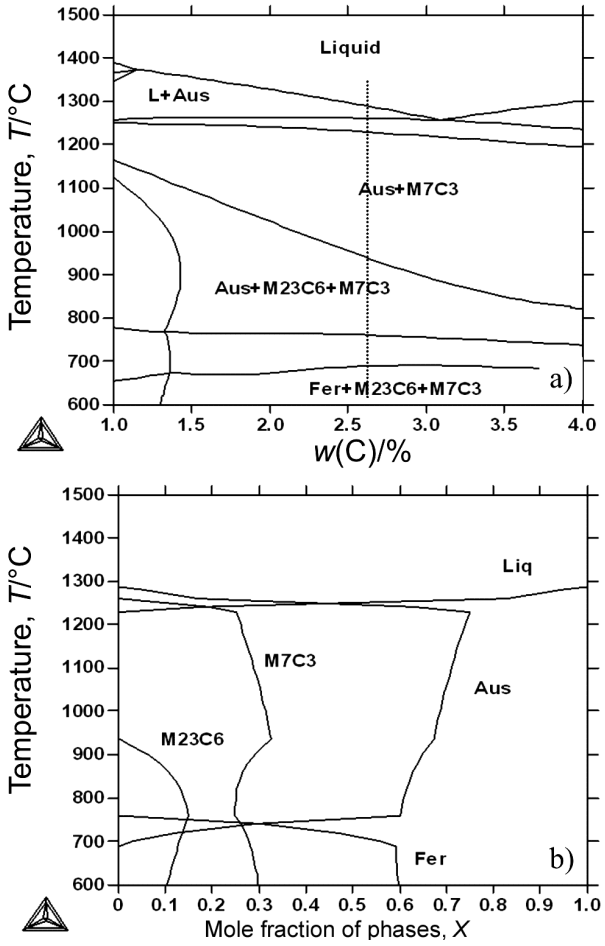

Figure 2: a) Isopleth of standard HiCrI and b) mole fraction of phases vs temperature microstructure
Slika 2: a) Isopleth standardne HiCrI; b) molski delež faz v odvisnosti od tempereture

Table 1: Model of the phases considered in the calculations
Tabela 1: Modeli faz, upoštevanih pri izračunih

Phase	N. sub.	N of sites Per sublatticee	Sublattice Species (Va = vacancies)
Liquid	1	1	Fe ,Si, Mn, Cr, Ni, Mo, V, Nb: C, Va
FCC (austenite)	2	1 : 1	Fe, Si, Mn, Cr, Ni, Mo, V, Nb: C, Va
BCC (ferrite)	2	1 : 3	Fe, Si, Mn, Cr, Ni, Mo, V, Nb: C, Va
MC	2	1 : 1	Fe, Si, Mn, Cr, Ni, Mo, V, Nb: C, Va
M_2C	2	2 : 1	Fe, Si, Mn, Cr, Ni, Mo, V, Nb: C, Va
M_3C (cementite)	2	3 : 1	Fe, Si, Mn, Cr, Ni, Mo, V, Nb: C
M_6C	4	2 : 2 : 2 : 1	Fe : Mo, W: Fe, Si, Mn, Cr, Ni, Mo, V, Nb: C
M_7C_3	2	7 : 3	Fe, Si, Mn, Cr, Ni, Mo, V, Nb: C
$M_{23}C_6$	3	20 : 3 : 6	Fe, Cr: Fe, Cr, Si, Mn, Cr, Ni, Mo, V, Nb: C

Table 2: Chemical composition of standard HiCrI
Tabela 2: Kemična sestav standardne HiCrI

C	Si	Mn	Cr	Ni	Mo	V	W
2.4–2.7	0.3–0.8	0.4–0.8	16–20	0.3–2.0	0.2–2.5	0.2–0.4	0.2–0.6

Figure 2a. Microstructure after heat treatment comprises tempered martensite dendrites and a eutectic consisting of an interpenetrating network of M_7C_3 carbides and tempered martensite.

The volume percentage of eutectic carbides assessed with Image Analysis is 28.0 ± 4 %. This agrees well with that predicted by Thermo-Calc, using TCFE2000 database: the carbide volume percentage, as calculated by the lever rule at 950 °C, is of 32 % (**Figure 2b**). The discrepancy can be explained in view of the lower kinetics of carbides precipitation in the solid state than in the liquid phase. This is confirmed by **Figure 2b** showing that the fraction of M_7C_3 at solidus is much lower (25 %) than at 950 °C.

The solidification of the melt starts with the precipitation of primary austenite at 1287 °C (T_L = liquidus), while, the eutectic reaction starts at 1260 °C (T_{Ei}) and ends at 1228 °C ($T_{Ef} = T_S$ = solidus). Looking to a novel cast iron with higher wear resistance, the composition of the modified HCrI should results as near as possible to the eutectic to maximize eutectic carbide amount. However, in designing the new composition, containing higher percentages of alloying elements than in the standard grade, attention was paid on avoiding hypereutectic solidification which may occur in internal sections of the shell [16], due to segregation. Large pro-eutectic carbides are known to worsen wear resistance and toughness, as well.

Therefore, the new composition was tailored to be slightly hypoeutectic. Since alloying elements influence eutectic carbon, Thermo-Calc was used to simulate solidification of alloys with different compositions, using standard products to validate the theoretical predictions. The content in Cr and Mo was modified. The width of the solidification range of the base alloy by varying content in Cr and Mo is reported in **Figures 3a and 3b**, respectively. While the increasing Cr causes a general reduction of solidification range, Mo plays the opposite effect [17]. **Table 3** resumes the influence of an increasing content of both alloying on the solidification of standard HiCr. The parameter $T_L - T_{Ei}$ (T_L = liquidus temperature; T_{Ei} = eutectic start temperature) was taken as representative of the material hypoeutecticity and, on the basis of the experimental results, a value of 20 °C was safely established in the development of the new composition. Data in **Figure 3** show that the parameter $T_L - T_{Ei}$ is more sensitive to an increase in Cr than in Mo. Thus, in a material with 20 % Cr proeutectic carbides may easily

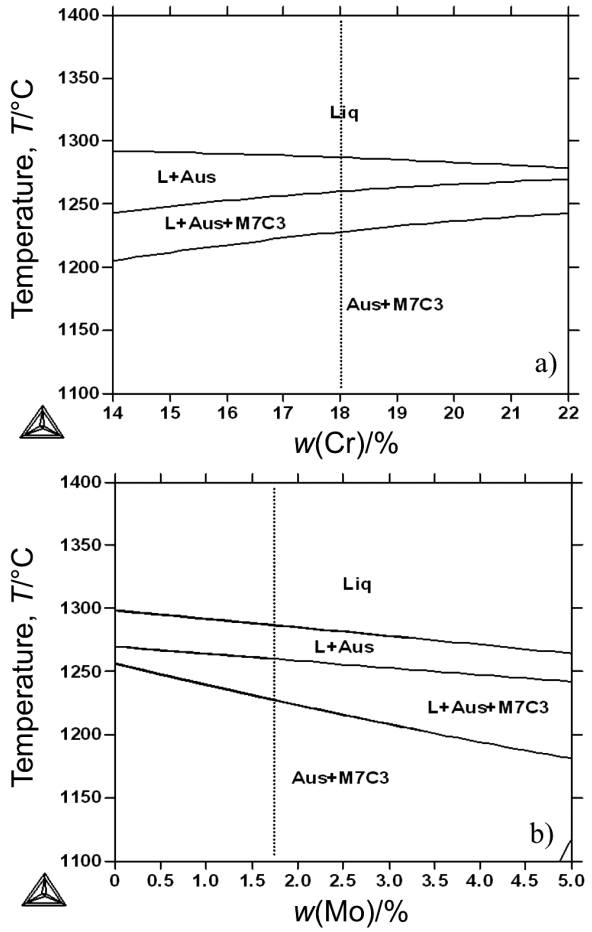

Figure 3: Influence of a) Cr and b) Mo, on the solidification range of standard HiCrI

Slika 3: Vpliv a) Cr in b) Mo na strjevalni interval standardne HiCrI

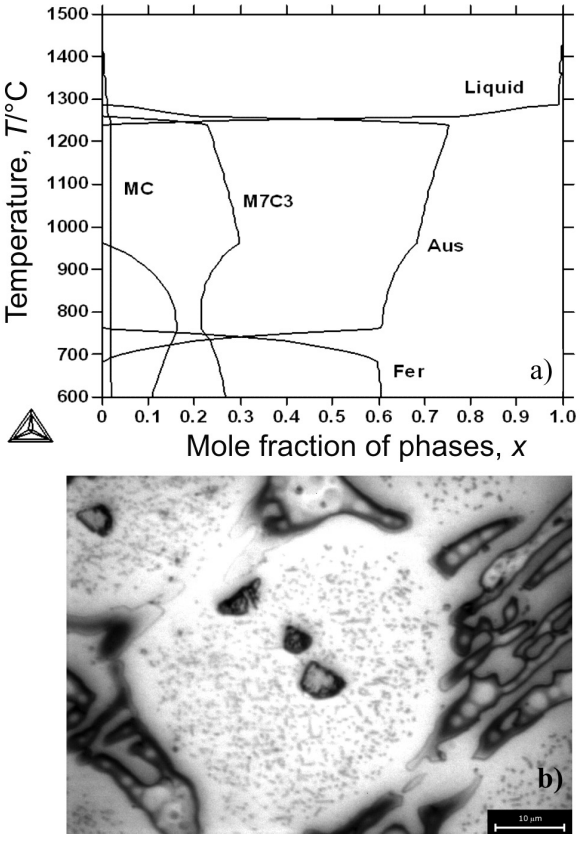

Figure 4: a) Mole fraction of solid phases vs. temperature b) proeutectic (Nb,V)C carbide within the metallic matrix

Slika 4: a) Molski delež faz v odvisnosti od temperature, b) proevtektični (Nb,V)C-karbid v kovinski matici

form at solidification, while no proeutectic carbides could be find up to high Mo content.

Table 3: Influence of Mo and Cr on the solidification range of standard HiCrI
Tabela 3: Vpliv Mo in Cr na strjevalni interval standardne HiCrI

	Standard HiCrI	Standard HiCrI 3% Mo	Standard HiCrI 20% Cr
T_L	1295 °C	↓	↓
T_{Ei}	1260 °C	↓	↑
T_{Ef}	1230 °C	↓	↑
$\Delta T_E = T_{Ei} - T_{Ef}$	30 °C	↑	↓
$\boldsymbol{T_L - T_{Ei}}$	**35 °C**	↑	↓

An improved high Mo HCrI grade was thus designed on the base of the above results to obtain a value of $T_L - T_{Ei}$ greater than 20, after proper modification of the C content of the standard composition. A further development was the introduction of a stronger carbide former than Mo, like V and Nb. Depending on the content of these two elements, pro-eutectic precipitation of MC carbides is possible (**Figure 4a**) directly from the liquid

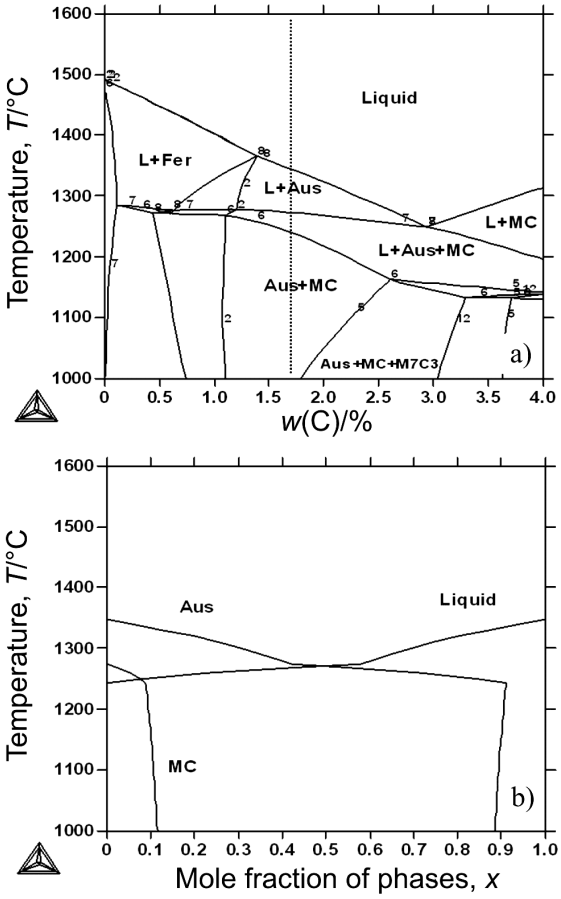

Figure 5: a) Isopleth of the studied HSS (dotted line represent the composition of the studied HSS). b) Diagram reporting the mole fraction of phases vs temperature.
Slika 5: a) Izoplete raziskanega HSS (črtkane črte pomenijo raziskani HSS); b) diagram, ki ponazarja molski delež faz v odvisnosti od temperature

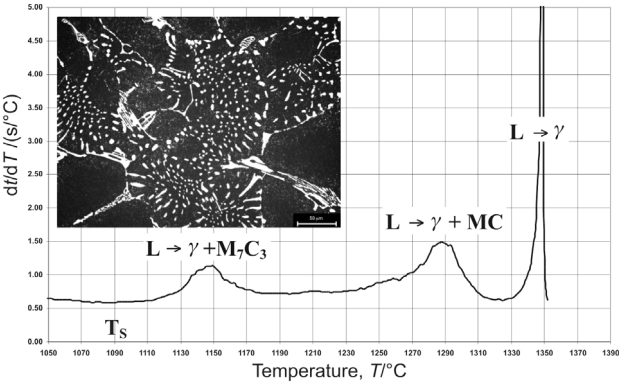

Figure 6: DTA showing the reactions occurring on solidification of HSS. In the frame the microstructure showing the presence of MC and M_7C_3 eutectic carbides
Slika 6: DTA, ki prikazuje reakcije med strjevanjem HSS. V okvirju je mikrostruktura, kjer so prikazani evtektični karbidi MC in M_7C_3

at much higher temperature than eutectic M_7C_3 carbides. Under this conditions, MC carbides are located in the interior of dendrites (**Figure 4b**), causing a substantial strengthening of the metallic matrix, without any embrittlement produced by interdendritic precipitation.

4 ALLOY DESIGN OF HIGH SPEED STEEL

The nominal composition of the base high speed steel in reported in **Table 4**.

Table 4: Nominal composition of the base HSS
Tabela 4: Nominalna sestava osnovnega HSS

C	Si	Mn	Cr	Ni	Mo	V
1.65-1.70	0.8-0.9	0.85-0.90	5.400	0.500	2.900	4.600

The related pseudo binary phase diagram calculated with Thermo-Calc is displayed in **Figure 5a** and the mole fraction of phases provided by equilibrium are shown in **Figure 5b**.

The solidification starts with the formation of primary dendrites of austenite at 1348 °C. The fraction increases up to 0.42 at 1273 °C, as the eutectic reaction, i.e., $L \rightarrow Aus+MC$ carbides starts. The amount of eutectic phases then increases by decreasing the temperature down to the calculated solidus temperature (1243 °C). At this point, the provided molar fraction of MC carbides is 8.8 %. In equilibrium, no other eutectic reactions are predicted.

Thermal analysis highlights that solidification starts at 1355 °C, in good agreement with the calculated value (**Figure 6**). The first eutectic reaction, i. e., $L \rightarrow Aus$ + MC, starts at about 1320 °C and shows the fastest kinetic at about 1280 °C in correspondence of the DTA peak. A second eutectic reaction, i. e., $L \rightarrow Aus$ + M_7C_3, starts at about 1180 °C and shows the maximum rate at 1160 °C. Solidification ends at about 1090 °C, i. e., at a much lower temperature than that provided by equilibrium

Table 5: Computer simulation of the solidification sequence in HSS (Thermo-Calc), using the Scheil Gulliver model
Tabela 5: Računalniška simulacija sekvenc strjevanja HSS (Thermo-Calc) po modelu Scheil Gulliver

Temperatures, T/°C				Volume Pct of Eutectic Carbides, φ/%			
T_L	T_{MC}	T_{M7}	T_S	MC	M_7C_3	M_2C	TOT
1348	1273	1175	1087	8.0	2.0	trace	10.0

Table 6: Computer simulation of the solidification sequence in HSS (Thermo-Calc), using the Scheil Gulliver model
Tabela 6: Računalniška simulacija sekvenc strjevanja HSS (Thermo-Calc) po modelu Scheil-Gulliver

DTA Temperatures, T/°C				Volume Pct of Eutectic Carbides, φ/%			
T_L	T_{MC}	T_{M7}	T_S	MC	M_7C_3	M_2C	TOT
1355	1320	1180	1110	7.0	2.8	trace	10.0

calculations (1243 °C). Discrepancies between calculations and DTA can be explained in view of the microsegregation to which liquid is exposed during solidification, caused mainly by the limited diffusion of solute atoms in solid phase. The result of simulation using the Scheil-Gulliver model in Thermo-Calc better reflects the experimental one. In **Figure 7**, the comparison between calculated molar fractions and experimental data indicate a quite good agreement. Now, beneath the eutectic reaction allowing the precipitation of MC carbides, a second reaction involving the precipitation of M_7C_3 is provided, as well. The fractions of carbides assessed with image analysis and calculations are very close, such us the solidus temperatures. As expected, in view of the maximum possible segregation of the liquid provided by the Scheil model, the calculated solidus underestimates the experimental value.

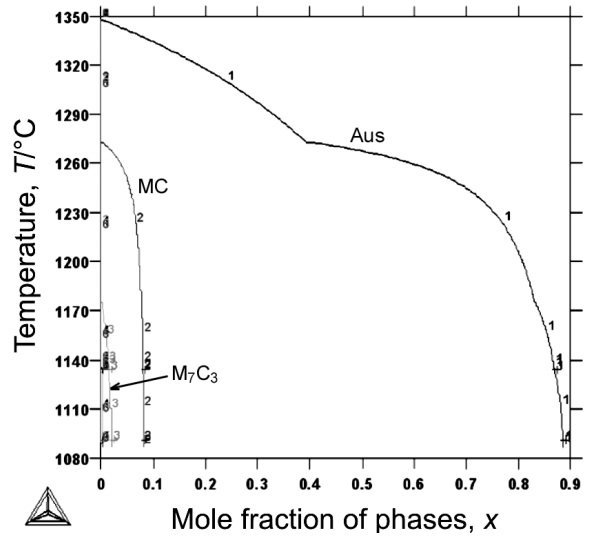

Figure 7: Molar fraction of solid phases provided by Thermo-Calc simulation using the Scheil Gulliver model
Slika 7: Molski delež faz, določen na podlagi Thermo-Calc simulacije po Scheil Gulliver modelu

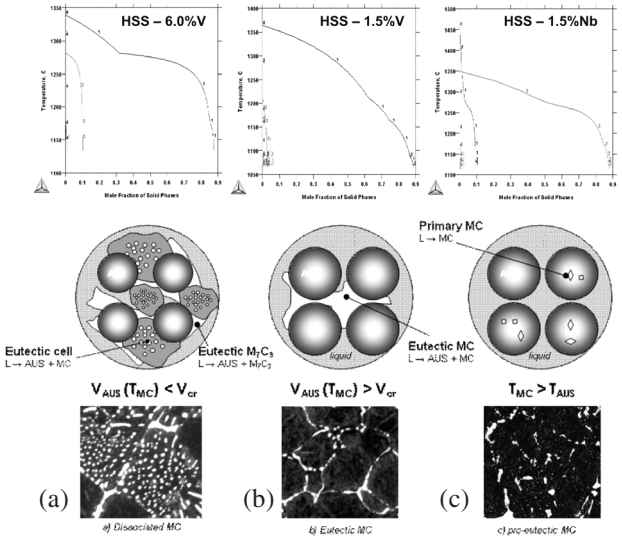

Figure 8: Morphology of MC carbides as a function of the content in V and Nb
Slika 8: Morfologija karbidov MC kot funkcija vsebnosti V in Nb

Hence, it can be stated that solidification proceeds under non equilibrium conditions, is caused principally by the limited diffusion in the solid phase.

This allows the author to use the Scheil-Gulliver model in the alloy design of such steel grade. Interdendritic eutectic carbides reduce toughness of HSS, since they constitute an almost continuous brittle network in

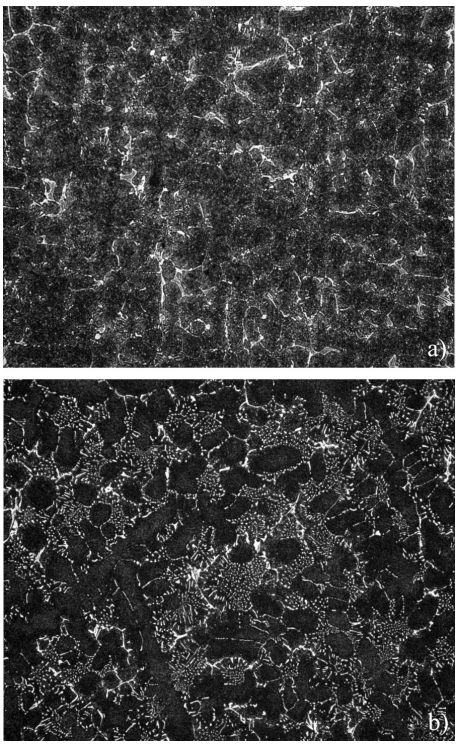

Figure 9: Increasing fraction of dissociated eutectic carbides by increasing V/Cr content (from up to down)
Slika 9: Naraščajoči delež disociacije evtektičnih karbidov pri rasti razmerja vsebnosti V/Cr (z zgoraj na dol)

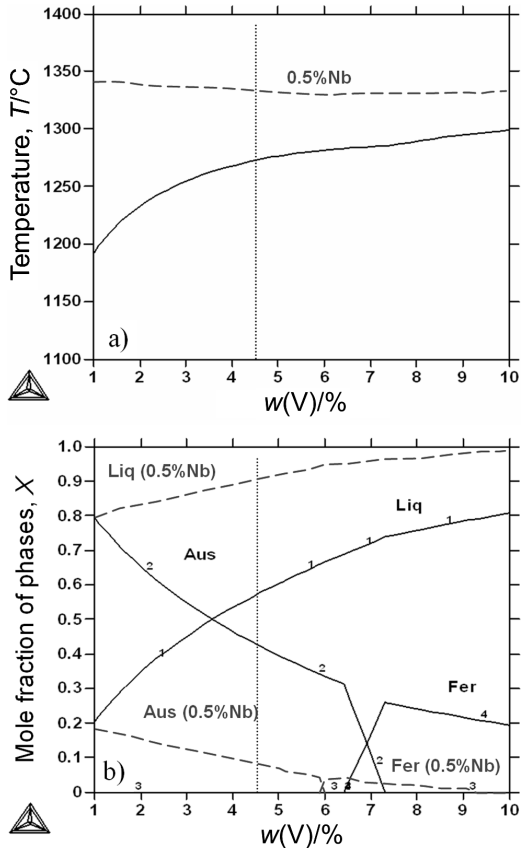

Figure 10: a) Eutectic MC start temperature and b) Mole fraction of phases as a function of V content at eutectic MC start

Slika 10: a) začetna temperatura MC-evtektika in b) molski delež faz v odvinsosti od vsebnosti V pri začetku MC-evtektika

the microstructure. Moreover, crack usually nucleates either at the carbide-matrix interface or inside the carbide particle, because the different elastic properties of the two constituents rise local stresses. Depending on the chemical composition, MC carbides tend to precipitate with different morphology.

By high C and V concentration VC homogeneously precipitates in eutectic cells to form a *dissociated eutectic* (**Figure 8a**). A relative high amount of fine and globular particles precipitate together with eutectic austenite, so that they are expected to be less detrimental for toughness than interdendritic carbides. The criteria to obtain this kind of microstructure is that the eutectic reaction is started with a high fraction of residual liquid phase. This allows eutectic cells to develop fully. **Figure 8a** shows the fraction of solid phases in the base HSS added with 6 % V. Two effects have to be underlined. The MC start temperature is increased with respect to the base material (1281 °C vs 1273 °C) and the corresponding fraction of liquid phase is higher (0.69 vs 0.58), as well. Indeed, **Figure 8b** shows the opposite result for the steel with V content decreased to 1.5 %. The MC start temperature drops to 1210 °C and the corresponding fraction of liquid phase to 0.38. Experimental results (**Figure 9**) confirm that the increasing content in V facilitates the formation of a microstructure with a high fraction of dissociated eutectic.

It is interesting to point out that Thermo-Calc allows the easy calculation of the MC start temperature (**Figure 10a**) and of the fraction of liquid phase (**Figure 10b**) by varying the content in V. Continuous lines in **Figure 10b** highlight the increasing fraction of liquid phase at MC precipitation start as the content in V increases. Correspondingly, the fraction of solid, i.e. austenite up to 7.2 % V and ferrite above 6.5 %, decreases.

With the aid of data in **Figure 10** a critical value for the fraction of austenite, for the formation of dissociated MC carbides could be determined. Increasing the V content above this value, the amount of eutectic cells progressively increases. A limiting factor is represented by the segregation of VC carbides during centrifugal casting of bimetallic rolls. Because of the lower density of these particles the liquid phase, MC carbides tend to segregate at the shell-core interface. This phenomenon is responsible for poor bonding and must be controlled to preserve roll quality. Hence, as proposed previously, Nb can be added, allowing the formation of composite Nb-V MC carbides with higher density. Nb is an MC former stronger than V. The addition of a small amount of this element dramatically increases the precipitation temperature of MC carbides (**Figure 10**). In **Figure 10a and 10b** dashed lines are referred to the standard alloy with 0.5 % Nb. As MC precipitate in the 1 % V – 0.5 % Nb alloyed high speed steel the fraction of liquid is about 0.8, i.e. much higher than that observed in the base material (0.2). As the content in V is close to the mass fraction 10 %, the fraction of liquid at MC precipitation start becomes almost 1, indicating the ultimate condition before the occurrence of proeutectic precipitation of MC carbides. This circumstance is verified by the higher amount of Nb, as confirmed by **Figure 8c**, showing the fraction of solid phases in the base HSS with addition of 1.5 % Nb. NbC particles now precipitate directly from the liquid at a much higher temperature than Nb-free or low-Nb grades promoting the heterogeneous nucleation of austenite dendrites. From this point of view, a refinement of the solidification structure can be obtained with properly selecting/handling Niobium. A basic form of inoculation can be realized.

Finally, in order to drive solidification transformations towards dissociate eutectic and to minimize the amount of interdendritic carbides, the chemical composition must be designed with a prevailing amount of V and a limited amount of Cr, Mo and W. As an example, if the amount in Cr is increased keeping V constant, the temperature of Cr-rich M_7C_3 eutectic carbides is increased, as their total fraction with respect to VC. The possibility of eutectic cells development is hindered by the concurrent precipitation of solid Aus + M_7C_3 (**Figure 9**). Moreover, carbon content has to be designed to both sustain the precipitation of carbides and harden tempered martensite.

5 CONCLUSIONS

The present paper briefly resumes the authors knowledge in the field of alloy design of high Speed Steels and High Chromium Irons by means of thermodynamic modelling. The basic criteria for the development of new alloys were illustrated in view of the eutectic reactions occurring during solidification. The influence of type and amount of different alloying elements on the solidification sequence was analysed and correlated to the microstructure. The results confirm the possibility to successfully employ computer modelling in the alloy design of high alloyed steels and cast irons.

6 REFERENCES

[1] Molinari A., Tremea A., Pellizzari M., Biggi A., Corbo G.: Mater. Sci. and Technol. 18 (**2002**), 1574–1580

[2] K. C. Hwang, S. Lee, H. C. Lee: Mater. Sci. Eng. A 254 (**1998**), 282

[3] S. Karagöz, H. F. Fischmeister: Met. Trans. A 29 (**1998**), 205–216

[4] J. A. Golczewsky, H. F. Fischmeister: Z. Metallkd. 84 (**1993**) 12, 860–866

[5] J. A. Golczewsky, H. F. Fischmeister: Steel Research. 63 (**1992**) 8, 354–360

[6] P. Gustafson: Computer assisted development of High Speed Steels. In The SGTE Casebook, Thermodynamic at work. Chapter 6. 70–76

[7] G. Coelho, J. A. Golczewsky, H. F. Fischmeister: Met. Trans. A 34 (**2003**), 1749–1758

[8] C. G. Schon, A. Sinatora, CALPHAD 22 (**1998**), 437

[9] H. F. Fischmeister, R. Riedl, S. Karagöz: Met. Trans. A 20 (**1989**), 2133

[10] M. Boccalini, H. Goldenstein: Intl. Mater. Reviews, 46 (**2001**) 2, 92–114

[11] G. M. Gulliver: J. Inst. Metals 9 (**1913**), 120–157

[12] E. Scheil: Z. Metallkd. 34 (**1942**), 70–72

[13] B. Sundman et al., CALPHAD 9 (**1985**), 153

[14] H. Ohtani, T. Tnaka, M. Hasebe, T. Nishizawa: Calphad 12 (**1988**), 225

[15] M. Hillert, LI Staffansson: Acta Chem. Scand. 24 (**1970**), 3618

[16] Molinari A., Pellizzari M., Biggi A., Corbo G., Tremea A.: Development of spincast hot rolls through microstructural tailoring. Proc. 44th Mechanical Working and Steel Processing, Orlando (Florida), 8-11 september, 2002, Iron & Steel Society:Vol. XL, pp. 1233–1244

[17] J. A. Tenorio et.al., Int. J. Cast Metals Res. 13 (**2000**), 99

UDK 669.715:620.178
Original scientific article/Izvirni znanstveni članek

ISSN 1580-2949
MTAEC9, 44(3)129(2010)

USE OF GREY BASED TAGUCHI METHOD IN BALL BURNISHING PROCESS FOR THE OPTIMIZATION OF SURFACE ROUGHNESS AND MICROHARDNESS OF AA 7075 ALUMINUM ALLOY

UPORABA GREY-TAGUCHIJEVE METODE PRI PROCESU GLAJENJA ZA OPTIMIZACIJO POVRŠINSKE HRAPAVOSTI IN MIKROTRDOTE ALUMINIJEVE ZLITINE AA 7075

Ugur Esme

Mersin University Tarsus Technical Education Faculty, Department of Mechanical Education, 33140, Tarsus-Mersin/Turkey
uguresme@gmail.com

Prejem rokopisa – received: 2009-11-09; sprejem za objavo – accepted for publication: 2010-03-20

This study investigated the multi-response optimization of burnishing process for an optimal parametric combination to yield favorable surface roughness and microhardness using the Grey relational analysis and Taguchi method. Sixteen experimental runs based on an orthogonal array of Taguchi method were performed to derive objective functions to be optimized within experimental domain. The objective functions have been selected in relation of burnishing parameters; burnishing force, number of passes, feed rate and burnishing speed. The Taguchi approach followed by Grey relational analysis was applyed to solve the multi-response optimization problem. The significance of the factors on overall quality characteristics of the burnishing process has also been evaluated quantitatively with the variance method (ANOVA). Optimal results were verified through confirmation experiments. This shows application feasibility of the Grey relation analysis in combination with Taguchi technique for continuous improvement in product quality in manufacturing industry.

Keywords: ball burnishing process, Grey relation analysis, Taguchi method

V tej študiji je raziskana večodgovorna optimizacija procesa glajenja z dosego optimalnih kombinacij parametrov za ugodno površinsko hrapavost in mikrotrdoto z uporabo Greyjeve analize odvisnosti in Taguchijeve metode. Šestnajst eksperimentov v ortogonalni porazdelitvi po metodi Taguchi je bilo uporabljenih za razvoj objektivnih funkcij za optimizacijo v eksperimentalnem polju. Objektivne funkcije so bile izbrane v odvisnosti od parametrov glajenja; sila glajenja, število prehodov, hitrost podajanja in hitrost glajenja. Taguchijev približek in Greyjeva analiza odvisnosti sta bila uporabljena za rešitev večodgovornega problema. Kvantitativno je bil ocenjen tudi pomen dejavnikov kakovosti procesa glajenja z metodo variance (ANOVA). Optimalni rezultati so bili potrjeni s preizkusi. Delo dokazuje uporabnost Greyjeve analize odvisnosti in Taguchijeve tehnike za stalno izboljšanje kakovosti proizvodov v predelovalni industriji.

Ključne besede: krogelno glajenje, Greyjeva analiza odvisnosti, Taguchijeva metoda

1 INTRODUCTION

The function performance of a machined component such as fatigue strength, load bearing capacity, friction, etc. depends to a large extent on the surface as topography, hardness, nature of stress and strain induced on the surface region. Nowadays, about 50% of the energy supplied is lost in the friction of elements in relative motion[1,2]. Roughness values less than 0.1 mm are required for good aesthetic appearance, easy mould release, good corrosion resistance, and high fatigue strength. During recent years, however, considerable attention has been paid to the post-machining metal finishing operations such as burnishing which improves the surface characteristics by plastic deformation of the surface layers[2,3].

Burnishing is considered as a cold-working finishing process, differing from other cold-working, surface treatment processes such as shot peening and sand blasting, etc. in that it produces a good surface finish and also induces residual compressive stresses at the metallic surface layers[4]. Accordingly, burnishing distinguishes itself from chip-forming finishing processes such as grinding, honing, lapping and super-finishing which induce residual tensile stresses at the machined surface layers[5,6]. Also, burnishing is economically desirable, because it is a simple and cheap process, requiring less time and skill to obtain a high-quality surface finish[4,5].

Beside producing a good surface finish, the burnishing process has additional advantages over other machining processes, such as securing increased hardness, corrosion resistance and fatigue life as a result of producing compressive residual stress. Residual stresses are probably the most important aspect in assessing integrity because of their direct influence on performance in service. Thus, control of the burnishing process (burnishing conditions) in such a way as to produce compressive residual stresses in the surface region could lead to considerable improvement in component life. A comprehensive classification of burnishing tools and their application has been given by Shneider[7]. A literature survey shows that work on the burnishing process

has been conducted by many researchers and the process improves also the properties of the parts, e.g. higher wear resistance[2,8,9] increased hardness[10-12], surface quality[2,3,14] and increased maximum residual stress in compression[11]. The parameters affecting the surface finish are: burnishing force, feed rate, ball material, number of passes, workpiece material, and lubrication[2,3]. It is necessary to find an optimal process condition capable of producing desired surface quality and hardness. However, this optimization should be performed in such a way that all the objectives should fulfill simultaneously. Such an optimization technique is called multi-response optimization[15].

The majority of the research existing in literature on the effect of burnishing parameters on the burnished surface is of experimental nature and very few analytical models are available in the literature.

The Taguchi method is very popular for solving optimization problems in the field of production engineering.[16,17] The method utilizes a well-balanced experimental design (allows a limited number of experimental runs) called orthogonal array design, and signal-to-noise ratio (S/N ratio), which serve as objective function to be optimized (maximized) within the experimental domain. However, traditional Taguchi method cannot solve multi-objective optimization problem. To overcome this, the Taguchi method coupled with Grey relational analysis has a wide area of application in manufacturing processes. This approach can solve multi-response optimization problem simultaneously[15,18].

Planning the experiments through the Taguchi orthogonal array has been used quite successfully in process optimization[19–24]. Therefore, in this study the Taguchi $L_{16}(4^4)$ orthogonal array was applied to plan the experiments on burnishing process.

Four controlling factors including burnishing force (F), number of passes (N), feed rate (f) and burnishing speed (V) on the surface roughness (Ra) and microhardness (HV) with four levels for each factor were selected. The Grey relational analysis was then applied to examine how the burnishing parameters influenced the surface roughness and microhardness and an optimal parameter combination was then obtained. Through analyzing the Grey relational grade matrix, the most influential factors for individual quality targets of burnishing process can be identified. Additionally, the analysis of variance (ANOVA) was also utilized to examine the most significant factors for the surface roughness and microhardness in burnishing process.

2 GREY RELATIONAL ANALYSIS

In Grey relational analysis, experimental data i.e., measured features of quality characteristics are first normalized ranging from zero to one. This process is known as Grey relational generation. Next, based on normalized experimental data, Grey relational coefficient is calculated to represent the correlation between the desired and actual experimental data[15]. Then overall Grey relational grade is determined by averaging the Grey relational coefficient corresponding to selected responses. The overall performance characteristic of the multiple response process depends on the calculated Grey relational grade. This approach converts a multiple response process optimization problem into a single response optimization situation with the objective function which is the overall Grey relational grade. The optimal parametric combination is then evaluated which would result in the highest Grey relational grade. The optimal factor setting for maximizing overall Grey relational grade can be obtained by Taguchi method[15].

In Grey relational generation, the normalized Ra values corresponding to the smaller-the-better (SB) criterion which can be expressed as:

$$x_i(k) = \frac{\max y_i(k) - y_i(k)}{\max y_i(k) - \min y_i(k)} \tag{1}$$

HV_{100} should follow the larger-the-better (LB) criterion, which can be expressed as:

$$x_i(k) = \frac{y_i(k) - \min y_i(k)}{\max y_i(k) - \min y_i(k)} \tag{2}$$

where $x_i(k)$ is the value after the Grey relational generation, min $y_i(k)$ is the smallest value of $y_i(k)$ for the k^{th} response, and max $y_i(k)$ is the largest value of $y_i(k)$ for the k^{th} response[15]. An ideal sequence is [$x_0(k)$ (k=1, 2, 3....., 16)] for the responses. The definition of Grey relational grade in the course of Grey relational analysis is to reveal the degree of relation between the 16 sequences [$x_0(k)$ and $x_i(k)$, i=1, 2, 3,.....,16]. The Grey relational coefficient $\xi_i(k)$ can be calculated as:

$$\xi_i(k) = \frac{\Delta_{\min} - \psi\Delta_{\max}}{\Delta_{0i}(k) + \psi\Delta_{\max}} \tag{3}$$

where $\Delta_{0i} = \left\| x_0(k) - x_i(k) \right\|$ the absolute value of the difference of $x_0(k)$ and $x_i(k)$; ψ is the distinguishing coefficient $0 \le \psi \le 1$; $\Delta_{\min} = \forall j^{\min} \in i \forall k^{\min} \left\| x_0(k) - x_j(k) \right\|$ = the smallest value of Δ_{0i}; and $\Delta_{\max} = \forall j^{\max} \in i \forall k^{\max} \left\| x_0(k) - x_j(k) \right\|$ is the largest value of Δ_{0i}. After averaging the Grey relational coefficients, the Grey relational grade γ_i can be computed as:

$$\gamma_i = \frac{1}{n} \sum_{k=1}^{n} \xi_i(k) \tag{4}$$

where n is the number of process responses. The higher value of Grey relational grade corresponds to intense relational degree between the reference sequence $x_0(k)$ and the given sequence $x_i(k)$. The reference sequence $x_0(k)$ represents the best process sequence. Therefore, higher Grey relational grade means that the corresponding parameter combination is closer to the optimal[15]. The mean response for the Grey relational grade with its

grand mean and the main effect plot of Grey relational grade are very important because optimal process condition can be evaluated from this plot[15].

3 EXPERIMENTAL DETAILS AND TEST RESULTS

3.1 Workpiece Material

In this study, high strength precipitation hardening 7XXX series wrought aluminum alloy AA 7075 was used. The strength and good mechanical properties make the AA 7075 aluminum alloy appropriate for the use in aerospace industry. The chemical composition and mechanical properties of the workpiece material is given in **Table 1**.

Table 1: Chemical composition and mechanical properties of AA7075 aluminum alloy
Tabela 1: Kemična sestava in mehanske lastnosti aluminijeve zlitine AA 7075

Chemical composition (%)	Al	Cu	Mg	Cr	Zn
	90.0	1.60	2.50	0.23	5.60
Mechanical properties	Tensile strength (MPa)	Yield strength (MPa)	Shear strength (MPa)	Fatique strength (MPa)	Hardness (HV_{100})
	220	95	150	160	150

The workpiece material, as shown in **Figure 1**, was prepared with the diameter of 30 mm and 70 mm in length as a three part each having 20 mm length.

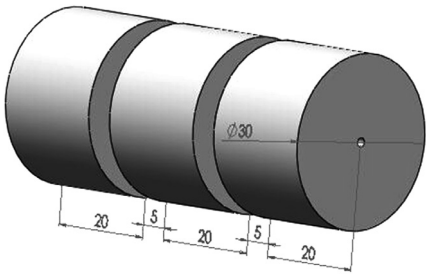

Figure 1: Dimensions of workpiece material[25]
Slika 1: Mere preizkušanca

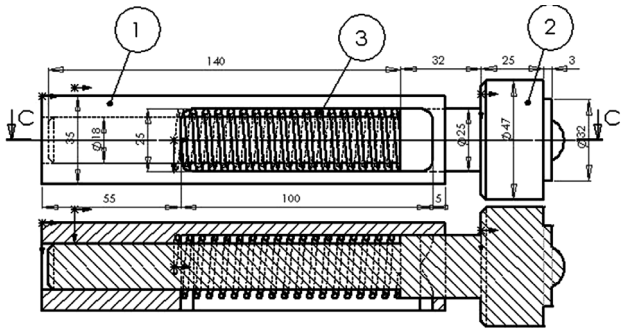

Figure 2: Detailed drawing of the ball burnishing tool: (1) casing; (2) adapter cover; (3) spring[25]
Slika 2: Načrt gladilnega orodja: (1) ohišje; (2) prilagoditveni pokrov, (3) vzmet[25]

3.2 Machines and Equipments

An 18 mm diameter ball was used for burnishing. The detailed and drawing is shown in **Figure 2**. When the ball or roller is pressed against the surface of the metallic specimen, a pre-calibrated spring was compressed. This spring is being used mainly to reduce the possible sticking of the tool onto the surface[25].

The experiments were performed on a *FANUC GT-250B CNC* lathe. The burnishing tool was mounted on the CNC turret. Dry turning and burnishing were used in all the experimental work, but alcohol was used to clean the specimens before burnishing. Cleaning of the ball was carried out continuously in order to prevent hard particles from entering on the contact surface between the tool and the specimen, such hard particles usually leaving deep scratches, which may damage the burnished surface of the specimen[25].

Phynix TR-100 model surface roughness tester was used to measure the surface roughness of the burnished samples. Cut off length was chosen as 0.3 for each roughness measurement. Vickers microhardness tester with 100 g load (HV_{100}) was used for microhardness measurements[25]. Six measurements of surface roughness and microhardness were taken from the samples and average of the values were used in the multi-criteria optimization.

3.3 Process Parameters and Test Results

In full factorial design, the number of experimental runs exponentially increases as the number of factors as well as their level increases. This requires huge experimentation cost and considerable time. So, in order to compromise these two adverse factors and to search the optimal process condition through a limited number of experimental runs Taguchi's $L_{16}(4^4)$ orthogonal array consisting of 16 sets of data was selected to optimize the multiple performance characteristics of surface roughness. The burnishing parameters used in this study are shown in **Table 2**.

Table 2: Process parameters and their limits
Tabela 2: Parametri in omejitve procesa

Parameters	Notation	Unit	Levels of factors			
			1	*2*	*3*	*4*
Burnishing force	F	N	58.86*	117.72	176.58	235.44
Number of passes	N	–	1*	2	3	4
Feed rate	f	mm/min	0.1*	0.2	0.3	0.4
Burnishing speed	V	rpm	200*	300	500	700

*Initial factor settings

Table 3 shows the selected design matrix based on Taguchi $L_{16}(4^4)$ orthogonal array consisting of 16 sets of coded conditions and the experimental results for the

responses of Ra and HV_{100}. All these data were utilized for the analysis and evaluation of optimal parameter combination required to achieve desired surface quality within the experimental domain.

Table 3: Orthogonal array $L_{16}(4^4)$ of the experimental runs and results
Tabela 3: Ortogonalna porazdelitev $L_{16}(4^4)$ preizkusov in rezultati

Run no	Process parameters				Experimental results	
	F	N	f	V	Ra (μm)	HV_{100}
1	1	1	1	1	0.61	160
2	1	2	2	2	0.57	167
3	1	3	3	3	0.53	173
4	1	4	4	4	0.59	187
5	2	1	2	3	0.36	165
6	2	2	1	4	0.18	178
7	2	3	4	1	0.25	181
8	2	4	3	2	0.20	193
9	3	1	3	4	0.20	172
10	3	2	4	3	0.22	187
11	3	3	1	2	0.08	196
12	3	4	2	1	0.23	210
13	4	1	4	2	0.30	191
14	4	2	3	1	0.15	199
15	4	3	2	4	0.14	205
16	4	4	1	3	0.19	212

4 PARAMETRIC OPTIMIZATION OF BURNISHING PROCESS

4.1 Evaluation of Optimal Process Condition

First, by using Eqs. (1) and (2), experimental data were normalized to obtain Grey relational generation[15]. The normalized data and Δ_{0i} for each of the responses are given in **Table 4** and **Table 5** respectively. For Ra smaller-the-better (SB) and for HV larger-the-better (LB) criterion has been selected.

Table 4: Grey relational generation of each performance characteristics
Tabela 4: Generacija Greyjeve odvisnosti za karakteristike vsake performance

Run no	Ra	HV
	Smaller-the-better	***Larger-the-better***
Ideal sequence	1	1
1	0.000	0.000
2	0.043	0.075
3	0.250	0.151
4	0.519	0.038
5	0.096	0.472
6	0.346	0.811
7	0.404	0.679
8	0.635	0.774
9	0.231	0.774
10	0.519	0.736
11	0.692	1.000
12	0.365	0.717
13	0.596	0.585
14	0.750	0.868
15	0.865	0.887
16	1.000	0.792

Table 5: Evaluation of Δ_{0i} for each of the responses
Tabela 5: Ocena Δ_{0i} za vsak odgovor

Run no	Ra	HV
Ideal sequence	1	1
1	1.000	1.000
2	0.957	0.925
3	0.750	0.849
4	0.481	0.962
5	0.904	0.528
6	0.654	0.189
7	0.596	0.321
8	0.365	0.226
9	0.769	0.226
10	0.481	0.264
11	0.308	0.000
12	0.635	0.283
13	0.404	0.415
14	0.250	0.132
15	0.135	0.113
16	0.000	0.208

Table 6 shows the calculated Grey relational coefficients (with $\psi_{Ra} = 0.67$, $\psi_{HV} = 0.33$) of each performance characteristic using Eq. (3).

Table 6: Grey relational coefficient of each performance characteristics ($\psi_{Ra} = 0.67$, $\psi_{HV} = 0.33$)
Tabela 6: Greyjev odvisnostni koeficient za karakteristike vsake performance ($\psi_{Ra} = 0.67$, $\psi_{HV} = 0.33$)

Run no	Ra	HV
Ideal sequence	1	1
1	0.333	0.333
2	0.343	0.351
3	0.400	0.371
4	0.510	0.342
5	0.356	0.486
6	0.433	0.726
7	0.456	0.609
8	0.578	0.688
9	0.394	0.688
10	0.510	0.654
11	0.619	1.000
12	0.441	0.639
13	0.553	0.546
14	0.667	0.791
15	0.788	0.815
16	1.000	0.707

The Grey relational coefficients, given in **Table 7**, for each response was accumulated by using Eq. (4) to evaluate Grey relational grade, which is the overall representative of all the features of burnishing quality. Thus, the multi-criteria optimization problem was transformed into a single equivalent objective function optimization problem using the combination of Taguchi

approach and Grey relational analyses. Higher is the value of Grey relational grade, the corresponding factor combination is said to be close to the optimal.

Table 7: Grey relational grade
Tabela 7: Greyjeva stopnja odvisnosti

Run no	Grey relational grade	Rank
1	0.333	16
2	0.348	15
3	0.380	14
4	0.397	13
5	0.443	12
6	0.629	6
7	0.558	10
8	0.651	5
9	0.591	8
10	0.606	7
11	0.874	1
12	0.573	9
13	0.548	11
14	0.750	4
15	0.806	2
16	0.803	3

When the Taguchi experimental design is carried out, a function would be offered (efficiency evaluation) about one design factor as the standard to evaluate the efficiency and to understand the experiment efficiency. While Taguchi experimental design took the quality loss as the base, it would design one statistic to evaluate efficiency, which is called the S/N ratio. In this section we had one quality characteristic that is grey relational grade for Taguchi analysis[26]. **Table 8** shows the S/N ratio based on the larger-the-better criterion for overall Grey relational grade calculated by using Eq. (5).

$$S/N = -10 \lg\left[\frac{1}{n}\sum_{i=1}^{n}\frac{1}{y_i^2}\right] \quad (5)$$

where n is the number of measurements, and y_i is the measured characteristic value.

Table 8: S/N ratio for overall Grey relational grade
Tabela 8: Razmerje S/N za splošno Greyjevo odvisnostno stopnjo

Run no	S/N
1	-9.54
2	-9.16
3	-8.40
4	-8.02
5	-7.07
6	-4.02
7	-5.06
8	-3.72
9	-4.57
10	-4.34
11	-1.17
12	-4.83
13	-5.21
14	-2.50
15	-1.87
16	-1.90

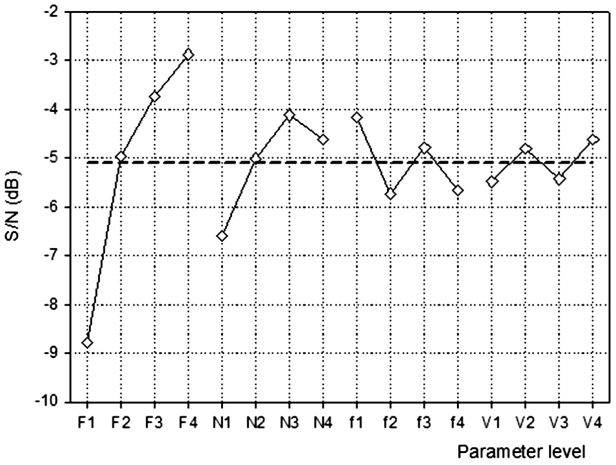

Figure 3: S/N ratio plot for the overall Grey relational grade
Slika 3: S/N razmerje za splošno Greyjevo stopnjo

Graphical representation of S/N ratio for overall Grey relational grade is shown in **Figure 3**. The dashed line is the value of the total mean of the S/N ratio.

As indicated in **Figure 3**, the optimal condition for the burnishing of AA7075 aluminum alloy becomes $F_4N_3f_1V_4$. **Table 9** shows the mean Grey relational grade ratio for each level of the process parameters.

Table 9: Response table for the mean Grey relational grade
Tabela 9: Tabela odgovorov za povprečno Greyjevo odvisnostno stopnjo

Factors	Grey relational grade				
	Level 1	Level 2	Level 3	Level 4	Max-Min
F	0.36	0.57	0.66	0.73	0.37
N	0.48	0.58	0.65	0.61	0.17
f	0.66	0.54	0.59	0.53	0.13
V	0.55	0.61	0.56	0.61	0.06

Total mean Grey relational grade= 0.58

4.2 Analysis of Variance (ANOVA)

The purpose of the analysis of variance (ANOVA) is to investigate which burnishing parameters significantly affect the performance characteristices. This is accomplished by separating the total variability of the grey relational grades, which is measured by the sum of the squared deviations from the total mean of the grey relational grade, into contributions by each burnishing parameters and the error. Thus;

$$SS_T = SS_F + SS_e \quad (6)$$

where

$$SS_T = \sum_{j=1}^{p}(\gamma_j - \gamma_m)^2 \quad (7)$$

and

SS_T Total sum of squared deviations about the mean
γ_j Mean response for j^{th} experiment
γ_m Grand mean of the response
p Number of experiments in the orthogonal array
SS_F Sum of squared deviations due to each factor
SS_e Sum of squared deviations due to error

In addition, the *F* test was used to determine which burnishing parameters have a significant effect on the performance characteristic. Usually, the change of the burnishing parameter has a significant effect on the performance characteristics when the *F* value is large. ANOVA for overall Grey relational grade is shown in **Table 10**.

Table 10: ANOVA results
Tabela 10: ANOVA rezultati

Parameter	Degree of Freedom	Sum of Square	Mean Square	F	Contribution (%)
F	3	0.300	0.100	19.00	71.59
N	3	0.066	0.022	4.20	15.75
f	3	0.043	0.014	2.72	10.26
V	3	0.009	0.003	0.63	2.14
Error	3	0.001	0.005		0.23
Total	15	0.419			100

According to this analysis, the most effective parameters with respect to surface roughness and microhardness are burnishing force, number of passes, burnishing feed and burnishing speed. Percent contribution indicates the relative power of a factor to reduce variation. For a factor with a high percent contribution, has a great influence on the performance. The percent contributions of the burnishing parameters on the surface roughness and microhardness are shown in **Table 10** and **Figure 4**. Burnishing force (*71.59%*) was found to be the major factor affecting surface roughness and microhardness, whereas number of passes (*15.75%*), burnishing feed (*10.26%*) and burnishing speed (*2.14%*) were found to be the second, third and fourth ranking factor respectively.

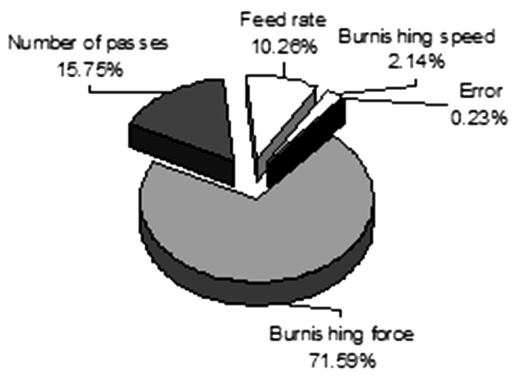

Figure 4: Contribution percentage of the burnishing parameters
Slika 4: Odstotna porazdelitev parametrov glajenja

4.3 Confirmation Test

After evaluating the optimal parameter settings, the next step is to predict and verify the enhancement of quality characteristics using the optimal parametric combination. The estimated Grey relational grade $\hat{\gamma}$ using the optimal level of the design parameters can be calculated as:

$$\hat{\gamma} = \gamma_m + \sum_{i=1}^{o} (\overline{\gamma}_j - \gamma_m) \quad (8)$$

where γ_m is the total mean Grey relational grade, $\overline{\gamma}_i$ is the mean Grey relational grade at the optimal level, and *o* is the number of the main design parameters that affect the quality characteristics. **Table 11** indicates the comparison of the predicted surface roughness and microhardness with that of actual by using the optimal burnishing conditions; good agreement between the actual and predicted results was obtained. Also, improvement in overall Grey relational grade was found to be as *0.65*.

Table 11: Results of confirmation test
Tabela 11: Rezultati potrditvenih preizkusov

	Initial factor settings	Optimal process condition	
		Prediction	Experiment
Factor levels	$F_1N_1f_1V_1$	$F_4N_3f_1V_4$	$F_4N_3f_1V_4$
Ra	0.61		0.12
HV_{100}	160		200
S/N ratio of overall Grey relational grade	-9.54	-0.51	-0.80
Overall Grey relational grade	0.33	0.91	0.98

Improvement in Grey relational grade=0.65

In Taguchi method, the only performance feature is the overall Grey relational grade and the aim should be to search a parameter setting that can achieve highest overall Grey relational grade. The Grey relational grade is the representative of all individual performance characteristics. In this study, objective functions have been selected in relation to parameters of surface roughness and microhardness. The weight calculations were done by using Analytic Hierarchy Process (AHP) and the weights were found to be as *0.67* and *0.33* for the responses of surface roughness and microhardness respectively. The results showed that using optimal parameter setting ($F_4N_3f_1V_4$) caused lower microhardness together with higher microhardness.

5 CONCLUSIONS

Taguchi method is a very effective tool for process optimization under limited number of experimental runs. Essential requirements for all types burnishing processes are smoother surface with higher surface hardness. This study has concentrated on the application of Taguchi method coupled with Grey relation analysis for solving

multi criteria optimization problem in the field of burnishing process. Experimental results have shown that surface roughness and microhardness of burnished aluminum alloy are greatly improved by using Grey based Taguchi method.

6 REFERENCES

[1] L. Kukielka, Journal of Mechanical Technology, 19 **(1989)**, 319–356

[2] M. H. El-Axir, International Journal of Machine Tools & Manufacture, 40 **(2000)**, 1603–1617

[3] N. H. Loh, S. C. Tam, S. Miyazawa, Journal of Mechanical Working Technology, 18 **(1989)**, 53–61

[4] A. M. Hassan, Journal of Materials Processing Technology, 72 **(1997)**, 385–391

[5] C. Wick, R. F. Veilleux, Soc. Manuf. Eng., 3 **(1985)**, 16–38

[6] T. Siva Prasad, B. Kotiveerachari, J. Inst. Eng., 69 **(1988)**, 55–58

[7] G. Y. Shneider, Machines and Tooling, 1 **(1989)**, 34–35

[8] A. N. Niberg, Soviet Engineering Research, 7 **(1987)**, 67

[9] P. C. Michael, N. Saka, E. Rabinowicz, Wear, 132 **(1989)**, 265

[10] N. H. Loh, S. C. Tam, S. Miyazawa, Wear, 129 **(1989)**, 235

[11] I. Yashcheritsyn, E. I. Pyatosin, V. V. Votchuga, Soviet Journal of Friction and Wear, 8 **(1987)**, 87

[12] M. Fattouh, M. H. El-Axir, S. M. Serage, Wear, 100 **(1988)**, 127

[13] A. S. H. Al-Bsharat, Investigation into the effect of burnishing process on some properties of cylindrical metallic materials, Jordan University of Science and Technology, MSc Thesis, **(1994)**

[14] O. M. Abd Al-Wahhab, The effects of roller-burnishing on some properties of non-ferrous metals, Jordan University of Science and Technology, MSc Thesis, **(1996)**

[15] S. Datta, A. Bandyopadhyay, P. K. Pal, International Journal of Advanced Manufacturing Technology, 39 **(2008)**, 1136–1143

[16] W. H., Yang, Y. S. Tarng, Journal of Materials Processing Technology, 84 **(1998)**, 122–129

[17] H. Rowlands, J. Antony, The TQM Magazine, 12 **(2000)**, 78–83

[18] S. H. Lim, C. M. Lee, W. J. Chung, International Journal of Precision Engineering and Manufacturing, 7 **(2006)**, 18–23

[19] D. C. Chen, C. F. Chen, Journal of Materials Processing Technology, 190 **(2007)**, 130–137

[20] C. P. Fung, P. C. Kang, Journal of Materials Processing Technology, 170 **(2005)**, 602–610

[21] S. H. Tang, V. J. Tan, S. M. Sapuan, S. Sulaiman, N. Ismail, R. Samin, Journal of Materials Processing Technology, 182 **(2007)**, 418–426

[22] P. Vijian, V. P. Arunachalam, Journal of Materials Processing Technology, 180 **(2006)**, 161–166

[23] L. J. Yang, Journal of Materials Processing Technology, 185 **(2007)**, 113–119

[24] J. Z. Zhang, J. C. Chen, E. D. Kirby, Journal of Materials Processing Technology, 184 **(2007)**, 233–239

[25] U. Esme, A. Sagbas, F. Kahraman, M. K. Kulekci, Materials and Technology 42 **(2008)**, 215–219

[26] F. C. Kung, Y. J. Weng, Polymer-Plastics Technology and Engineering, 47 **(2008)**, 1154–1161

UDK 669.131:669.85/.86
Original scientific article/Izvirni znanstveni članek

ISSN 1580-2949
MTAEC9, 44(3)137(2010)

EFFECT OF CERIUM ADDITIONS ON THE AlSi17 CASTING ALLOY

DODATEK CERIJA LIVNI ZLITINI AlSi17

Stanislav Kores, Maja Vončina, Borut Kosec, Primož Mrvar, Jožef Medved

University of Ljubljana, Faculty of Natural Sciences and Engineering, Department of Materials and Metallurgy, Aškerčeva 12, 1000 Ljubljana, Slovenia
stanislav.kores@ntf.uni-lj.si

Prejem rokopisa – received: 2010-01-08; sprejem za objavo – accepted for publication: 2010-02-01

The influence of the primary silicon phase and of eutectic silicon on the solidification process of hypereutectic Al-Si alloys with the addition of cerium is presented. The solidification was analyzed by a simple thermal analysis and a simultaneous thermal analysis, and the microstructures were examined with conventional light microscopy and scanning electron microscopy. The simultaneous refinement of both the primary and the eutectic silicon particles was achieved with cerium additions. The results showed that the addition of cerium had a very positive influence on the alloy's tensile strength.

Keywords: hypereutectic Al-Si alloys, cerium, silicon refinement, modification

Članek opisuje vpliv dodatka cerija na primarno fazo silicija in na evtektski silicij pri strjevanju nadevtektskih Al-Si-zlitinah. Proces strjevanja je bil analiziran z enostavno in s simultano termično analizo. S konvencionalnim svetlobnim mikroskopom ter z elektronskim mikroskopom je bila opravljena mikrostrukturna analiza. Z dodatkom cerija je bilo doseženo udrobnjevanje tako primarno izločene faze silicija kot tudi evtektskega silicija. Preiskave so pokazale, da ima dodatek cerija pozitiven učinek na natezno trdnost zlitin.

Ključne besede: nadevtektske Al-Si zlitine, cerij, udrobnjevanje silicija, modifikacija

1 INTRODUCTION

The application of aluminium alloys for automotive parts, such as pistons, cylinder liners, engine blocks and other parts is important because of the alloys' wear resistance, heat resistance and low thermal expansion.[1,2] The dominant group of Al-Si foundry alloys contains the mass fraction of Si between 5 and 25 %, and additions of Mg, Ni and Cu. Silicon, as the major alloying addition, represents one of the most effective ways to obtain high-quality aluminium casting alloys, mainly because of their high fluidity due to the relatively large volume of the Al-Si eutectic.[3,4] Al-Si alloys with more than 12 % Si have a hypereutectic microstructure, usually consisting of a primary silicon phase in a eutectic matrix. These alloys are used for engine blocks or cylinder liners, and are the ideal solution for the substitution of cast-iron cylinder liners in the manufacturing of a monolithic engine block.[5,3]

The primary silicon phase has a harmful effect on the extrudability, machinability, strength, and ductility of the alloy, since coarse silicon phases lead to premature crack initiation and fracture when in tension.[4] With the aim to avoid these problems, the structural modifications are achieved with the addition of elements that refine the silicon phases to a better shape.[1]

The use of silicon modifiers and high cooling rates refines the primary silicon particles.[6] Sodium and strontium are both effective modifiers of the Al-Si eutectic, but it is difficult to control and maintain the modification effect of sodium because of the volatilization and oxidation losses, especially when longer holding times and higher temperatures are required. Strontium does not cause such problems; however, it is reported that it may cause micro- and macroporosity in Al-Si alloy castings.[7] The refinement of primary silicon grains is usually achieved with the addition of phosphorus to the melt. The diagram in **Figure 1** shows the influence of phosphorus additions on the size of the primary silicon grains[8]. It is reported[4,7–12] that rare-earth elements are capable of modifying the Al-Si eutectic too, and it has also been proved that rare-earth elements

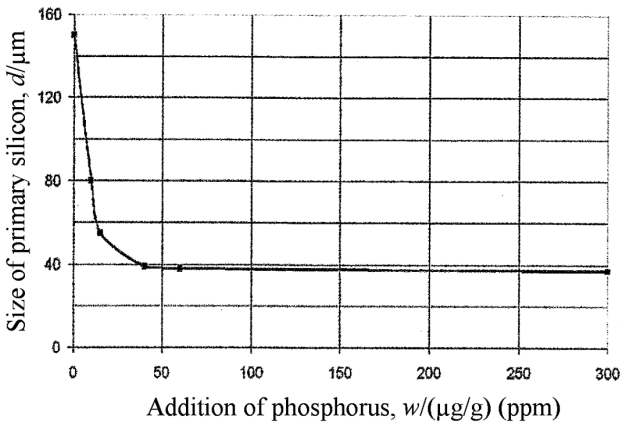

Figure 1: Influence of phosphorus additions on the refinement of primary silicon particles[7]

Slika 1: Vpliv dodatka fosforja na udrobnitev primarnega silicija[7]

represent one way to achieve longer effects for refining agents.[7] It is, for example, mentioned in reference[13] that cerium did not refine the primary silicon grains, but it had a moderate effect on modifying the silicon eutectic. A small cerium addition could provide ternary high-temperature stable τ_1 and τ_2 phases in equilibrium with the Al-Si-rich melt. These phases might act as nucleation sites for (aluminium) or (silicon) particles in both hypo- and hypereutectic Al-Si alloys.[14] Kowata et al.[15] reported that the primary Si in hypereutectic Al-20 % Si alloys was refined with rare-earth metals.

The goal of the present investigation was to check the possibility of whether cerium acted as a refining agent for the primary silicon phase and the silicon eutectic in the pure AlSi17 alloy and in the commercial AlSi17CuMg alloy. The influence of various cerium additions on the tensile strength was also examined.

2 EXPERIMENTAL

Pure Al-Si alloys with the mass fraction of Si 17 % and the commercial AlSi17CuMg alloy and various additions of cerium were used for the experiments. The alloys were melted in an electric resistance furnace in a 3-kg crucible and cerium was added as a 99.9 % pure metal. The melt with a temperature of 750 °C was poured into the measuring cast-iron cell for the thermal analysis. The cooling curve was recorded with a K-type thermocouple at a cooling rate of approximately 20 K/s. With the Thermo-Calc program we recorded all the thermodynamically possible equilibrium phases existing under the defined conditions. The equilibrium binary phase diagram was determined and the composition of the microstructure could be predicted. The samples for light microscopy were prepared with a standard metallographic procedure and examined with an Olympus BX61 light microscope equipped with a DP 70 video camera. The simultaneous thermal analysis (STA) of specimens of the starting materials was performed with the STA 449 Netzsch apparatus. Two equal corundum cups were placed on the platinum sensor. One contained the examined material, the other one, which was empty, represented the reference material. The measurements were carried out in a protective atmosphere of 99.999 % pure argon. The specimens were heated up to 720 °C at a heating rate of 10 K/min and cooled with the same cooling rate to room temperature.

3 RESULTS AND DISCUSSION

To act as a nucleus, the compound must precipitate prior to the primary silicon phase. A thermodynamic simulation of the AlSi17 alloy with 80 µg/g (ppm) phosphorus was made with the Thermo-Calc program, and **Figure 2 a** shows that the AlP compound precipitates before the primary silicon phase.

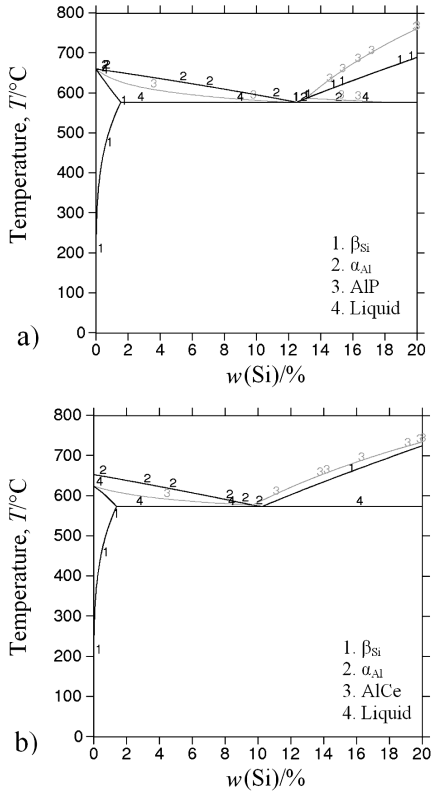

Figure 2: Isopleth diagram of AlSi17 alloy with 80 µg/g (ppm) P (a), and the mass fraction of Ce w(Ce) = 4.5 % (b)

Slika 2: Izopletni fazni diagram zlitine AlSi17 z 80 µg/g (ppm) P (a) in masni delež Ce w(Ce) = 4,5 % (b)

The evidence that cerium also forms nuclei, a simulation with the Thermo-Calc program, was carried out for various additions of cerium. **Figure 2 b** presents the isopleths of the phase diagram for the AlSi17 alloy with 4.5 % Ce. It is evident that the AlCe compound precipitated before the primary silicon. The several proposed mechanisms of refinement for primary silicon grains by the addition of phosphorus can be summarized as follows. The widely accepted and popular theory is based on the nucleation of silicon grains on the AlP compound when phosphorus is added to the alloy. It has been proposed that the AlP compound with the melting point above 982 °C and a cubic structure similar to that of silicon, acted as a nucleation agent and with heterogeneous nucleation produced the refinement of the primary grains [4].

The modification effect of the cerium addition on the solidification of the AlSi17 alloy is shown on the cooling curve in **Figure 3**. The addition of 0.5 % Ce affected the primary silicon size distribution, and this could be seen on the cooling curve without undercooling. The solidification time was shorter than with the pure AlSi17 alloy. The diagram demonstrates that the alloy with 4.5 % Ce had a lower liquidus temperature, below 600 °C. At the same time, the solidification time was longer than for the pure alloy. The idea that added cerium formed nuclei for the primary silicon precipitation was refuted,

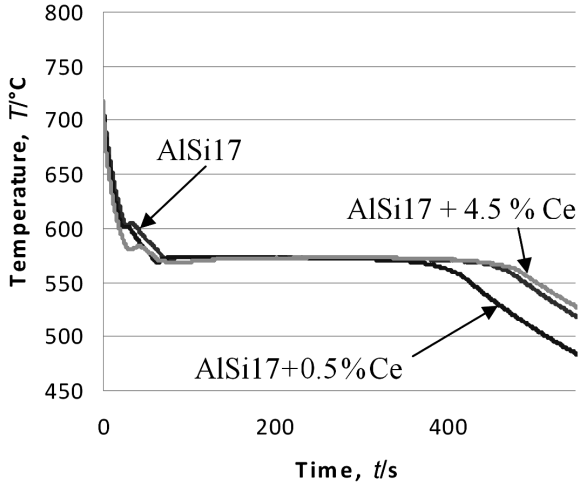

Figure 3: Effect of cerium addition on the AlSi17 alloy
Slika 3: Učinek dodatka cerija na zlitino AlSi17

since the liquidus temperature was lower than with the pure alloy.

Figure 4 shows the microstructures of the unmodified (**a**) and modified AlSi17 alloy with 1 % Ce (**b**) in the light microscope. It demonstrates that this addition modified the size of the primary silicon grains, from coarse shapes to fine polyhedral shapes. Also, the microstructure of the eutectic was finer.

The microstructure of the AlSi17 alloy with 4.5 % Ce is presented in **Figure 5**. It demonstrates that the higher

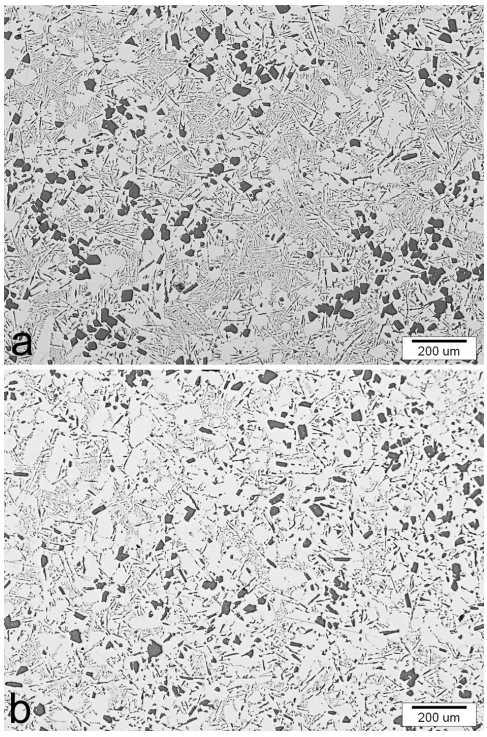

Figure 4: Microstructures of the AlSi17 alloy (a) and the alloy with w = 1 % addition of cerium
Slika 4: Mikrostruktura zlitine AlSi17 (a) in zlitine z dodatkom w = 1 % cerija

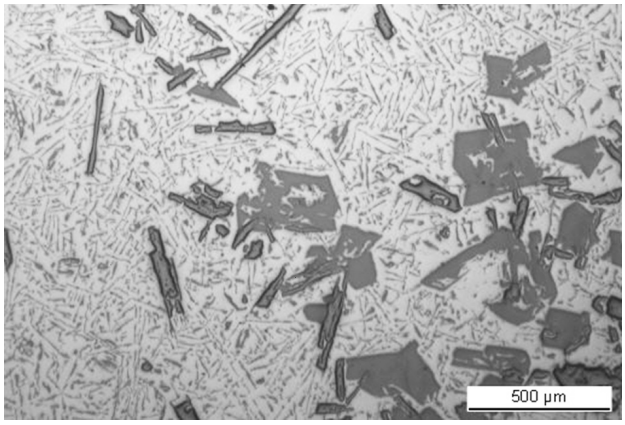

Figure 5: AlSi17 alloy with w = 4.5 % Ce
Slika 5: Zlitina AlSi17 z w = 4,5 % Ce

cerium content does not cause the refinement of the primary silicon grains. A phase with a highly polyhedral shape that contained cerium was found in the microstructure.

STA was performed with specimens from the thermal analysis. **Figure 6** indicated that the liquidus temperature of the alloy decreased with an increasing cerium content. The greatest reduction of the liquidus temperature was with the alloy containing 1 % Ce, and the drop was from 686.6 °C (pure AlSi17 alloy) to 591.9 °C.

With the aim to prove that pure cerium possibly forms nuclei, the sample containing 1 % cerium was

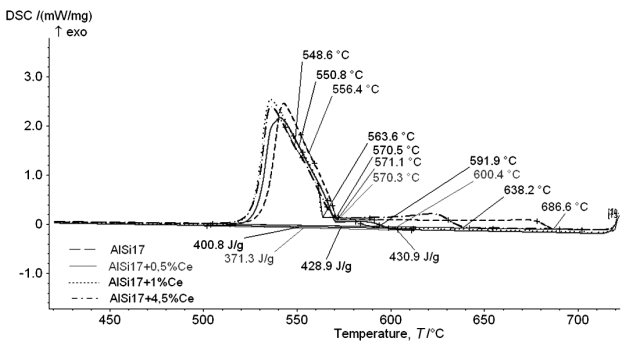

Figure 6: DSC-curves for the AlSi17 alloy with various additions of cerium
Slika 6: DSC-krivulje zlitine AlSi17 z različnimi dodatki cerija

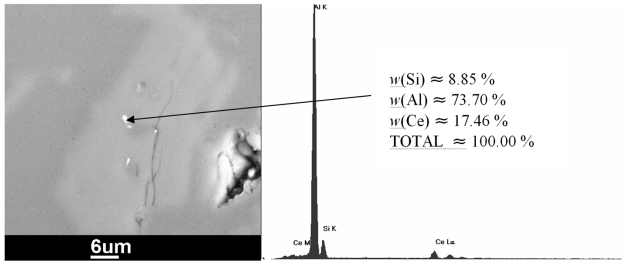

Figure 7: Scanning electron micrograph of the AlSi17 with w = 1 % Ce
Slika 7: Posnetek z vrstičnim elektronskim mikroskopom zlitine AlSi17 z w = 1 % Ce

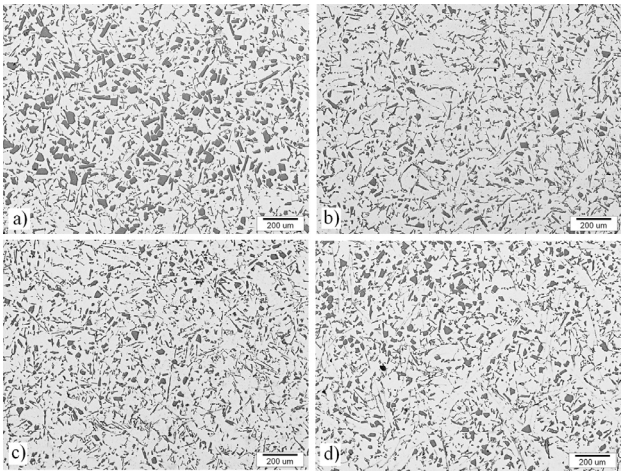

Figure 8: Influence of cerium additions on the microstructure of the AlSi17CuMg alloy; a) pure alloy, b) with mass fractions w = 0.5 % Ce, c) with w = 1 % Ce, d) with w = 1.5 % Ce

Slika 8: Vpliv dodatka cerija na mikrostrukturo zlitine AlSi17CuMg, a) brez dodatka, b) z masnimi deleži w = 0,5 % Ce, c) z w = 1 % Ce, d) z w = 1,5 % Ce

examined with a scanning electron microscope. **Figure 7** shows a micrograph of the examined alloy. Cerium did not form any nuclei for the precipitation of the primary silicon phase and precipitated on the surface of the primary silicon phase itself.

The examination of various cerium additions to the commercial AlSi17CuMg alloy with the mass fractions 1.6 % Cu, and 0.3 % Mg was performed too. **Figures 8 a to 8 d** show the microstructures of the base AlSi17CuMg alloy (a), of alloys with 0.5 mass % Ce (b), with 1 mass % Ce (c) and with 1.5 % Ce. The addition of 1 % Ce had the greatest effect with regards to refining the primary silicon phase and also of the Al-Si eutectic.

The influence of cerium additions on the mechanical properties of the AlSi17CuMg alloy was determined with tensile tests. The results of the tensile strength tests are presented in **Table 1**. It was found that the cerium additions had a positive influence on the tensile strength.

Table 1: Tensile strengths of the examined test samples
Tabela 1: Natezne trdnosti preiskovanih vzorcev

Alloy	Pure alloy	with w = 0.5 % Ce	with w = 1 % Ce	with w = 1.5 % Ce
AlSi17CuMg	170 MPa	192 MPa	195 MPa	186 MPa

4 CONCLUSIONS

The refinement of the primary silicon and of the eutectic silicon morphology was achieved with additions of cerium (up to 1 % Ce) to hypereutectic Al-Si alloys. The best results for the microstructural and strength properties were obtained with the addition of 1 % Ce. With an increase in the cerium additions, the precipitation temperature of the primary silicon phase decreased. The addition of 1 % Ce produced the greatest reduction in the liquidus temperature, from 686.6 °C to 591.9 °C.

5 REFERENCES

[1] Y. Hong-Kun, Z. Di, Transactions of Nonferrous Metals Society, China, April (**2003**) 358
[2] O. Zak, B. Tonn, Giesserei-Praxis, Germany, September (**2009**) 281
[3] F. C. Robles Hernandez, J. H. Sokolowski, Journal of Alloys and Compounds, 419 (**2006**), 180
[4] J. Chang, I. Moon, C. Choi, Journal of Materials Science 33 (**1998**) 5015
[5] J. E. Gruzleski and B. M. Closset, American Foundrymen's Society, Inc., Des Plaines, Illinois, (**1990**) 19
[6] L. Bäckerud, G. Chai, J. Tamminem, Solidification Characteristics of Aluminium Alloys, American Foundry Society/Skanaluminium, U. S. A Vol. 3. (1990)
[7] B. J. Ye, C. R. Jr. Loper, D.Y. Lu, et al., AFS Transaction, 30 (**1985**) 533
[8] W. Vogel, V. Schneider, Giesserei 78, Nr. 23, (**1991**), 848–852
[9] H. Sano, Metal Powder Report (UK), 49 (1) (**1994**) 26
[10] J. Y. Chang, G. H. Kim, I. G. Moon at al., Scripta Materialia, 39 (**1998**) 307
[11] R. Sharan, N. P. Saksen, International Cast Metals Journal 3 (**1978**) 29
[12] M. Ravi, U. T. S. Pillai, G. C. Pai, Metallurgical and Materials Transactions 27A (**1996**) 1283
[13] J. C. Wiess, C. R. Loper Jr., AFS Transaction 32 (**1987**) 51
[14] J. Gröbner, D. Mirković, R. Schmid-Fetzer, Metallurgical and Materials Transactions A, 35A (**2004**) 3349
[15] T. Kowata, H. Horie, S. Hiratsuka, A. Chida, Imono 66 (**1994**) 803

UDK 539.374.001.8.621.7-111
Original scientific article/Izvirni znanstveni članek

ISSN 1580-2949
MTAEC9, 44(3)141(2010)

A GENERALIZED THEORY OF PLASTICITY

POSPLOŠENA TEORIJA PLASTIČNOSTI

Chygyryns'kyy Victorovich Valeryy[1], Kachan Aleksey Yakovlevich[1], Ilija Mamuzić[2], Ben' Anna Nikolaevna[1]

[1]Zaporozhskyy National Technical University, Str. Zukovsky 64, 69063 Zaporozhskye, Ukraine
[2]University of Zagreb, Faculty for Metallurgy, Aleja narodnih heroja 3, 44000 Sisak, Croatia
valerij@zntu.edu.ua

Prejem rokopisa – received: 2008-11-21; sprejem za objavo – accepted for publication: 2009-11-23

A closed solution of the plane problem of the generalized theory of plasticity and a model of the complex plastic medium were theoretically developed. Solutions with the use of the deformation theory and the theory of plastic yielding were developed. The solution for a simple strengthening medium was deduced.

Key words: metal plasticity, analytical solution, mathematical model, plastic medium, process parameters

Razvita sta bila zaprta rešitev splošne teorije plastičnosti in teoretičen model kompleksnega plastičnega medija. Opredeljene so bile rešitve z uporabo teorije deformacije in teorije plastičnega tečenja. Razvita je bila rešitev za preprost utrditveni medij.

Ključne besede: plastičnost kovin, analitična rešitev, matermatični model, plastični medij, parametri procesa

1 INTRODUCTION

A characteristic of the new method based on a closed solution of the plane problem of theory of plasticity is a simplified analysis of the deformation mode of the medium and the theoretical connection to the medium mechanical characteristics through the process parameters. The analytical solution of the plane problem of the theory of plasticity for a strengthening medium is known.[1] The developed complex model for the strengthening of the plastic medium is based on the shear resistance to the plastic deformation and is a function of the coordinates of the nucleus of deformation. This approach offers a new possibility to evolve a new solution for a problem, including the generalized theory of plasticity. The approach includes equations and criteria: an equilibrium equation, and the criteria of yielding, the equation of incompressibility, of the deformation rate and the deformation as well as equations of continuity of the deformation rate and the deformation:

– the equilibrium equations

$$\frac{\partial \sigma_x}{\partial x}+\frac{\partial \tau_{xy}}{\partial y}=0;\ \frac{\partial \tau_{xy}}{\partial x}+\frac{\partial \sigma_y}{\partial y}=0$$

– the criterion of yielding

$$(\sigma_x-\sigma_y)^2+4\cdot\tau_{xy}^2=4\cdot k^2$$

– the constraint equations for the rates of deformation and deformation

$$\frac{\sigma_x-\sigma_y}{2\cdot\tau_{xy}}=\frac{\xi_x-\xi_y}{\gamma'_{xy}}=F_1;\ \frac{\sigma_x-\sigma_y}{2\cdot\tau_{xy}}=\frac{\varepsilon_x-\varepsilon_y}{\gamma_{xy}}=F_2 \quad (1)$$

– the equations of incompressibility for the rates of deformation and the deformation

$$\xi_x+\xi_y=0;\ \varepsilon_x+\varepsilon_y=0$$

– the equation of continuity for the deformation rates and the deformation

$$\frac{\partial^2 \xi_x}{\partial y^2}+\frac{\partial^2 \xi_y}{\partial x^2}=\frac{\partial^2 \gamma'_{xy}}{\partial y\partial x};$$

$$\frac{\partial^2 \varepsilon_x}{\partial y^2}+\frac{\partial^2 \varepsilon_y}{\partial x^2}=\frac{\partial^2 \gamma_{xy}}{\partial y\partial x}$$

– the equation of heat conductivity

$$a^2\left(\frac{\partial^2 T}{\partial x^2}+\frac{\partial^2 T}{\partial y^2}\right)=\frac{\partial T}{\partial t}$$

The model of the complex plastic medium is defined with

$$T_i=\chi\cdot(H_i)^{m_1}\cdot(\Gamma_i)^{m_2}\cdot(T)^{m_3} \quad (2)$$

The system of equations (1) includes the equations of the deformation theory of plasticity and the theory of plastic yielding with the addition of the equation of heat conductivity.[2] The model (2) is a real strengthening medium with the boundary conditions for stresses[3]

$$\tau_n=T_i\cdot\sin[A\Phi-2\alpha],\ T_i=k$$

or

$$\tau_n=\frac{\sigma_x-\sigma_y}{2}\cdot\sin 2\alpha-\tau_{xy}\cdot\cos 2\alpha \quad (3)$$

The additional conditions are given by the specific contact forces (3) of the change of friction according to the sinusoidal law of deformational and high-speed strain hardening. All the intensities and the temperature depend on the coordinates of the deformation nucleus.

2 THEORETICAL DEVELOPMENT

With the aim to obtain the model (2), let us consider three second-order equations in form of non-uniform hyperbolic partial derivations:

$$\frac{\partial^2 \tau_{xy}}{\partial x^2}-\frac{\partial^2 \tau_{xy}}{\partial y^2}=2\cdot\frac{\partial^2}{\partial y\partial x}\sqrt{k^2-\tau_{xy}^2},$$
$$\frac{\partial^2 \xi_x}{\partial y^2}-\frac{\partial^2 \xi_x}{\partial x^2}=2\cdot\frac{\partial^2}{\partial y\partial x}\frac{1}{F_1}\cdot\xi_x \qquad (4)$$
$$\frac{\partial^2 \varepsilon_x}{\partial y^2}-\frac{\partial^2 \varepsilon_x}{\partial x^2}=2\cdot\frac{\partial^2}{\partial y\partial x}\frac{1}{F_2}\cdot\varepsilon_x$$

The boundary conditions (3) correspond to the substitution $\tau_{xy}=k\cdot\sin A\Phi$. A complex dependence of the coordinates is assumed with $k=f(\Gamma_i, H_i, T, x, y)$. In this case, $k=C_\sigma\cdot\exp\theta'$, with $\theta'=f(\Gamma_i, H_i, T, x, y)$, with Γ_i, H_i, T standing for the intensity of the deformation, the rates of deformation and the temperature.

The derivatives are taken as for the complex function,[4] and after substitution in the first equation (3) we obtain:

$$\begin{aligned}&\{(\theta'_H\cdot H_x+\theta'_s\cdot\Gamma_x+\theta'_t\cdot T_x)_x+[(\theta'_H\cdot H_x+\theta'_s\cdot\Gamma_x+\\&+\theta'_t\cdot T_x)+A\Phi_y]^2-(\theta'_H\cdot H_y+\theta'_s\cdot\Gamma_y+\theta'_t\cdot T_y)_y-\\&-[(\theta'_H\cdot H_y+\theta'_s\cdot\Gamma_y+\theta'_t\cdot T_y)-A\Phi_x]^2+2A\Phi_{xy}\}\cdot\\&\cdot\sin(A\Phi)+\{2\cdot[(\theta'_H\cdot H_x+\theta'_s\cdot\Gamma_x+\theta'_t\cdot T_x)+A\Phi_y]\cdot\\&\cdot[A\Phi_x-(\theta'_H\cdot H_y+\theta'_s\cdot\Gamma_y+\theta'_t\cdot T_y)]+A\Phi_{xx}-\\&-A\Phi_{yy}-2\cdot(\theta'_{HH}\cdot H_x\cdot H_y+\theta'_H\cdot H_{xy}+\\&-\theta'_{ss}\cdot\Gamma_x\cdot\Gamma_y+\theta'_s\cdot\Gamma_{xy}+\theta'_{tt}\cdot T_x\cdot T_y+\theta'_t\cdot T_{xy})\}\cdot\\&\cdot\cos(A\Phi)=0\end{aligned} \qquad (5)$$

Equation (5) is equal to zero if the parts in the square brackets are equal to zero. Then,

$$\begin{aligned}\theta'_H\cdot H_x+\theta'_s\cdot\Gamma_x+\theta'_t\cdot T_x&=A\Phi_y\\\theta'_H\cdot H_y+\theta'_s\cdot\Gamma_y+\theta'_t\cdot T_y&=A\Phi_x\\(\theta'_H\cdot H_x+\theta'_s\cdot\Gamma_x+\theta'_t\cdot T_x)_x&=-A\Phi_{yx}\\(\theta'_H\cdot H_y+\theta'_s\cdot\Gamma_y+\theta'_t\cdot T_y)_y&=-A\Phi_{xy}\\A\Phi_{yy}=-(\theta'_{HH}\cdot H_x\cdot H_y+\theta'_H\cdot H_{xy}+\theta'_{ss}\cdot\Gamma_x\cdot\Gamma_y+&\\+\theta'_s\cdot\Gamma_{xy}+\theta'_{tt}\cdot T_x\cdot T_y+\theta'_t\cdot T_{xy})&\\A\Phi_{xx}=(\theta'_{HH}\cdot H_x\cdot H_y+\theta'_H\cdot H_{xy}+\theta'_{ss}\cdot\Gamma_x\cdot\Gamma_y+&\\+\theta'_s\cdot\Gamma_{xy}+\theta'_{tt}\cdot T_x\cdot T_y+\theta'_t\cdot T_{xy})&\end{aligned}$$

The operations with the complex function allow us to determine the exponent index as the sum of three functions accounting for the effect of the deformation degree and the rate, and of the temperature:

$$\theta'=-A\theta=\theta'_1+\theta'_2+\theta'_3=-(A'_1\theta+A'_2\theta+A'_3\theta)$$

The shear resistance and the components of the tensor of the stresses are:

$$k=C_\sigma\cdot\exp(-A'_1\theta)\cdot\exp(-A'_2\theta)\cdot\exp(-A'_3\theta)\cdot\sin(A\Phi) \qquad (6)$$

$$\begin{aligned}\sigma_x&=C_\sigma\cdot\exp(-A'_1\theta)\cdot\exp(-A'_2\theta)\cdot\exp(-A'_3\theta)\cdot\cos(A\Phi)+\\&+\sigma_0+f(y)+C\\\sigma_y&=-C_\sigma\cdot\exp(-A'_1\theta)\cdot\exp(-A'_2\theta)\cdot\exp(-A'_3\theta)\cdot\cos(A\Phi)+\\&+\sigma_0+f(x)+C\end{aligned}$$

with $\theta'_x=(\theta'_1)_x+(\theta'_2)_x+(\theta'_3)_x=-A\Phi_y$

$\theta'_y=(\theta'_1)_y+(\theta'_2)_y+(\theta'_3)_y=A\Phi_x$

By substituting the stress values into the equation of constraint we obtain:

$$\frac{\sigma_x-\sigma_y}{2\tau_{xy}}=\operatorname{ctg}A\Phi;\ \frac{\xi_x-\xi_y}{\gamma'_{xy}}=\operatorname{ctg}B_1\Phi$$
$$\operatorname{ctg}A\Phi=\operatorname{ctg}B_1\Phi=F_1$$
$$\frac{\varepsilon_x-\varepsilon_y}{\gamma'_{xy}}=\operatorname{ctg}B_2\Phi$$
$$\operatorname{ctg}A\Phi=\operatorname{ctg}B_2\Phi=F_2$$

It is possible to establish the relation between the shears and the linear figures of the deformation rates and the deformations. Taking into account the equations of non-compressibility we obtain:

$$\gamma'_{xy}=2\cdot\frac{1}{F_1}\cdot\xi_x=2\cdot\xi_x\cdot\operatorname{tg}B_1\Phi$$
$$\gamma_{xy}=2\cdot\frac{1}{F_2}\cdot\varepsilon_x=2\cdot\varepsilon_x\cdot\operatorname{tg}B_2\Phi$$

In order to simplify, we define:

$$\xi_x=C_\xi\cdot\exp\theta''_1\cdot\cos B_1\Phi$$
$$\varepsilon_x=C_\varepsilon\cdot\exp\theta''_2\cdot\cos B_2\Phi$$

By substituting these relations into the equations of continuity of the deformation rate and the deformation (1) or (4), we obtain:

$$\begin{aligned}&[-\theta''_{1xx}-(\theta''_{1x}+B_1\Phi_y)^2+\theta''_{1yy}+(\theta''_{1y}-B_1\Phi_x)]\cdot\sin B_1\Phi+\\&+[2(B_1\Phi_x-\theta''_{1y})\cdot(\theta''_{1x}+B_1\Phi_y)+(B_1\Phi_{xx}-B_1\Phi_{yy})]\cdot\\&\cdot\cos B_1\Phi=2\cdot B_1\Phi_{xy}\cdot\sin B_1\Phi+2\cdot\theta''_{1xy}\cdot\cos B_1\Phi\end{aligned} \qquad (7)$$

as well as

$$\begin{aligned}&[-\theta''_{2xx}-(\theta''_{2x}+B_2\Phi_y)^2+\theta''_{2yy}+(\theta''_{2y}-B_2\Phi_x)]\cdot\sin B_2\Phi+\\&+[2(B_2\Phi_x-\theta''_{2y})\cdot(\theta''_{2x}+B_2\Phi_y)+(B_2\Phi_{xx}-B_2\Phi_{yy})]\cdot\\&\cdot\cos B_2\Phi=2\cdot B_2\Phi_{xy}\cdot\sin B_2\Phi+2\cdot\theta''_{2xy}\cdot\cos B_2\Phi\end{aligned} \qquad (8)$$

Brackets identical to (5) appear in equations (7) and (8). For

$$(\theta''_1)_x=-B_1\Phi_y\quad(\theta''_1)_y=B_1\Phi_x$$
$$(\theta''_2)_x=-B_2\Phi_y\quad(\theta''_2)_y=B_2\Phi_x$$

the equations are transformed into identities, with, $\theta''_1=-B_1\theta$, $\theta''_2=-B_2\theta$ as the indices of the exponents of the functions determining the fields of the deformation rate and the deformation, $B_1\Phi$ and $B_2\Phi$ are the trigonometric functions determining the fields of the deformation rate and the deformation.

The expressions for the deformation rate and the deformation are:

$$\xi_x = -\xi_y = C_\xi \cdot \exp\theta_1'' \cdot \cos B_1\Phi = C_\xi \cdot \exp(-B_1\theta)\cdot \cos B_1\Phi \quad (9)$$

$$\gamma_{xy}' = C_\xi \cdot \exp\theta_1'' \cdot \sin B_1\Phi = C_\xi \cdot \exp(-B_1\theta)\cdot \sin B_1\Phi$$

$$H_i = 2C_\xi \cdot \exp\theta_1'' = 2C_\xi \cdot \exp(-B_1\theta)$$

$$\varepsilon_x = -\varepsilon_y = C_\varepsilon \cdot \exp\theta_2'' \cdot \cos B_2\Phi = C_\varepsilon \cdot \exp(-B_2\theta)\cdot \cos B_2\Phi \quad (10)$$

$$\gamma_{xy} = C_\varepsilon \cdot \exp\theta_2'' \cdot \sin B_2\Phi = C_\varepsilon \cdot \exp(-B_2\theta)\cdot \sin B_2\Phi$$

$$\Gamma_i = 2C_\varepsilon \cdot \exp\theta_2'' = 2C_\varepsilon \cdot \exp(-B_2\theta)$$

with $(\theta_1'')_y = B_1\Phi_x \quad (\theta_1'')_x = -B_1\Phi_y$

$(\theta_2'')_y = B_2\Phi_x \quad (\theta_2'')_x = -B_2\Phi_y$

With a comparison of expressions (9), (10) and (7) we can confirm that all the expressions have functional dependencies on the coordinates θ and Φ (the indices of the exponents and the examples of the trigonometric functions).

It is of interest to obtain similar dependencies for the solution for the temperature fields that could allow us to solve this task theoretically. Let us consider a differential equation for the stationary temperature field

$$\frac{\partial^2 T}{\partial x^2} + \frac{\partial^2 T}{\partial y^2} = 0$$

For this case we look for the solution in the form of

$$T = C_T \cdot \exp(\theta_3'') \cdot (\sin B_3\Phi + \cos B_3\Phi) \quad (11)$$

with: $(\theta_3'')_x = -B_3\Phi_y, \ (\theta_3'')_y = -B_3\Phi_x$

We will demonstrate that expression (11) is a solution of the Laplace equation. By substituting the derivatives (11) into the equation of the heat conductivity and a simplification we obtain:

$$\left\{(\theta_3'')_{xx} + \left[(\theta_3'')_x + B_3\Phi_y\right]\cdot\left[(\theta_3'')_x - B_3\Phi_y\right] + (\theta_3'')_{yy} + \left[(\theta_3'')_y + B_3\Phi_x\right]\cdot\left[(\theta_3'')_y - B_3\Phi_x\right]\right\}\cdot(\sin B_3\Phi + \cos B_3\Phi) + [2\cdot(\theta_3'')_x \cdot B_3\Phi_x + B_3\Phi_{xx} + 2\cdot(\theta_3'')_y \cdot B_3\Phi_y + B_3\Phi_{yy}]\cdot(\cos B_3\Phi - \sin B_3\Phi) = 0 \quad (12)$$

In the case of equality to zero, the brackets, $\left[(\theta_3'')_x + B_3\Phi_y\right]$, $\left[(\theta_3'')_y - B_3\Phi_x\right]$ in equation (12) establish a relation in the form of:

$$(\theta_3'')_{xx} = -B_3\Phi_{yx}, \ (\theta_3'')_{yy} = -B_3\Phi_{xy}$$

$$B_3\Phi_{xx} = (\theta_3'')_{yx}, \ B_3\Phi_{yy} = (\theta_{xy}'')$$

The last correlations correspond to Cauchy-Rieman condition and are functions determined by the Laplace equation corresponding to relation (11).

From the comparison of the solutions (7) to (11) (conditions superimposed on functions) it was concluded that $\theta_3'' = -B_3\theta$ for the stressed and deformed conditions and the temperature fields can be used to determine a common parametric function, which is included into the fields of the stresses, the deformations, the rates of deformation and the temperatures, allowing us to express them mathematically, one with another. Thus,

$$\exp(-\theta) = \left(\frac{H_i}{2\cdot C_\xi}\right)^{\frac{1}{B_1}} = \left(\frac{\Gamma_i}{2\cdot C_\varepsilon}\right)^{\frac{1}{B_2}} = \left(\frac{T}{C_T\cdot(\sin B_3\Phi + \cos B_3\Phi)}\right)^{\frac{1}{B_3}}$$

With substitution into an expression for resistance to deformation, we obtain

$$T_i = \chi\left(H_i\right)^{\frac{A_1'}{B_1}}\cdot\left(\Gamma_i\right)^{\frac{A_2'}{B_2}}\cdot(T')^{\frac{A_3'}{B_3}} \quad (13)$$

The form of expression (13) corresponds to a dependence of the yield stress from the rate, the degree of deformation and the temperature proposed in[1].

3 ANALYSIS OF THE RESULTS

In the analysis the expressions (6) are used to study the stressed condition of the plastic medium in the case of a flat upsetting of rough plates. If the problem is reduced to a more simple mathematical model ($A_2' = A_3' = 0$), expression (6) will correspond to the solutions in[5].

$$k = C_\sigma \cdot \exp(-A_1'\theta)$$

$$\tau_{xy} = C_\sigma \cdot \exp(-A_1'\theta)\cdot\sin(A\Phi)$$

$$\sigma_x = C_\sigma \cdot \exp(-A_1'\theta)\cdot\cos(A\Phi) + \sigma_0 + f(y) + C$$

$$\sigma_y = -C_\sigma \cdot \exp(-A_1'\theta)\cdot\cos(A\Phi) + \sigma_0 + f(x) + C \quad (14)$$

Applying the condition for plasticity $\sigma_0 = -2k\cdot\cos A\Phi$, $C = k_0$, the functions $A\Phi$ and θ become harmonic. Starting from the Laplace equation and the Cauchy-Rieman conditions we obtain the expressions for determining the functions in the form of the coordinate polynomial.

$$A\Phi = AA_6\cdot x\cdot y - AA_{13}\cdot x\cdot y\cdot(x^2 - y^2)$$

$$\theta' = -\left\{0.5\cdot AA_6\cdot(x^2 - y^2) - AA_{13}\cdot[0.25\cdot(x^4 + y^4) - 1.5\cdot x^2\cdot y^2]\right\}$$

The constants in the expressions were determined as proceeding from the real boundary conditions

$$AA_6 = 4\cdot\frac{\Psi_0}{l\cdot h}, \ AA_{13} = 16\cdot\Psi_1\cdot\frac{l - 2\cdot h}{l^3\cdot h\cdot(l + h)}$$

$$\Psi_0 = \text{arctg}\left[2\cdot f\cdot(1 - f)\right]$$

$$\Psi_1 = \text{arctg}\left[1.7\cdot f\cdot(1 - f)\right]$$

and the coefficient

$$C_\sigma = \frac{k_0}{\cos A\Phi_0}\cdot\exp(-\theta_0')$$

$$A\Phi_0 = AA_6\cdot\frac{l\cdot h}{4} - AA_{13}\cdot\frac{l\cdot h}{4}\cdot\left(\frac{l^2}{4} - \frac{h^2}{4}\right)$$

$$\theta_0' = -A\theta_0 = -\left\{0.5\cdot AA_6\cdot\left(\frac{l^2}{4} - \frac{h^2}{4}\right) - AA_{13}\left[0.25\cdot\left(\frac{l^4}{16} + \frac{h^4}{16}\right) - 1.5\cdot\frac{l^2\cdot h^2}{16}\right]\right\}$$

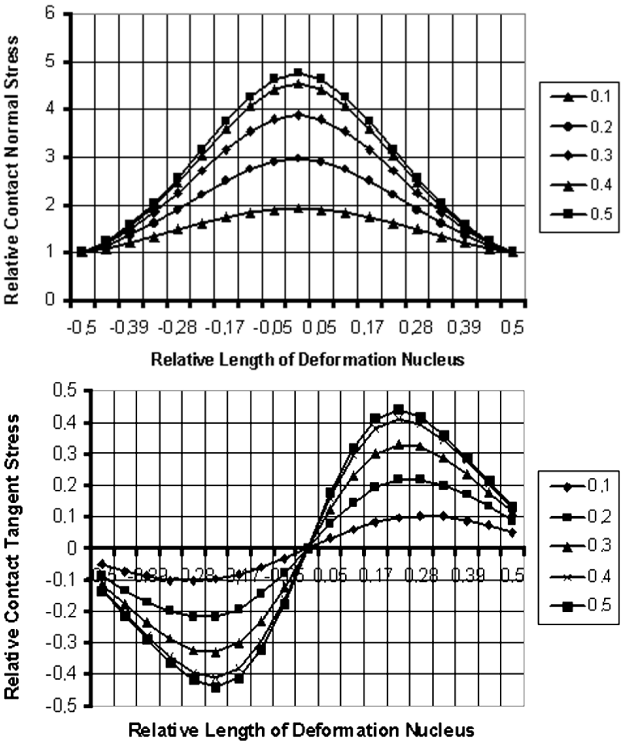

Figure 1: Distribution of the normal and tangent stresses at the contact during upsetting with rough strikers l/h = 8, f = 0,1...0,5

Slika 1: Porazdelitev kontaktnih normalnih in tangetnih napetosti pri krčenju s težkimi kladivi l/h = 8, f = 0,1...0,5

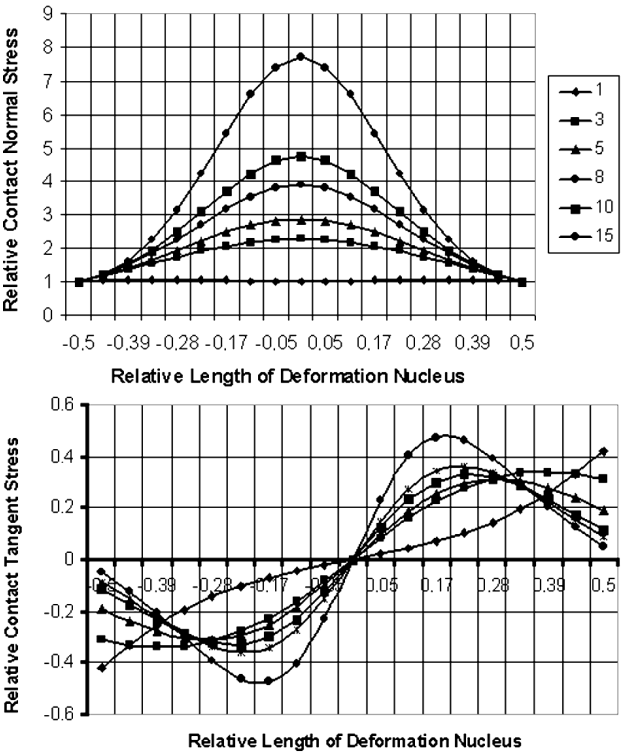

Figure 2: Distribution of the normal and tangent stresses at the contact during upsetting with rough strikers f = 0,3, l/h = 1...15

Slika 2: Porazdelitev kontaktnih normalnih in tangetnih napetosti pri krčenju s težkimi kladivi f = 0,3, l/h = 1...15

By substituting the components of the tensor of stresses into (14), we obtain

$$\sigma_x = -k_0 \cdot \frac{\exp(\theta' - \theta'_0)}{\cos A\Phi_0} \cdot \cos A\Phi + k_0$$

$$\sigma_y = -3k_0 \cdot \frac{\exp(\theta' - \theta'_0)}{\cos A\Phi_0} \cdot \cos A\Phi + k_0$$

$$\tau_{xy} = k_0 \cdot \frac{\exp(\theta' - \theta'_0)}{\cos A\Phi_0} \cdot \sin A\Phi \qquad (15)$$

The results of the calculation according to equations (15) in **Figures 1 to 4** show that the distribution of the contact stresses is related to the factor of the shape of the stress nucleus l/h and the friction coefficient f, the relative normal stresses $\sigma_y/2k_0$ and the relative tangent stresses τ_{xy}/k_0. The results of the calculation correspond to the real distribution diagrams of the contact stresses.[6] It should be emphasized that expressions (15) are uniform for the entire nucleus of deformation and there is no need to break it into separate zones of contact friction.[7] **Figures 5 and 6** show the distribution of stresses

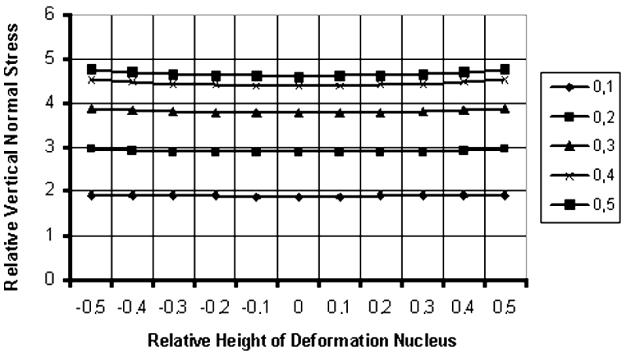

Figure 3: Distribution of the normal stresses along the plate height during the upsetting with rough strikers l/h = 8, f = 0,1...0,5

Slika 3: Porazdelitev normalnih napetosti po višini plošče pri krčenju s težkimi kladivi: l/h = 8, f = 0.1…0.5

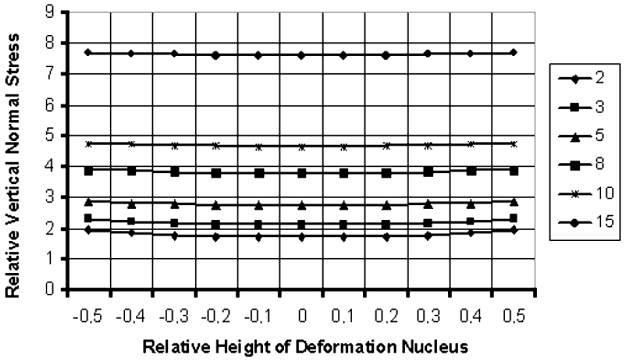

Figure 4: Distribution of the normal stresses along the strip height during the upsetting with rough strikers f = 0,3, l/h = 2...15

Slika 4: Porazdelitev normalnih napetosti po višini plošče pri krčenju s težkimi kladivi f = 0,3, l/h = 2...15

in the nucleus of deformation, which also include the shape factor and the friction coefficient.

The obtained results display qualitatively and quantitatively the general patterns of the distribution fields of the tensor of stresses over the entire nucleus of deformation. The results meet fully the requirements of the boundary conditions. In particular, the proposed procedure and expressions[15] can be recommended for the calculation of various problems in applications.

The proposed complex model of a plastic medium based on the closed solution can be considered as a generalization of the theory of plasticity, uniting the theories of deformation and of plastic yielding.

4 REFERENCES

[1] V. V. Chygyryns'kyy, I. Mamuzić, G. V. Bergeman: Analysis of the State of Stress of a Medium under Conditions of Inhomogeneous Plastic Yielding; Metalurgija. Zagreb. 43 (**2004**), 87–93

[2] A. N. Tikhonov, A. A. Samarsky: Uravnenia matematicheskoy fisiki (Equations of mathematical physics); Nauka, (**1977**), 735

[3] N. N. Malinin: Prikladnaya teoria plastichnosti i polsychesti (Applied theory of plasticity and yielding); Mashinostroyeniye, (**1975**), 399

[4] L. M. Kachanov: Osnovy teorii plastichnosti (Fundamentals of the theory of plasticity); Nauka, (**1969**), 419

[5] G. E. Arkulis, V. G. Dorogobid: Teoria plastichnosti (Theory of plasticity); Metalurgiya, (**1987**), 251

[6] A. P. Chekmarev, P. L. Klimenko: Experimentalnoe issledovanie udel'nyh davleniy na kontaktnoy poverhnosti pri prokatke v kalibrah (Experimental investigations of partial pressures on the contact surface in rolling in calibers); Obrabotka metallov davleniem (Pressure forming of metals); Sbornik trudov Dnepropetrovskogo metallurgicheskogo instituta; Khar'kov, M., 1960. – Vypusk 39

[7] M. V. Storozhev, E. A. Popov: Teoria obrabotki metallov davleniem (Theory of pressure working of metals); Mashinostroyeniye, (**1977**), 422

LIST OF SYMBOLS

σ – normal components of the stress tensor;
τ – tangential components of the stress tensor;
ξ – linear components of the strain-rate tensor;
γ – shear components of the strain-rate tensor;
ε – linear deformation along the axes x and y;
χ – factor of correspondence between the tangent stress and the temperature-deformation parameter of the centre to deformation;
Γ_i – intensity of the shift of the deformation;
τ_n – tangential contact stress on an arbitrary inclined area;
α – angle of inclination of the contact area;
k – shearing plastic deformation strength;
Φ – harmonic function depending on the coordinates of the deformation zone and the argument of a trigonometric function;
Φ_0 – argument of trigonometric function for $x = \pm l/2$ and $y = \pm h/2$;
A – constant characterizing the trigonometric function for the state of stress of the plastic medium;
A_6, A_{13} – constant factor, characterizing the shearing tangent stress in the zone of reduction
Ψ_0, Ψ_1 – values taking into account the influence of the factor of friction;
B – constant value characterizing the trigonometric function for the state of strain of the plastic medium;
θ_0 – factor exhibitors for $x = \pm l/2$ and $y = \pm h/2$;
θ' – harmonic function, exponential index, characterizing the shearing stress distribution in the zone of reduction;
θ'' – a harmonic function, exponential index, characterizing the distribution of the rate of shearing in the zone of reduction;
C_σ – constant value determining the state of stress of the plastic medium;
C_ξ – constant value characterizing the state of strain of the plastic medium;
T – temperature in the k-th point;
T_i – intensity of tangential stress;
H_i – intensity of shearing rates;
C_T – constant value characterizing the temperature field;
a – coefficient of temperature conductivity;
l and h – length and height of the deformation nucleus during strip upsetting;
f – friction coefficient;
k_0 – contact shear resistance at the beginning of the deformation nucleus

UDK 669.14.018:519.68
Original scientific article/Izvirni znanstveni članek

ISSN 1580-2949
MTAEC9, 44(3)147(2010)

COMPARATIVE MODELING OF WIRE ELECTRICAL DISCHARGE MACHINING (WEDM) PROCESS USING BACK PROPAGATION (BPN) AND GENERAL REGRESSION NEURAL NETWORKS (GRNN)

PRIMERJALNO MODELIRANJE ELEKTROEROZIJSKE ŽIČNE OBDELAVE (WEDM) Z UPORABO POVRATNOSTI (BPN) IN SPOŠNE NEVRONSKE REGRESIJSKE MREŽE (GRNN)

Onur Guven[1], Ugur Esme[2*], Iren Ersoz Kaya[3], Yigit Kazancoglu[4], M. Kemal Kulekci[5], Cem Boga[6]

[1]Mersin University, Engineering Faculty, Department of Mechanical Engineering, 33400, Mersin/Turkey
[2,3,5]Mersin University, Tarsus Technical Education Faculty Department of Mechanical Education, 33480, Tarsus-Mersin/Turkey
[4]Izmir University of Economics, Department of Business Administration, 35330, Balcova-Izmir/Turkey
[6]Cukurova University, Vocational School of Karaisali, 01770, Karaisali-Adana/Turkey
uguresme@gmail.com

Prejem rokopisa – received: 2010-01-22; sprejem za objavo – accepted for publication: 2010-03-02

The use of two neural networks techniques to model wire electrical discharge machining process (WEDM) is explored in this paper. Both the back-propagation (BPN) and General Regression Neural Networks (GRNN) are used to determine and compare the WEDM parameters with the features of the surface roughness. A comparison between the back-propagation and general regression neural networks in the modeling of the WEDM process is given. It is shown that both the back-propagation and general regression neural networks can model the WEDM process with reasonable accuracy. However, back propagation neural network has better learning ability for the wire electrical discharge machining process than the general regression neural network. Also, the back-propagation network has better generalization ability for the wire electrical discharge machining process than does the general regression neural network.

Keywords: WEDM, neural network, modeling, BPN, GRNN

Raziskana je uporaba dveh nevronskih mrež za modeliranje elekroerozijske žične obdelave (WEDM). Obe metodi: povratnostna (BPN) in splošna regresijska nevronska mreža (GRNN), sta uporabljeni za določitev in primerjavo VEDM-procesa. Dokazano je, da sta obe metodi primerni za modeliranje WEDM s sprejemljivo natančnostjo. Vendar pa ima povratnostna nevronska mreža boljšo sposobnost učenja in boljšo sposobnost posplošenja procesa kot splošna regresijska nevronska mreža.

Ključne besede: WEDM, nevronska mreža, modeliranje, BPN, GRNN

1 INTRODUCTION

Manufacturing industry is becoming ever more time-conscious with regard to the global economy, and the need for rapid prototyping and small production batches is increasing. These trends have placed a premium on the use of new and advanced technologies for quickly turning raw materials into usable goods; with no time being required for tooling.[1] Wire electrical discharge machining (WEDM) technology has been found to be one of the most recent developed advanced non-traditional methods used in industry for material processing with the distinct advantages of no thermal distortion, high machining versatility, high flexibility, rapid machining and high accuracy of complex parts.[2] The degree of accuracy of workpiece dimensions obtainable and the fine surface finishes make WEDM particularly valuable for applications involving manufacture of stamping dies, extrusion dies and prototype parts. Without WEDM the fabrication of precision workpieces requires many hours of manual grinding and polishing.[3–6]

The most important performance measures in WEDM are cutting speed, workpiece surface roughness and cutting width. Discharge current, discharge capacitance, pulse duration, pulse frequency, wire speed, wire tension, average working voltage and dielectric flushing conditions are the machining parameters which affect the performance measures.[3–7]

Tosun et al.[3] determined the effect of machining parameters on the cutting width and material removal rate based on the Taguchi method. Tosun and Cogun[4] investigated experimentally the effect of cutting parameters on wire electrode wear. Tosun et al.[5] investigated the effect of the cutting parameters on size of erosion craters (diameter and depth) on wire electrode experimentally and theoretically. Cogun and Savsar[6] investigated the random behaviour of the time-lag durations of discharge pulses using a statistical model for different pulse durations, pulse pause durations, and discharge currents in EDM.

Esme et al.[7] modeled the surface roughness in WEDM process using design of experiments and neural networks. Scott et al.[8] have developed formulas for the solution of a multi-objective optimization problem to select the best parameter settings on a WEDM machine.

They used a factorial design model to predict the measures of performances as a function of a variety of machining parameters. Wang and Rajurkar[9] have developed a WEDM frequency monitoring system to detect on-line the thermal load on the wire to prevent the wire from rupture. Spur and Schoenbeck[10] have investigated a finite element model and they have explained the impact of a discharge on the anode as a heat source on a semi-infinite solid whose size and intensity are time-dependent in WEDM. Tarng et al.[11] developed a neural network system to determine settings of pulse duration, pulse interval, peak current, open circuit voltage, servo reference voltage, electric capacitance and wire speed for the estimation of cutting speed and surface finish. Spedding and Wang[12] presented parametric combination by using artificial neural networks and they also characterized the roughness and waviness of workpiece surface and the cutting speed. Liao et al.[13] performed an experimental study to determine the variation of the machining parameters on the MRR, gap width and surface roughness. They have determined the level of importance of the machining parameters on the metal removal rate (MRR). Lok and Lee[14] compared the machining performance in terms of MRR and surface finish by the processing of two advanced ceramics under different cutting conditions using WEDM. Ramakrishnan and Karunamoorthy[15] developed an artificial neural network with Taguchi parameter design. Tsai et al.[16] relationships between the heterogeneous second phase and the machinability evaluation of the ferritic SG cast irons in the WEDM process. Sarkar et al.[17] studied on the features of trim cutting operation of wire electrical discharge machining of γ-titanium aluminide. Caydas et al.[18] developed an adaptive neuro-fuzzy inference system (ANFIS) for modeling the surface roughness in WEDM process.

As indicated in the previous studies, most of the research works are focused on the effect of machining parameters, discharge energy, theory and experimental verification crater formation on the wire electrode. The present study focused on the comparative modeling and prediction of surface roughness to compare the techniques of back propagation network (BPN) and general regression neural network (GRNN).

2 EXPERIMENTAL DETAILS

As shown in **Figure 1**, the experimental studies were performed on an *Acutex WEDM* machine tool. Different settings of pulse duration (t), open circuit voltage (V), wire speed (S) and dielectric flushing pressure (p) were used in the experiments. Table feed rate (8.2 mm/min), pulse interval time (18 μs), and wire tension (1800 g) are kept constant during the experiments[7].

AISI 4340 steel plate was used as a workpiece material with (150 × 150 × 10) mm dimensions. CuZn37 *Suncut* brass wire with 0.25 mm diameter and tensile strength of 900 N/mm^2 was used in the experiments. Workpiece average surface roughness (R_a) measurements were made by using *Phynix TR–100* portable surface roughness tester. Cut-off length (λ) and traversing length (l) were set as 0.3 mm and 5 mm, respectively. Pulse duration, open circuit voltage, wire speed and dielectric flushing pressure were selected as input parameters and surface roughness (R_a) was selected as an output parameter[7].

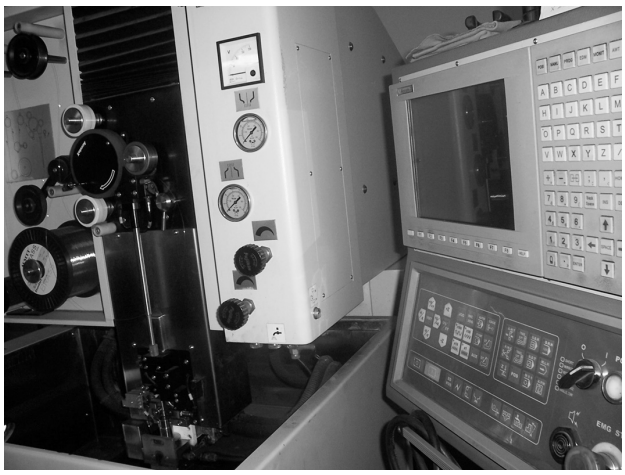

Figure 1: Acutex WEDM used in the experiments[7]
Slika 1: Acutex WEMM, uporabljen za preizkuse[7]

Four measurements were made and their average was taken as R_a value for a machined work surface. After collecting the experimental results both techniques namely back propagation neural network (BPN) and general regression neural network (GRNN) techniques were carried out to predict surface roughness (R_a).

3 ARTIFICIAL NEURAL NETWORKS (ANN)

It is well known that modeling the relationships between the input and output variables for non-linear, coupled, multi-variable systems is very difficult. In recent years, neural networks have demonstrated great

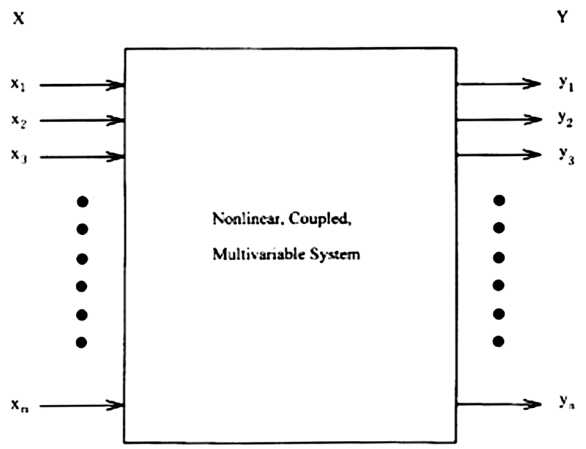

Figure 2: A non-linear, coupled, and multi-variable system[19]
Slika 2: Nelinearen, povezan in multivariabilni sistem[19]

potential in the modeling of the input–output relationships of complicated systems.[19,20] Consider that $X = \{x_1, x_2 \ldots, x_m\}$ is the input vector of the system where m is the number of input variables and $Y = \{y_1, y_2 \ldots, y_n\}$ is the corresponding output vector of the system where n is the number of output variables[19] as shown in **Figure 2**. In this section, the use of back-propagation and general regression networks to construct the relationships between the input vector X and output vector Y of the system will be explored.

3.1 Back-Propagation Networks (BPN)

The back-propagation network is composed of many interconnected neurons that are often grouped into input, hidden and output layers. The neurons of the input layer are used to receive the input vector X of the system and the neurons of the output layer are used to generate the corresponding output vector Y of the system. The back-propagation network used in this study is shown in **Figure 3**. For each neuron a summation function for all the weighted inputs are calculated as:

$$\text{net}_j^k = \sum_j w_\mu^k o_i^{k-1} \tag{1}$$

where net^k_j is the summation function for all the inputs of the j-th neuron in the k-th layer, w^k_{ji} is the weight from the i-th neuron to the j-th neuron and o_i^{k-1} is the output of the i-th neuron in the (k–1)-th layer.

Setting 5-hidden layers resulted in lowest error between predicted and experimental results. Therefore, in the present work, 4-inputs, 5-hidden layer, 1 output layer (4 : 5 : 1 model) back propagation neural network has been used. The used BPN algorithm is shown in **Figure 3**.

As shown in Eq. (1), the neuron evaluates the inputs and determines the strength of each one through its weighting factor, i.e. the larger the weight between two neurons, the stronger is the influence of the connection.[19] The result of the summation function can be treated as an input to an activation function from which the output of the neuron is determined. The output of the neuron is then transmitted along the weighted outgoing connections to serve as an input to subsequent neurons. To modify the connection weights properly, a supervised learning algorithm involving two phases is employed.[21] The first is the forward phase which occurs when an input vector X is presented and propagated forward through the network to compute an output for each neuron.[19,20] Hence, an error between the desired output y_j and actual output o_j of the neural network is computed.[19] The summation of the square of the error E can be expressed as:

$$E = \frac{1}{2}\sum_{j-1}^{n}\left(y_j - o_j\right)^2 \tag{2}$$

The second is the backward phase which is an iterative error reduction performed in a backward direction. To minimize the error between the desired and actual outputs of the neural network as rapidly as possible, the gradient descent method, adding a momentum term,[21] is used. The new incremental change of weight $\Delta w^k_{ji}(n + 1)$ can be expressed as:

$$\Delta w_{ji}^k(n+1) = -\eta\frac{\partial E}{\partial w_{ji}^k} + \alpha\Delta w_{ji}^k(n) \tag{3}$$

where η is the learning rate, α is the momentum coefficient and n is the index of iteration. Through this learning process, the network memorizes the relationships between input vector X and output vector Y of the system through the connection weights.[19–21]

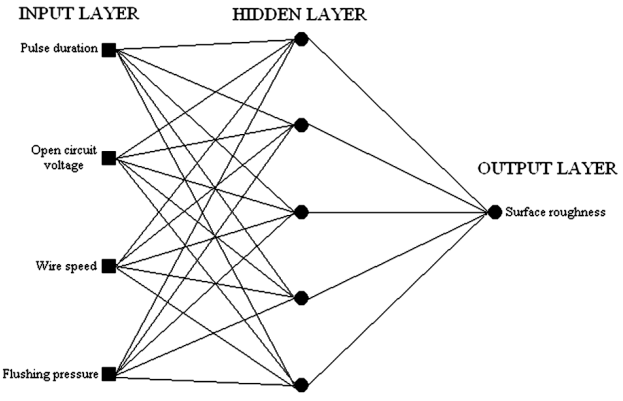

Figure 3: BPN network used for modeling
Slika 3: BPN mreža, uporabljena za modeliranje

4 GENERAL REGRESSION NEURAL NETWORKS (GRNN)

The General Regression Neural Networks (GRNN) introduced by Donald Specht in 1990 is a memory-based feed forward neural network based on the approximate estimation of the probability density function from observed samples using Parzen-window estimation.[22] It approximates any arbitrary function between input and output vectors. This approach removes the necessity to specify a functional form of estimation.

The method utilizes a probabilistic model between an independent random vector X (input) and a dependent scalar random variable Y (output). Let x and y be the particular measured values of X and Y, respectively, and $\hat{g}(x, y)$ is the joint continuous probability density function of X and Y. A good choice for a non-parametric estimate of the probability density function g is the Parzen window estimator as proposed by Parzen and performed for multidimensional cases by Cacoullos.[22–26] Given a sample of n real D dimensional x_i vectors and corresponding scalar y_i values, the estimate of joint probability density in GRNN is given by;

$$\hat{g}(x,y) = \frac{1}{(2\pi)^{(d+1)/2}\sigma^{(d+1)}}\frac{1}{n}\sum_{i=1}^{n}\left[\exp\left(\frac{(x-x_i)^T(x-x_i)}{2\sigma^2}\right)\exp\left(\frac{(y-y_i)^2}{2\sigma^2}\right)\right] \tag{4}$$

where σ is the window width of a sample probability, called the smoothing factor of the kernel[24]. The expected value of Y given x (the regression of Y on x) is given by;

$$E[Y/x] = \frac{\int_{-\infty}^{+\infty} Y \cdot g(x,Y)\mathrm{d}Y}{\int_{-\infty}^{+\infty} g(x,Y)\mathrm{d}Y} \quad (5)$$

Using Eq. (4), Eq. (5) becomes;

$$\hat{y}(x) = E[Y/x] = \frac{\sum_{i=1}^{n}\left[y_i \exp(d_i)\right]}{\sum_{i=1}^{n}\exp(d_i)} \quad (6)$$

where d_i is the distance between the input vector and the i^{th} training vector, and is given by;

$$d_i^2 = -\frac{(x-x_i)^T(x-x_i)}{2\sigma^2} \quad (7)$$

The estimate $\hat{y}(x)$ is thus a weighted average of all the observed y_i values where each weight is exponentially proportional to its Euclidean distance from x.

As shown in **Figure 4**, the structure of the GRNN consists of 4 layers; the input layer, the hidden (pattern) layer, the summation layer and the output layer. As a preprocessing step, all input variables of the training data are scaled. Then, they are copied as the weights into the pattern units.

As a preprocessing step, all input variables of the training data are scaled. Then, they are copied as the weights into the pattern units. The summation layer has two units that can be denoted as the numerator and the denominator of Eq. (6). The output layer gives the estimate of the expected value of $\hat{y}(x)$. If y and $\hat{y}$ are the vector variables, the results above are generalized by adding with one summation unit for each component of y in the output layer.

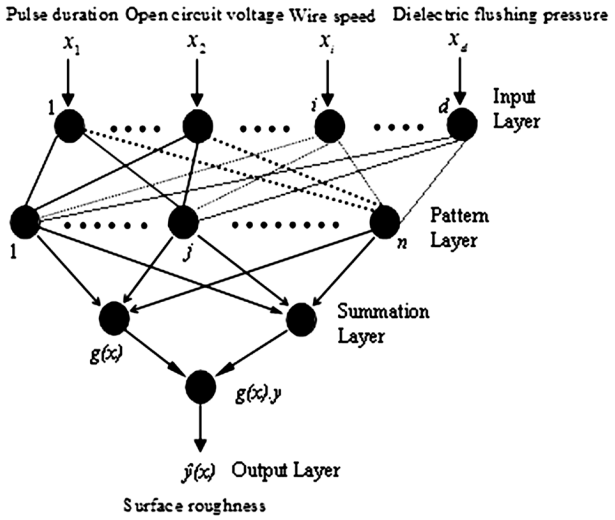

Figure 4: Constructed GRNN network
Slika 4: Zgrajena GRNN-mreža

The only adjustable parameter of the network is σ, the smoothing factor for the kernel function. It is critical to decide an optimum value for σ. The larger values of this factor cause the density to be smooth, and $\hat{y}(x)$ then converges to the sample mean of the observed y_i. On the other hand, when σ is chosen very small, the density is forced to have non-gaussian shapes. Then, the oscillatory points have a bad effect on the estimate. All values of y_i are taken into account where the points closer to x are given heavier weights, if the optimum value of σ is selected.[24–26] Therefore, in this study, σ was chosen as 0.57 due to the optimum value of success rate that was found after iterative calculation of σ values between 0.1 and 0.9.

The main advantage of GRNN according to other techniques is fast learning. It is a one-pass training algorithm, and does not require an iterative process. The training time is just the loading time of the training matrix. Also, it can handle both linear and non-linear data because the regression surface is instantly described everywhere, even just one sample is enough for this. Thus, other existing pattern nodes tolerate faulty samples. Another advantage is the fact that adding new samples to the training set does not require re-calibration of the model. As the sample size increases, the estimate surface converges to the optimal regression surface. Thus, it requires many training samples to span the variation in the data and all these to be stored for the future use. Solely, this causes a trouble of an increase in the amount of the computation to evaluate new points. In the course of time, highly improvements in the speed of the computer's processing power prevent this being a major problem. Furthermore, this also can be overcome by applying the various clustering techniques for grouping samples that each center is represented by this group of samples.[22–26] However, there is only one disadvantage that there is no intuitive method for choosing the optimal smoothing factor.

5 RESULTS AND DISCUSSIONS

In this study, twenty-eight set of data under different process condition was used for training and testing of the BPN and GRNN. Sixteen of them were used as a training purpose and the rest were used as testing purposes. **Table 1** shows the design matrix and training set used for BPN and GRNN analysis.

Testing the validation of BPN and GRNN results was made using the input parameters according to the design matrix given in **Table 2**.

These comparisons have been depicted in terms of percentage error in **Figure 5** for validation set of experiments. From **Table 2** it is evident that for our set of data the BPN result predicts the surface roughness nearer to the experimental values than the GRNN results. But,

Table 1: Neural network training set[7]
Tabela 1: Podatki za trening nevronske mreže[7]

WEDM input Parameters					Output
Exp. no	*t*/ns	*V*/V	*S*/(mm/min)	*p*/(kg/cm^2)	R_a/μm
1	200	300	12	16	2.12
2	200	60	4	16	1.13
3	900	60	4	6	2.14
4	200	60	12	16	1.24
5	200	300	12	6	2.32
6	200	300	4	16	1.98
7	900	60	12	16	2.15
8	900	300	12	6	3.85
9	200	300	4	6	2.10
10	900	300	4	16	3.24
11	900	60	12	6	2.26
12	900	300	12	16	3.65
13	900	60	4	16	2.01
14	200	60	4	6	1.18
15	900	300	4	6	3.55
16	200	60	12	6	1.24

Table 2: Test and comparison of BPN and GRNN results
Tabela 2: Preizkusi in primerjava BPN- in GRNN-rezultatov

Exp. No	WEDM input parameters					Modeling			
						Back Propagation Neural Network (BPN)		General Regression Neural Network (GRNN)	
	t/ns	*V*/V	*S*/(mm/min)	*p*/(kg/cm^2)	R_a/μm	*predicted*	*error*	*predicted*	*error*
1	300	80	4	6	1.30	1.26	3.08	1.38	-6.15
2	400	90	5	8	1.50	1.36	9.33	1.55	-3.33
3	500	150	6	10	2.08	2.02	2.88	1.96	5.77
4	700	250	10	14	3.18	3.48	-9.43	3.22	-1.26
5	350	60	12	16	1.29	1.24	3.88	1.43	-10.85
6	450	70	5	16	1.58	1.53	3.16	1.50	5.06
7	550	100	8	11	2.08	2.02	2.88	1.88	9.62
8	750	180	4	6	2.92	3.11	-6.51	2.72	6.85
9	850	200	10	8	3.27	3.47	-6.12	3.14	3.98
10	200	300	12	8	2.23	2.37	-6.28	2.31	-3.59
11	250	300	4	10	1.96	2.00	-2.04	2.14	-9.18
12	300	250	6	20	1.89	1.81	4.23	2.02	-6.88
						Average error: 4.99% CPU time = 2.3 min		Average error: 6.04% CPU time = 0.074 sec	

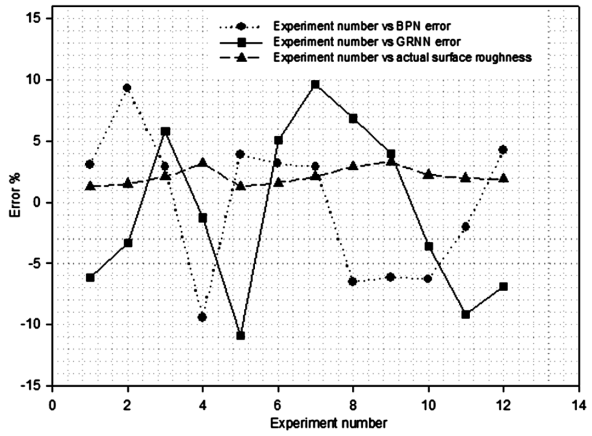

Figure 5: BPN and GRNN errors in prediction of the surface roughness
Slika 5: BPN- in GRNN-napake pri napovedi hrapavosti površine

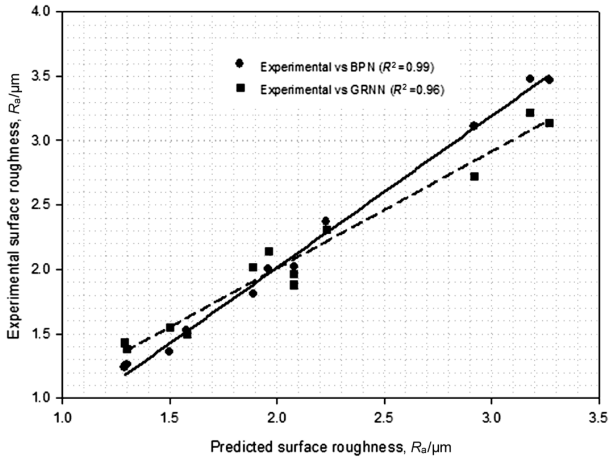

Figure 6: Comparison of predicted and experimental results
Slika 6: Primerjava napovedanih in eksperimentalnih rezultatov

GRNN is much faster than BPN with the CPU times of *0.074* s and *2.3* min respectively. In the prediction of surface roughness values the average errors for BPN and GRNN are calculated as *4.99 %* and *6.04 %* respectively.

The value of the multiple coefficient of R^2 is obtained as *0.99* for BPN and *0.96* for GRNN which means that the fitted line is very close to the experimental results. **Figure 6** represents the comparison of predicted (both BPN and GRNN) and actual results. Both BPN and GRNN results showed that the predicted values have been very close to experimental values.

6 CONCLUSIONS

The prediction of optimal machining conditions for the required surface finish and dimensional accuracy plays a very important role in the process planning of the wire erosion discharge machining process. This paper has described a neural network approach and comparison of Back Propagation Networks (BPN) and General Regression Neural Networks (GRNN) networks for the modeling of wire electrical discharge machining process using small set of data. Both the BPN and GRNN networks were used to construct the complicated relationships between the process parameters and the surface roughness. The experimental results has showed that the BPN network has better learning ability (with average error of *4.99 %* and multiple coefficient of R^2 of *99 %*) for the wire electrical discharge machining process than the GRNN (with average error of *6.04 %* and multiple coefficient of R^2 of *0.96*) network. Training of BPN network consumed more CPU time (elapsed time *2.3* min) than the GRNN (elapsed time *0.074* s). In addition to this, the back propagation network has better generalization ability for the wire electrical discharge machining process than the general regression neural network modeling.

7 REFERENCES

[1] J. Wang, , 19 (**2003**), 114

[2] U. Caydas, A. Hascalik, Journal of Materials Processing Technology, 202 (**2008**), 574–582

[3] N. Tosun, C. Cogun, G. Tosun, Journal of Materials Processing Technology, 152 (**2004**), 316–322

[4] N. Tosun, C. Cogun, H. Pihtili, Int. J. Adv. Manuf. Technol., 21 (**2003**), 857–865

[5] N. Tosun, C. Cogun, A. Inan, Machining Science and Technology, 7 (**2003**), 209–219

[6] C. Cogun, M. Savsar, International Journal of Machine Tools and Manufacture, 3 (**1990**), 467–474

[7] U. Esme, A. Sagbas, F. Kahraman, Iranian Journal of Science & Technology, Transaction B, Engineering, 33 (**2009**), 231–240

[8] D. Scott, S. Boyina, K. P. Rajurkar, Int. J. Prod. Res., 11 (**1991**), 2189–2207

[9] W. M. Wang, K. P. Rajurkar, Monitoring sparking frequency and predicting wire breakage in WEDM, Sensors and Signal Processing for Manufacturing, ASME, Production Engineering Division (PED), New York, 55 (**1992**), 49–64

[10] G. Spur, J. Schoenbeck, Anode erosion in wire-EDM-A theoretical model. CIRP Ann., 1 (**1993**), 253–256

[11] Y. S. Tarng, S. C. Ma, L. K. Chung, International Journal of Machine Tools and Manufacture, 35 (**1995**), 1693–1701

[12] T. A. Spedding, Z. Q. Wang, Precis. Eng., 20 (**1997**), 5–15

[13] Y. S. Liao, J. T. Huang, H. C. Su, Journal of Materials Processing Technology, 71 (**1997**), 487–493

[14] Y. K. Lok, T. C. Lee, Journal of Materials Processing Technology, 63 (**1997**), 839–843

[15] R. Ramakrishnana, L. Karunamoorthyb, Journal of Materials Processing Technology, 207(**2008**), 343–349

[16] T. C Tsai, J.T. Horng, N.M. Liu, C.C. Chou, K.T. Chiang, Materials and Design, 29 (**2008**), 1762–1767

[17] S. Sarkar, S. Mitra, B. Bhattacharyya, Journal of Materials Processing Technology, 205(**2008**), 376–387

[18] U. Caydas, A. Hascalik, S. Ekici, doi:10.1016/j.eswa.2008.07.019, (**2008**)

[19] S. C. Juang, Y. S. Tarng, H. R. Lii, Journal of Materials Processing Technology, 75 (**1998**), 54–62

[20] J. A. Freeman, D. M. Skapura, Neural Networks: Algorithms, Application and Programming Techniques, Addison–Wesley, New York, (**1991**)

[21] J. McClelland, D. Rumelhart, Parallel Distributed Processing, MIT Press, Cambridge, MA, 1 (**1986**)

[22] D. Specht, A General Regression Neural Network. IEEE Trans. Neural Networks, 2 (**1991**), 568–576

[23] T. Cacoullos, Estimation of a multivariate density. Annals of Inst. Stat. Math., 18 (**1996**), 178–189

[24] D. Yeung, C. Parzen, Window Network Intrusion Detectors, Proceedings of the Sixteenth International Conference on Pattern Recognition, Quebec City, Canada, 4 (**2002**), 385–388

[25] I. Ersoz Kaya, T. Ibrikci, A. Cakmak, Journal of Computational Intelligence in Bioinformatics, 1 (**2008**), 1–11

[26] U. Esme, I. Ersoz, A. Ozbek, F. Kahraman, A. Sagbas, Cukurova University Journal of Engineering and Architecture, 23 (**2008**), 57–66

UDK 543.428.2:579.24
Original scientific article/Izvirni znanstveni članek

ISSN 1580-2949
MTAEC9, 44(3)153(2010)

DEGRADATION OF BACTERIA *ESCHERICHIA COLI* BY TREATMENT WITH Ar ION BEAM AND NEUTRAL OXYGEN ATOMS

UNIČEVANJE BAKTERIJ *ESCHERICHIA COLI* S CURKOM IONOV Ar IN NEVTRALNIH ATOMOV KISIKA

Kristina Eleršič[1], Ita Junkar[1], Aleš Špes[1], Nina Hauptman[2], Marta Klanjšek-Gunde[2], Alenka Vesel[1]*

[1]Jozef Stefan Institute, Jamova cesta 39, 1000 Ljubljana, Slovenia
[2]National Institute of Chemistry, Hajdrihova 19, 1000 Ljubljana, Slovenia
alenka.vesel@ijs.si

Prejem rokopisa – received: 2009-06-18; sprejem za objavo – accepted for publication: 2010-03-12

Scanning electron microscopy was used to determine the difference between bacteria degradation by two types of particles presented in gaseous plasma, i.e. positively charged ions and neutral oxygen atoms. The source of ions was an argon ion gun with the ion energy of 1 keV and the flux of 3×10^{18} m^{-2} s^{-1}. The source of neutral oxygen atoms was inductively coupled oxygen plasma supplying the flux of oxygen atoms of about 1.5×10^{23} m^{-2} s^{-1}. The ion beam treatment time was 1800 s while the oxygen atom treatment time was 300 s. Bacteria *Escherichia coli,* strain ATCC 25922 were deposited onto well activated aluminum at the concentration of about 3×10^6 cfu and exposed to both particles. SEM analysis was performed using a field emission microscope with the energy of primary electrons of 1 keV. SEM images revealed huge difference in morphology of bacteria treated by both methods. While ions tend to drill holes into bacterial cell wall, the atoms caused a more even disruption of bacterial cell wall. The results were explained by kinetic, potential and charging effects.

Key words: bacteria, *Escherichia coli,* sterilization, degradation, oxygen plasma, atoms, ions, SEM

Z vrstično elektronsko mikroskopijo smo raziskovali razliko v degradaciji bakterij pri obdelavi z dvema različnima vrstama delcev v plinski plazmi: s pozitivno nabitimi in z nevtralnimi kisikovimi atomi. Vir ionov argona z energijo 1 keV in tokom 3×10^{18} m^{-2} s^{-1} je bila ionska puška. Vir nevtralnih atomov kisika s tokom $1{,}5 \times 10^{23}$ m^{-2} s^{-1} na površino vzorcev pa je bila induktivno sklopljena kisikova plazma. Čas obdelave z ioni je bil 3000 s, medtem ko je bil čas obdelave s kisikovimi atomi 300 s. Bakterije *Escherichia coli*, sev ATCC 25922 smo nanesli na dobro aktivirano površino aluminija in jih potem izpostavili curkom obeh vrst delcev. Koncentracija bakterij je bila 3×10^6 cfu. Po obdelavi smo površino vzorcev analizirali z vrstično elektronsko mikroskopijo (SEM). SEM-slike so razkrile veliko razliko v morfologiji bakterij, obdelanih z atomi oziroma ioni. Medtem ko ioni povzročijo nastanek lukenj v celični steni bakterij, pa atomi bolj enakomerno degradacijo celične stene. Dobljene rezultate smo razložili z vplivom kinetičnih in potencialnih efektov ter vplivom nabijanja površine.

Ključne besede: bakterije, *Escherichia coli*, sterilizacija, degradacija, kisikova plazma, atomi, ioni, SEM

1 INTRODUCTION

Plasma sterilization has attracted much attention in the past decade due to possible application for sterilization of delicate materials that cannot stand autoclaving in humid air at 130 °C. Several different types of discharges have been used to create plasma suitable for destruction of vital bacteria and their spores.[1–9] The discharges include low and atmospheric pressure. Among atmospheric discharges, RF and microwave plasma torches are particularly popular, while the dielectric barrier glow discharge was not found as efficient. The same applies also for otherwise popular corona discharges. The low pressure discharges suitable for destruction of bacteria at low temperature include the DC, RF and microwave discharges.[10–14] Radiofrequency discharges are particularly popular since they assure for a high density of plasma radicals and rather low kinetic temperature of neutral gas.

Most authors presented results on bacterial deactivation as a function of discharge parameters. The discharge parameters that are often varied include the type of gas or gas mixture, the pressure in the discharge tube and the gas flow, the discharge power, the dimensions and the type of material used for the discharge chamber, etc. Much less work, however, has been done on determination of sterilization effects versus plasma parameters. Not surprisingly, the explanations of observed sterilization effects are often contradictory. Many authors explain sterilization by destruction of bacterial DNA caused by UV photons from plasma. Other authors state that sterilization is due to chemical etching of the bacterial cell wall with radicals such as O, N, H, etc. Some other authors take into account also the kinetic effects of bombardment with positive ions, and most authors agree that synergetic effects play an important role.

In order to understand the role of different plasma particles it is the best to separate them and treat bacteria only with one type plasma particles. At the experiments presented in this paper we exposed bacteria separately to 2 types of different plasma particles: energetic non-reactive ions and neutral oxygen atoms with the kinetic temperature of 300 K.

2 EXPERIMENTAL

2.1 Sample preparation

Bacteria *Escherichia coli* (*E. coli*) were cultivated according to the standard procedure. In experiment we used bacteria *E. coli* strain ATCC 25922. It was grown at 37 °C, on LB plates for 24 h. Cells were then resuspended in sterile water. Number of cells was adjusted to approximately 3×10^6 cfu (colony forming unites).

Live bacteria were deposited onto commercially available aluminum foils. Substrates were first carefully cleaned with wet chemical treatment, and then activated with a brief exposure to oxygen plasma in order to assure the removal of any traces of organic contaminants and achieve optimal hydrophilicity. A drop of water containing vital bacteria was placed onto the substrate. Due to highly activated surface, the bacteria-containing water drop was spread on a large surface. Such spreading allowed for two dimensional distributions of bacteria with out overlapping.

2.2 Experimental system

Samples were treated either by neutral oxygen atoms in an afterglow chamber of oxygen plasma reactor or by positively charged Ar ions from a commercial ion gun. The schematic of the experimental setup for the case of oxygen atoms is shown in **Figure 1**. The vacuum system is pumped with a two stage rotary pump. The effective pumping speed at the exit of the experimental chamber is almost identical to the nominal pumping speed of the pump, i.e.16 m^3/h. The experimental chamber is connected to a discharge chamber through a narrow tube that allows for a difference in the effective pumping speeds between the experimental and discharge chambers and thus a pretty high drift velocity of gas through the narrow tube. Both chambers as well as the connection tube are made from borosilicate glass Schott 8250. This glass has a low recombination coefficient for the reaction $O + O \rightarrow O_2$.[15,16] Such a configuration assures for experiments at constant (i.e. room) temperature and constant density of oxygen atoms in the vicinity of substrates. The density of neutral oxygen atoms is measured with a catalytic probe.[17-19] At the experimental pressure of 75 Pa the O density is about 1×10^{21} m^{-3}. The resultant flux of neutral oxygen atoms onto the surface of the sample is then $j = ¼\ nv = 1.5 \times 10^{23}$ m^{-2} s^{-1}.

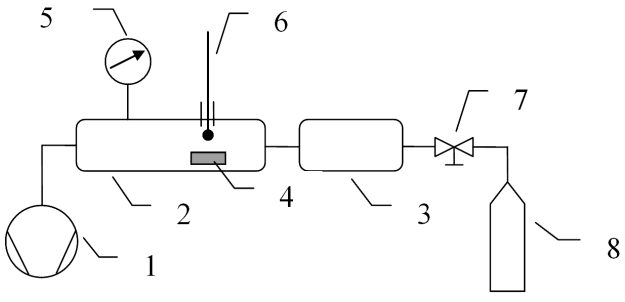

Figure 1: The experimental setup for treatment of bacteria with neutral oxygen atoms. 1 – vacuum pump, 2 – experimental chamber, 3 – discharge chamber, 4 – sample, 5 – vacuum gauge, 6 – catalytic probe, 7 – inlet valve, 8 – oxygen flask

Slika 1: Shema eksperimentalnega sistema za obdelavo bakterij z nevtralnimi atomi kisika: 1 – vakuumska črpalka, 2 – eksperimentalna komora, 3 – razelektritvena komora, 4 – vzorec, 5 – vakuummeter, 6 – katalitična sonda, 7 – dozirni ventil, 8 – jeklenka s kisikom

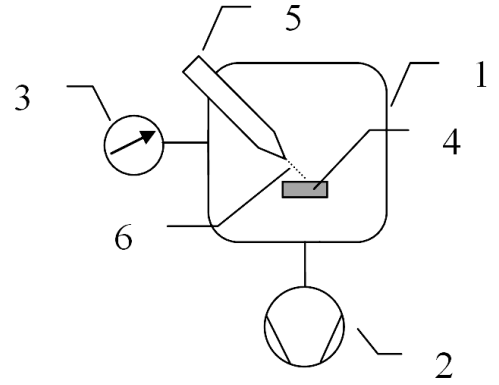

Figure 2: The experimental setup for treatment of bacteria with Ar ions: 1 – UHV chamber, 2 – pumping system, 3 – vacuum gauge, 4 – sample, 5 – ion gun, 6 – energetic ions.

Slika 2: Shema eksperimentalnega sistema za obdelavo bakterij z ioni Ar: 1 – UVV komora, 2 – črpalni sistem, 3 – vakuummeter, 4 – vzorec, 5 – ionska puška, 6 – energijski ioni

The experimental setup for treatment of bacteria with Ar ions is shown schematically in **Figure 2**. The source of Ar ions is a commercial ion gun used for sputtering of materials during depth profiling. Ar ion beam with the energy of 1 keV at an incidence angle of 45° and a raster of 3 mm × 3 mm was used for treating bacteria. The ion current is 0.15 A/m^2 giving the ion flux onto the surface of the substrate with bacteria of 3×10^{18} m^{-2} s^{-1}. We used no charge compensation during treatment of bacteria with argon ions.

2.3 SEM imaging

Scanning electron micrographs of substrates with bacteria were obtained using a field emission microscope Karl Zeiss Supra 35 VP. A 1 kV accelerating voltage was used to record images.

3 RESULTS

SEM image of untreated *E. coli* bacteria is shown in **Figure 3**. The image does not look very sharp. This is not an artifact of the microscope but rather the consequence of the presence of the capsule on the surface of bacteria as well as between bacteria. Namely, the capsule is composed predominantly of chemically bonded water as well as some sugars, proteins and lipids – material that are a bad scatterer for electrons. That's why the SEM image looks rather dim.

A SEM image of a bacteria treated by Ar ions is shown in **Figure 4**. The bacteria are badly damaged and definitely not capable of revitalization.

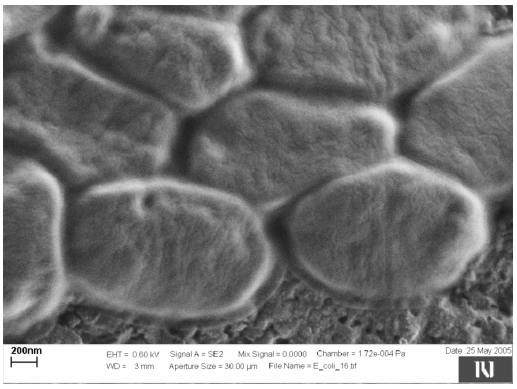

Figure 3: SEM image of untreated bacteria
Slika 3: SEM-slika neobdelane bakterije

A SEM image of bacteria treated in the afterglow of the oxygen plasma, i.e. with neutral oxygen atoms only, is presented in **Figure 5**. In this case, the surface morphology is very different from that observed in **Figure 4**.

4 DISCUSSION

Figures 3, 4 and **5** represent SEM images of bacteria *E. coli*. Bacteria presented in **Figure 3** are live what has been confirmed by cultivation using the standard plate count technique. Bacteria are covered with a thin film of jelly of lipopolysaccharides and is called capsule. The majority of lipopolysaccharide cover material has chemically bonded water. This thin cover is (about 400 nm or more) capsular polysaccharide gel[20] which serves as a medium for gluing bacteria together as well as for sticking onto surfaces. The capsule also facilitates formation of three dimensional clusters of bacteria. Such clustering was not observed at our experiments since we activated the surface of the aluminum prior to bacterial deposition. The surface of activated aluminum foil is perfectly hydrophilic thus allowing for two- dimensional spreading of bacteria on its surface. Such procedure for bacteria fixation therefore allows for uniform treatment of bacteria with plasma particles.

An exposure of bacteria to argon ions causes a strong damage. **Figure 4** represents the SEM image of bacteria

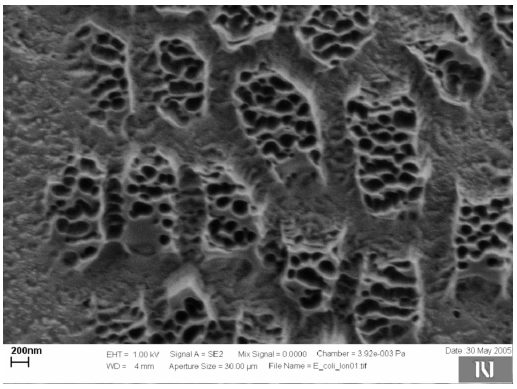

Figure 4: SEM image of bacteria treated with argon ions
Slika 4: SEM-slika bakterije, obdelane z ioni argona

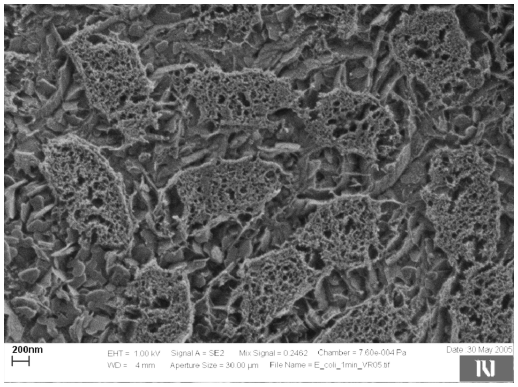

Figure 5: SEM image of bacteria treated with oxygen atoms
Slika 5: SEM-slika bakterije, obdelane z atomi kisika

after receiving the argon ion dose of 5.4×10^{21} m^{-2}. The bacteria are definitely not capable of revitalization what was proved also by control experiments using the plate count technique. It is interesting that the damage caused by ions is far from being uniform. Namely, a hole – like structure of the bacterial cells is observed. Although it is known that ion beam etching is never perfectly homogeneous and isotropic, such rich surface morphology cannot be due to common effects observed at ion beam etching of organic materials. The observed morphology may be attributed to appearance of the local surface electrical charge during treatment with positively charged ions. Namely, the electrical conductivity of bacteria is poor. Since the composition of the cell wall is far from being uniform, some spots on the surface may keep larger charge than other. The surface charge influence the local uniformity of the ion flux on the surface causing local focusing and thus further non-uniformity of the ion beam etching. Finally, the bacteria obtain morphology as shown in **Figure 4**. The ions practically cannot reach the uppermost part of bacteria since positive charge prevents it.

The SEM image of bacteria treated with oxygen atoms shows a completely different picture. In this case, the badly damaged bacteria are flattened, also. In fact, little material remained after receiving the dose of approximately 4.5×10^{25} m^{-3}. The remains observed on the surface of the aluminum foil after treatment with oxygen atoms represent only ash – mostly inorganic remains of the bacterial material after rather complete oxidation of organic material. This picture is in agreement with previous observations on selective etching of organic materials by oxygen radicals[21].

5 CONCLUSIONS

Bacteria *E. coli* were deposited onto aluminum foils and exposed to positively charged argon ions or neutral oxygen atoms in the ground state. In both cases, the samples were kept at room temperature. Since argon is inert gas that does not interact chemically with organic material, the interaction was almost completely kinetic. Apart

from radiation damage, the argon ions caused sputtering of the bacterial material. The sputtering was extremely inhomogeneous what was explained by local charging of the bacteria. In the case of oxygen atoms, any kinetic effect is neglected since the O atoms are thermal at room temperature. In this case, rather uniform degradation of bacteria occurred and only ashes remained after the treatment. The interaction of O atoms with bacteria is therefore purely chemical. In both cases, bacteria were badly damaged and unable to revitalize.

ACKNOWLEDGEMENT

This research was funded by Slovenian Research Agency, Contract No. P2 – 0082.

6 REFERENCES

[1] Moisan M, Barbeau J, Moreau S, Pelletier J, Tabrizian M, Yahia L'H, Low-temperature sterilization using gas plasmas: a review of the experiments and an analysis of the inactivation mechanisms, Int. J. Pharm. 226 (**2001**), 1–2

[2] Soloshenko IA, Tsiolko VV, Khomich VA, Shchedrin AI, Ryabtsev AV, Bazhenov VY, Mikhno IL, Sterilization of medical products in low-pressure glow discharges, Plasma Phys. Reports 26 (**2000**), 792–800

[3] Park BJ, Takatori K, Lee MH, Han DW, Woo YI, Son HJ, Kim JK, Chung KH, Hyun SO, Park JC, Escherichia coli sterilization and lipopolysaccharide inactivation using microwave-induced argon plasma at atmospheric pressure, Surf. Coat. Technol. 201 (**2007**), 5738–5741

[4] Fridman G, Brooks AD, Balasubramanian M, Fridman A, Gutsol A, Vasilets VN, Ayan H, Friedman G, Comparison of direct and indirect effects of non-thermal atmospheric-pressure plasma on bacteria, Plasma Process. Polym. 4 (**2007**), 370–375

[5] Moreau S, Moisan M, Tabrizian M, Barbeau J, Pelletier J, Ricard A, Yahia L'H, Using the flowing afterglow of a plasma to inactivate Bacillus subtilis spores: Influence of the operating conditions, J. Appl. Phys. 88 (**2000**), 1166–1174

[6] Kylian O, Rossi F, Sterilization and decontamination of medical instruments by low-pressure plasma discharges: application of Ar/O-2/N-2 ternary mixture, J. Phys. D Appl. Phys. 42 (**2009**), 085207

[7] Ricard A, Moisan M, Moreau S, Determination, through titration with NO, of the concentration of oxygen atoms in the flowing afterglow of Ar-O2 and N2-O2 plasmas used for sterilization purposes, J. Phys. D Appl. Phys. 34 (**2001**), 1203–1212

[8] Lerouge S, Wertheimer MR, Marchand R, Tabrizian M, Yahia LH, Effect of gas composition on spore mortality and etching during low-pressure plasma sterilization, J. Biomed. Mater. Res. 51 (**2000**), 128–135

[9] Stapelmann K, Kylian O, Denis B, Rossi F, On the application of inductively coupled plasma discharges sustained in $Ar/O_2/N_2$ ternary mixture for sterilization and decontamination of medical instruments, J. Phys. D Appl. Phys. 41 (**2008**), 192005

[10] Cvelbar U, Vujošević D, Vratnica Z, Mozetič M, The influence of substrate material on bacteria sterilization in an oxygen plasma glow discharge, J. Phys. D Appl. Phys. 39 (**2006**), 3487–3493

[11] Vujošević D, Mozetič M, Cvelbar U, Krstulović N, Miloševič S, Optical emission spectroscopy characterization of oxygen plasma during degradation of Escherichia coli, J. Appl. Physic. 101 (**2007**), 103305-1–103305-7

[12] Canal C, Gaboriau F, Villeger S, Cvelbar U, Ricard A, Studies on antibacterial dressings obtained by fluorinated post-discharge plasma, Int. J. Pharm. 367 (**2009**), 155–161

[13] Vratnica Z, Vujošević D, Cvelbar U, Mozetič M, Degradation of bacteria by weakly ionized highly dissociated redio-frequency oxygen plasma, IEEE Trans. Plasma Sci. 36 (**2008**), 1300–1301

[14] Vujošević D, Vratnica Z, Vesel A, Cvelbar U, Mozetič M, Drenik A, Mozetič T, Klanjšek Gunde M, Hauptman N, Oxygen plasma sterilization of bacteria, Mater. Technol. 40 (**2006**), 227–232

[15] Drenik A, Cvelbar U, Vesel A, Mozetič M, Weakly ionized oxygen plasma, Inf. MIDEM 35 (**2005**), 85–91

[16] Sorli I, Petasch W, Kegel B, Schmid H, Liebl G, Plasma processes 1. Plasma basics, plasma generation, Inform. Midem, 26 (**1996**), 35–45

[17] Babič D, Poberaj I, Mozetič M, Fiber optic catalytic probe for weakly ionized oxygen plasma characterization, Rev. Sci. Instrum. 72 (**2001**), 4110–4114

[18] Poberaj I, Mozetič M, Babič D, Comparison of fiber optics and standard nickel catalytic probes for determination of neutral oxygen atoms concentration, J. Vac. Sci. Technol. A 20 (**2002**), 189–193

[19] Mozetič M, Characterization of reactive plasmas with catalytic probes, Surf. Coat. Technol. 201 (**2007**), 4837–4842

[20] Stirm S, Freund-Mölbert E, *Escherichia coli* Capsule Bacteriophages II. Morphology, J Virol. 8 (3) (**1971**), 330–342

[21] Mozetič M, Controlled oxidation of organic compounds in oxygen plasma, Vacuum 71 (**2003**), 237–240

UDK 669.14.018.252:620.18:621.785
Professional article/Strokovni članek

ISSN 1580-2949
MTAEC9, 44(3)157(2010)

EFFECT OF HEAT TREATMENT ON THE MICROSTRUCTURE AND PROPERTIES OF Cr-V LEDEBURITIC STEEL

VPLIV TOPLOTNE OBDELAVE NA MIKROSTRUKTURO IN LASTNOSTI LEDEBURITNEGA JEKLA Cr-V

Stanislav Krum, Jana Sobotová, Petr Jurči

Department of Material Science, Faculty of Mechanical Engineering, CTU in Prague, Karlovo nam. 13, 12135 Prague, Czech Republic
s.krum@seznam.cz

Prejem rokopisa – received: 2009-11-16; sprejem za objavo – accepted for publication: 2010-03-01

Duplex coating of high-alloyed tool steels is the newest and most promising technology that allows improvements to tools in terms of wear resistance and service time. However, the deposition of thin films onto the nitrided surface is associated with problems that are not yet solved. To clarify the problem of the adhesion and mechanical properties of the system substrate/coating it is necessary to prepare the substrate with well-defined microstructural parameters. The Vanadis 6 PM ledeburitic steel was chosen as a substrate for surface processing. It was austenitised, quenched and double tempered to a desired hardness of *HRC* = (57–58). Some specimens were also sub-zero treated in order to improve the transformation of austenite to martensite. The microstructure of the heat-processed steel was examined using optical microscopy and scanning electron microscopy. The resistance to nucleation of fracture was assessed with the three-point bending-strength test and the fracture surfaces were subjected to a fractographic analysis.

Keywords: Sub-zero treatment, hardness, ledeburitic tool steel

Dupleksno pokritje visokolegiranih orodnih jekel je nova in obetajoča tehnologija za povečanje obrabne obstojnosti in dobe uporabnosti orodij. Vendar je nanos tanke plasti na nitrirano površino povezana s problemi, ki še niso rešeni. Za razlago problema adhezije in mehanskih lastnosti sistema podlaga-pokritje je treba pripraviti podlago z dobro opredeljenimi parametri mikrostrukture. Jeklo Vanadis 6 PM je bilo izbrano za podlago za nadaljevanje procesiranja. Bilo je avstenitizirano, kaljeno in dvakrat popuščeno na želeno trdoto *HRC* = (57–58). Nekateri preizkušanci so bili tudi podhlajeni zaradi povečanja obsega premene avstenita v martenzit. Mikrostruktura je bila preiskana z optično in vrstično elektronsko mikroskopijo. Odpornost proti začetku razpoke je bila preverjena s tritočkovnim upogibom, površina prelomov pa fraktografsko preiskana.

Ključne besede: podhladitev, trdota, ledeburitno jeklo

1 INTRODUCTION

Generally, heat treatment improves a steel's toughness and hardness, and it is absolutely necessary for the proper functioning of tool steels. The heat treatment usually consists of austenitizing, quenching and is followed by multiple tempering. After this procedure the tool steels gain properties that are suitable for industrial applications.

In tool steels, retained austenite is an undesired component because it lowers the hardness after the heat treatment. Additionally, it can transform into martensite and/or bainite at elevated working temperatures or under high loading. This worsens the operational suitability of tools and strong efforts are made to minimize the amount of retained austenite.

With this aim, the sub-zero treatment was introduced in the 1960s. This treatment hinders the retained austenite stabilization in steels with the M_f temperature lower than room temperature. A typical example of these steels is the group of ledeburitic steels, with a higher carbon content and with a large amount of alloying elements.

Nevertheless, the opinions on the effect of the sub-zero treatment on the working utility of tools are diverse because the nature of the process has not yet been entirely clarified. In 1962 Rapatz concluded that there is no advantage in using these methods for ledeburitic high-speed steels [1]. Also, Hoyle did not recommend this type of heat treatment for ledeburitic steels [2]. On the other hand, Berns stated different recommendations for ledeburitic steels. He found that it was possible to significantly increase the hardness of chromium ledeburitic steels with an immediate sub-zero treatment after quenching [3]. He stated that the immediate sub-zero treatment after quenching from the usual temperatures and tempering allowed a hardness increase of the low-carbon-content steels. For the steel X155CrVMo 12 1, it is possible to reach *HRC* = 67 and in the case of superhard ledeburitic steel X290Cr even *HRC* = 69. Thus, it is evident that older studies focused on the research of this type of heat treatment did not produce definite results. On top of that, in the case of ledeburitic high-speed steels the results were not even optimistic. Nevertheless, in recent years the experiments engaged in sub-zero treatment have become more realistic.

The goal of this study was to investigate what happens when Cr-V ledeburitic steels are plasma nitrided. For this purpose, it was necessary to prepare a

substrate with a well-defined microstructure and properties. In this paper, the Vanadis 6 steel processed using various heat treatments, including a sub-zero period, is investigated.

2 EXPERIMENTAL

2.1 Material

The samples were made from Vanadis 6 – a ledeburitic cold-work tool steel with the chemical composition of 2.1 % C, 7 % Cr, 6 % V and an initial hardness of HV_{10} = 284 Fifteen specimens for three-point bend tests were net-shape machined to dimensions of (10 × 10 × 100) mm and then submitted to the heat treatments in **Table 1**.

2.2 Methods

Several measurements and experiments for determining the material and structural properties were performed. The hardness was measured with the EMCOTEST M4C 075G3 hardness tester using the Vickers HV_{10} and Rockwell HRC methods. These two methods were selected because of the expected high material surface hardness. The resistance against crack initiation was determined with a three-point bending test. The microstructure of the steel in the as-received state and of heat treated steel were examined with optical microscopy and scanning electron microscopy, applying a Neophot 32 optical microscope and a Jeol JSM 5410 scanning electron microscope. Also, the quantitative analysis of the carbides' dissolution during the austenitizing, which consisted of determining the particle count and the size classes, was performed. The first out was executed using the micrograph of the as-received material and the second one using the micrograph after the heat treatment A. Within the fractography study, micrographs of two material states were taken: after heat-treatment A (i.e. without the sub-zero treatment) and after heat treatment C (i.e., with sub-zero treatment –196 °C; 7 h).

3 EXPERIMENTAL RESULTS

3.1 Optical and scanning microscopy

The as-received steel Vanadis 6 has a microstructure with fine carbide particles uniformly distributed throughout the ferritic matrix. These carbides are of eutectic, secondary and eutectoid origin, as shown in the micrographs in **Figure 1** and **Figure 2**.

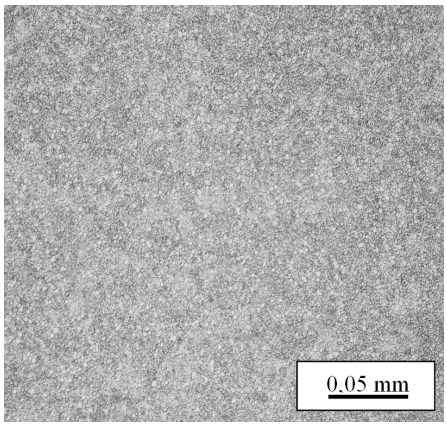

Figure 1: Microstructure of the as-received material state (optical microscopy)
Slika 1: Mikrostruktura prejetega jekla, optični posnetek

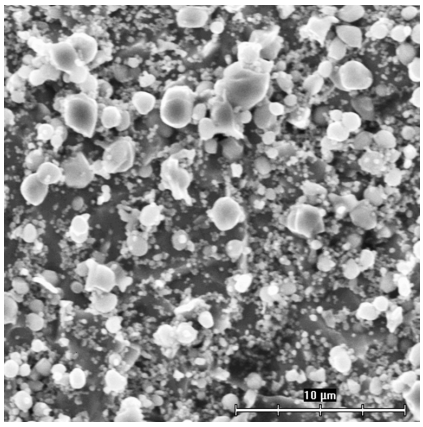

Figure 2: Microstructure of the as-received state (SEM)
Slika 2: Mikrostruktura prejetega jekla, SEM-posnetek

After the heat treatment (**Figure 3**), the matrix consists of tempered martensite and particles of the carbides M_7C_3 and MC.

The material submitted to heat treatment B, i.e., with sub-zero treatment, shows, at first glance, a similar microstructure, MC and M_7C_3 carbide particles in a martensitic matrix with particles of carbide M_7C_3 fewer and smaller than after heat-treatment A, **Figure 4**.

The results of the quantitative analysis of the carbide particles are presented in **Figure 5** (as-received) and

Table 1: Heat treatment details
Tabela 1: Podatki o toplotni obdelavi

Specimen	Heat-treatment marking	Heat-treatment process details			
		Austenitizing	Quenching $p(N_2)$/bar	Sub-zero treatment	Tempering
1 – 5	A	1030 °C; 30 min	6	–	2 × 530 °C; 1 h
6 – 10	B	1030 °C; 30 min	6	–196 °C; 4 h	2 × 530 °C; 1 h
11 – 15	C	1030 °C; 30 min	6	–196 °C; 7 h	2 × 530 °C; 1 h

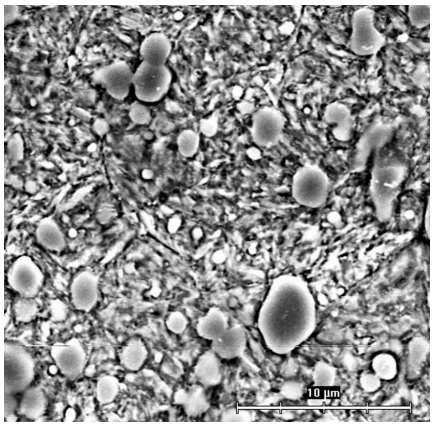

Figure 3: Microstructure of Vanadis 6 after the heat-treatment A
Slika 3: Mikrostruktura jekla Vanadis 6 po toplotni obdelavi A

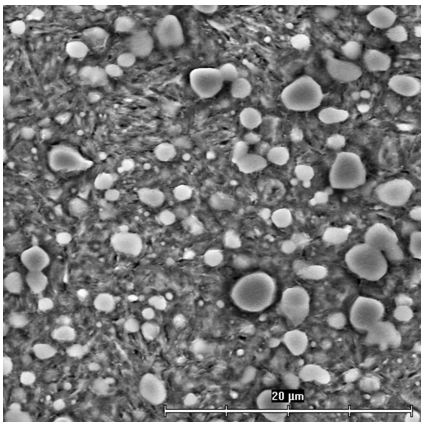

Figure 4: Microstructure of Vanadis 6 after the heat-treatment B
Slika 4: Mikrostruktura jekla Vanadis 6 po toplotni obdelavi B

Figure 6 (after heat treatment). It is obvious that after the heat treatment the number of carbide particles is lower and their size is smaller in comparison to the as-received material. The main reason is that the as-received material contains a larger number of ultra-fine eutectoid carbides that undergo a complete dissolution in the austenite. In addition, also a part of the

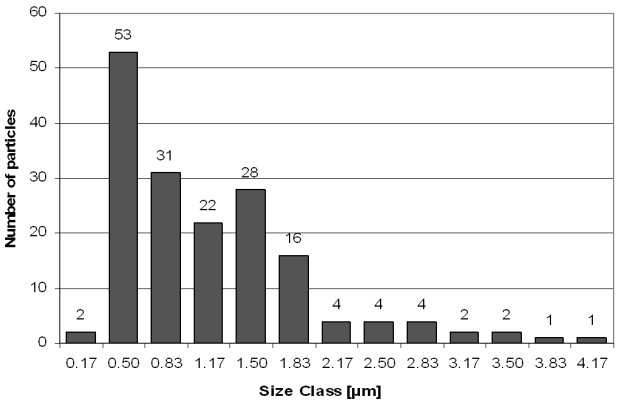

Figure 5: Results of the analysis of the carbide particles' sizes and the number in the as-received material
Slika 5: Rezultati določitve velikosti in števila karbidnih zrn v prejetem jeklu

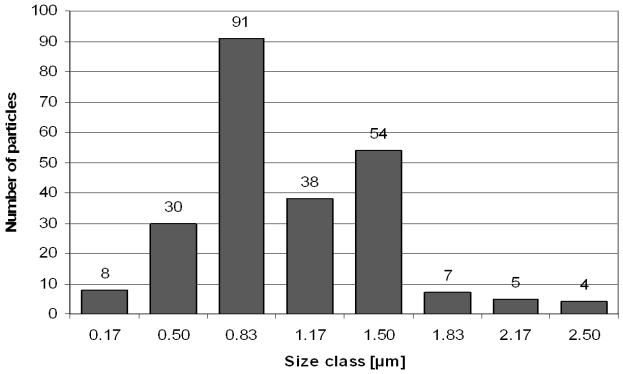

Figure 6: Results of the analysis of the carbide particles' sizes and the number in the material after the heat treatment
Slika 6: Rezultati določitve velikosti in števila karbidnih zrn v toplotno obdelanem jeklu

secondary carbides is dissolved in the austenite during the heating up to the final austenitizing temperature

3.2 Hardness

The results of the hardness measurements obtained from the samples of all the heat treatments are presented in **Table 2**. The hardness of the as-received material was HV_{10} = 284 and the average hardness after heat treatment without a sub-zero treatment was of HV_{10} = (748 ± 6.9) (*HRC* = (60 ± 0.2)). The process with the 4-h sub-zero treatment at –196 °C leads to an average surface hardness of HV_{10} = (734 ± 6.9) (*HRC* = (58 ± 1.0)). Finally, the process including the 7-h sub-zero treatment at –196 °C leads to the average surface hardness of HV_{10} = (721 ± 5.6) (*HRC* = (58 ± 0.4)).

It is evident that after the sub-zero treatment the hardness is slightly lower – of the order of tens of Vickers units compared to the heat treatment without this treatment. This hardness decrease is higher with a longer duration of the sub-zero period. These findings do not agree with [2,4], which stated that the hardness increased after this procedure.

Table 2: Average hardness and standard deviation after different heat treatments
Tabela 2: Povprečna trdota in standardna deviacija po različni toplotni obdelavi

Measurement Method	HV_{10}			*HRC*		
Heat Treatment	A	B	C	A	B	C
Average Value of Hardness	748	734	721	60	58	58
Standard Deviation	6.9	6.9	5.6	0.2	1.0	0.4

3.3 Three-point bending strength

The three-point bending strength was used to determine the materials' resistance to fracture initiation. The measured parameters were the maximum load until fracture and the bending strength. The tests were performed on all the samples and the average values of the samples with the same heat treatment are presented

in **Table 3**. The bending strength was calculated from the F_{max} using the formula: $R_{Mo} = \frac{3F_{max} \cdot L}{2a^3}$, where: F_{max}/N – load at the fracture, L/mm – length of the sample, a/mm – width of the sample with square intersection.

Table 3: Results of the three-point bending-strength test
Tabela 3: Rezultati tritočkovnega upogiba

Heat treatment	Average value of bending strength /MPa	Average value of the maximum load /kN
A	2436	16.24
B	2961	19.74
C	3217	21.45

The relationships between the load and the deformation (*F-s*) of the samples are shown in the following diagrams. **Figure 7** shows the *F-s* diagram for the sample processed with the processing route A (no sub-zero treatment). The *F-s* relation is practically linear, therefore only a minimum plastic deformation until fracture can be expected to occur. Also, the three-point bending strength and the maximum load F_{max} were relatively low (**Table 3**); the fracture appeared when the load reached only 16.24 kN. In **Figure 8**, the behavior after the B heat treatment (–196 °C, 4 h sub-zero treatment) is shown. The *F-s* relation is not a completely linear shape, especially at high loading, and indicates that some plastic deformation took place during the testing. The fracture in this case appeared at a load of 19.74 kN. **Figure 9** shows the results of the three-point bending test of the sample processed with the C treatment (–196 °C, 7 h sub-zero treatment). The dependence of the load deformation is even less linear because of the greater portion of plastic deformation. The fracture occurs at 21.45 kN.

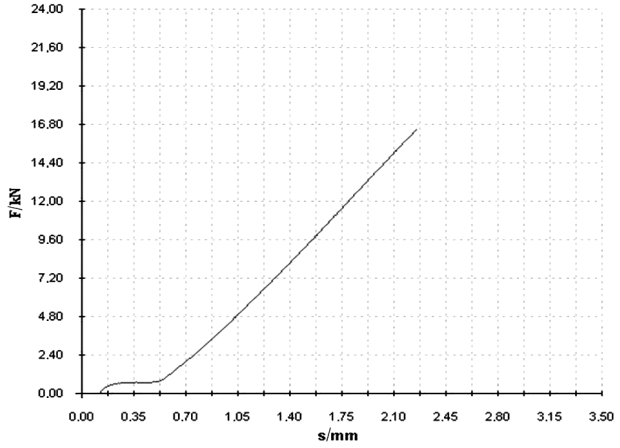

Figure 7: Dependence of *F-s* for the three-point bending test of the sample processed using the A treatment (without the sub-zero treatment)
Slika 7: *F-s*-odvisnost za tritočkovni upogib po toplotni obdelavi A (brez podhladitve)

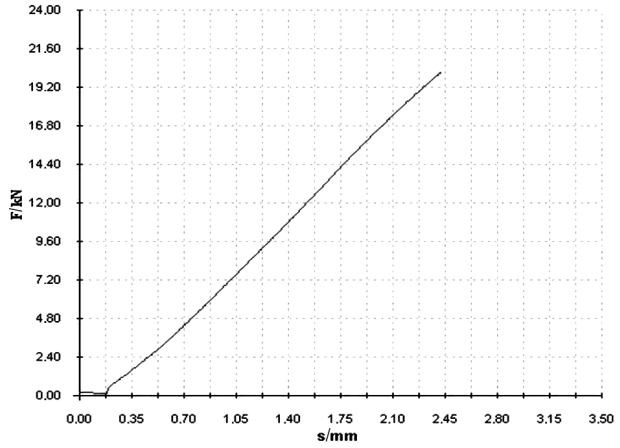

Figure 8: Dependence of *F-s* for the three-point bending test of the sample processed using the B treatment (with –196 °C, 4 h sub-zero treatment)
Slika 8: *F-s*-odvisnost za tritočkovni upogib po toplotni obdelavi B (podhladitev –196 °C, 4 h)

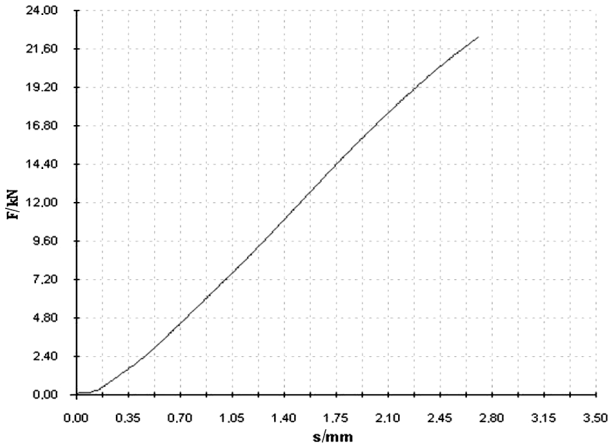

Figure 9: Dependence of *F-s* for the three-point bending test of the sample processed using the C treatment (with –196 °C, 7 h sub-zero treatment)
Slika 9: F-s odvisnost za tritočkovni upogib po toplotni obdelavi C (podhladitev –196 °C, 7 h)

From these results, it seems that the sub-zero period has a relatively small, but positive, effect on the three-point bending strength and it agrees with the changes in hardness, as with a higher bending strength, the hardness is lower.

3.4 Fractography

The fracture of the specimen processed using the processing route A is shown in **Figure 10**. The fracture was initiated on the tensile-strained side of the specimen and propagated throughout the specimen. Step-like propagation tracks are visible in the region near the surface of the specimen. At a depth of approx. 1 mm, a great step is also found.

The micrograph in **Figure 11** at a higher magnification shows that the fracture surface presents a dimpled morphology with some areas of microcleavages and indicates that a very low energy was spent for the crack propagation.

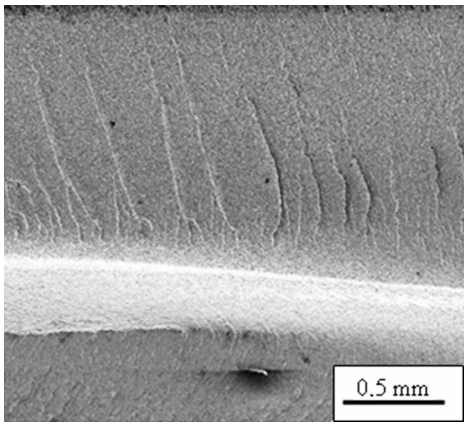

Figure 10: Fracture surface of the sample processed using the A treatment
Slika 10: Površina preloma po toplotni obdelavi A

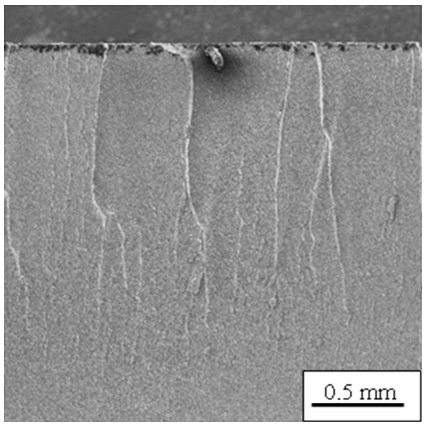

Figure 12: Fracture surface of the sample processed using the C treatment
Slika 12: Površina preloma po toplotni obdelavi C

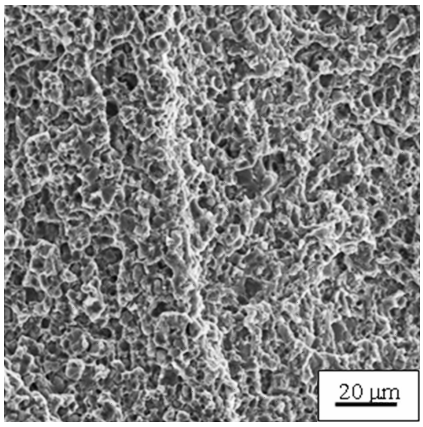

Figure 11: Detail of the fracture surface of the sample processed using the A treatment
Slika 11: Detajl površine preloma po toplotni obdelavi A

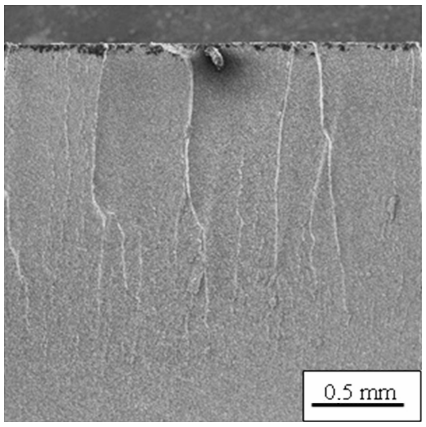

Figure 13: Detail of the fracture surface of the sample processed using the C treatment
Slika 13: Detajl površine preloma po toplotni obdelavi C

The fracture surface of the sample processed using the C treatment sample at 35-times magnification is presented in **Figure 12**, and at 1000-times magnification is shown **Figure13**. The dimples in the fracture surface of the sample processed using the C treatment are deeper and the step-like propagation tracks are longer than on the sample processed using the A treatment (**Figure 10**). Considering the *F-s* diagrams, showing that for the sample processed using the C treatment a greater amount of plastic deformation energy was consumed, it is possible to say that performed sub-zero treatment improves slightly the ductility of the tool steel.

4 CONCLUSIONS

1) After all of the performed heat-treatment processes the microstructure of he material consisted of tempered martensite and undissolved carbides.
2) The hardness was slightly higher for the steel without the sub-zero treatment than for the steel that underwent this process.
3) The sub-zero processed samples had a slightly higher three-point bending strength. The reason is that the crack propagation is connected with a higher consumption of plastic energy until the fracture.
4) The results of the mechanical tests are rather unexpected and so further, and more accurate, tests and examinations will be necessary to determine and verify the causes of this unexpected observation.

Acknowledgements

This paper has originated thanks to the support obtained from the Czech Universities Development Fund (IGS) within the grant CTU0908212.

5 LITERATURE

[1] Rapatz, F.: Die Edelstaehle, 5. Aufl. Springr Verlag, Berlin/Gottingen/Heidelberg, 1962, p. 862
[2] Hoyle, G.: High Speed Steels, Butterworth, London – Boston – Durban – Singapore – Sydney – Toronto – Wellington, University Press Cambridge
[3] Berns, H.: HTM 29 (**1974**), 4, s.236
[4] Company literature Uddeholm AB Vanadis 6